# EXPERIMENTAL INVESTIGATION OF TURBINE BLADE PLATFORM FILM COOLING AND ROTATIONAL EFFECT ON TRAILING EDGE INTERNAL COOLING

A Dissertation

by

LESLEY MAE WRIGHT

Submitted to the Office of Graduate Studies of
Texas A&M University
in partial fulfillment of the requirements for the degree of

DOCTOR OF PHILOSOPHY

August 2006

Major Subject: Mechanical Engineering

# EXPERIMENTAL INVESTIGATION OF TURBINE BLADE PLATFORM FILM COOLING AND ROTATIONAL EFFECT ON TRAILING EDGE INTERNAL COOLING

A Dissertation

by

LESLEY MAE WRIGHT

Submitted to the Office of Graduate Studies of
Texas A&M University
in partial fulfillment of the requirements for the degree of

DOCTOR OF PHILOSOPHY

Approved by:

Chair of Committee, Je-Chin Han
Committee Members, Taher Schobeiri
Sai Lau
Hamn-Ching Chen
Head of Department, Dennis O'Neal

August 2006

Major Subject: Mechanical Engineering

## ABSTRACT

Experimental Investigation of Turbine Blade Platform Film Cooling and Rotational Effect on Trailing Edge Internal Cooling. (August 2006)

Lesley Mae Wright, B.S., Arkansas State University;

M.S., Texas A&M University

Chair of Advisory Committee: Dr. Je-Chin Han

The present work has been an experimental investigation to evaluate the applicability of gas turbine cooling technology. With the temperature of the mainstream gas entering the turbine elevated above the melting temperature of the metal components, these components must be cooled, so they can withstand prolonged exposure to the mainstream gas. Both external and internal cooling techniques have been studied as a means to increase the life of turbine components.

Detailed film cooling effectiveness distributions have been obtained on the turbine blade platform with a variety of cooling configurations. Because the newly developed pressure sensitive paint (PSP) technique has proven to be the most suitable technique for measuring the film effectiveness, it was applied to a variety of platform seal configurations and discrete film flows. From the measurements it was shown advanced seals provide more uniform protection through the passage with less potential for ingestion of the hot mainstream gases into the engine cavity.

In addition to protecting the outer surface of the turbine components, via film cooling, heat can also be removed from the components internally. Because the turbine

blades are rotating within the engine, it is important to consider the effect of rotation on the heat transfer enhancement within the airfoil cooling channels. Through this experimental investigation, the heat transfer enhancement has been measured in narrow, rectangular channels with various turbulators. The present experimental investigation has shown the turbulators, coupled with the rotation induced Coriolis and buoyancy forces, result in non-uniform levels of heat transfer enhancement in the cooling channels. Advanced turbulator configurations can be used to provide increased heat transfer enhancement. Although these designs result in increased frictional losses, the benefit of the heat transfer enhancement outweighs the frictional losses.

# DEDICATION

Mom and James, thanks for everything

## ACKNOWLEDGMENTS

I would like to express deep gratitude to my advisor, Professor J.C. Han, for the opportunity to conduct research in the Turbine Heat Transfer Laboratory, for his support, and for his consistent guidance and encouragement. I would also like to thank the members whom have graciously served on my committee, Professor S. Lau, Professor M.T. Schobeiri, and Professor H.C. Chen.

Financial support for this experimental investigation was received from the Advanced Gas Turbine Systems Research (AGTSR) program (project numbers SR-082 and SR-094) and the University Turbine Systems Research (UTSR) program (project number 02-01-SR113) under the supervision of the United States Department of Energy (DOE).

## NOMENCLATURE

| | | |
|---|---|---|
| $A$ | = | surface area of copper plate ($m^2$) |
| AR | = | channel aspect ratio, $W/H$ |
| C | = | true chord length of the blade |
| $C_{ax}$ | = | axial chord length of the blade |
| $C_{mix}$ | = | oxygen concentration of mainstream-coolant mixture |
| $c_p$ | = | specific heat of coolant (kJ/(kgK)) |
| $C_\infty$ | = | oxygen concentration of mainstream |
| $D_h$ | = | hydraulic diameter (m) |
| $D$ | = | inlet hole diameter |
| d | = | film hole diameter |
| $e$ | = | rib height (m) |
| $f$ | = | friction factor |
| $f_o$ | = | Blasius fully developed friction factor in non-rotating smooth tube |
| $h$ | = | heat transfer coefficient ($W/m^2K$) |
| $H$ | = | channel height (0.5 in, 1.27 cm) |
| $I_b$ | = | background intensity captured by optical components |
| $I_f$ | = | discrete film hole momentum flux ratio ($= \rho_f V^2_f / \rho_m V^2_{m2} \cong V^2_f / V^2_{m2}$) |
| $I_s$ | = | slot injection momentum flux ratio ($= \rho_s V^2_s / \rho_m V^2_{m1} \cong V^2_s / V^2_{m1}$) |
| $I(P)$ | = | emission intensity of PSP |
| $I(P)_{air}$ | = | emission intensity of PSP recorded with air as film coolant |
| $I(P)_{mix}$ | = | emission intensity of PSP recorded with nitrogen as film coolant |

$I(P)_{ref}$ = emission intensity of PSP at reference (atmospheric) pressure

$I(T)$ = emission intensity of TSP

$I(T)_{ref}$ = emission intensity of TSP at reference temperature

$k$ = thermal conductivity of coolant (W/mK)

$l_f$ = discrete film hole length

$l_s$ = slot length

$L$ = hole length or heated length of duct (6 in, 15.24 cm)

$\dot{m}$ = mass flow rate of coolant (kg/s)

Nu = regionally averaged Nusselt number, $hD_h/k$

$Nu_o$ = Nusselt number for flow in fully-developed turbulent non-rotating smooth tube

$M$ = blowing ratio = $\rho_c V_c / \rho_m V_m \cong V_c / V_m$

$M_f$ = discrete film hole blowing ratio (= $\rho_f V_f / \rho_m V_{m2} \cong V_f / V_{m2}$)

$m_s$ = slot injection mass flow ratio (percentage of the mainstream flow)

$M_s$ = slot injection blowing ratio (= $\rho_s V_s / \rho_m V_{m1} \cong V_s / V_{m1}$)

$MFR_{total}$ = total mass flux ratio (coolant to mainstream)

$P$ = rib pitch (m)

$P_i$ = pressure at the inlet of the heated test section (Pa)

$P_e$ = pressure at the outlet of the heated test section (Pa)

$P_{O2}$ = partial pressure of oxygen

Pr = Prandtl number

$Q$ = rate of heat transfer (W)

| | | |
|---|---|---|
| $Q_{net}$ | = | net rate of heat transfer (W) |
| $q_{net}''$ | = | net heat flux at wall ($W/m^2$) |
| $\bar{R}$ | = | mean rotating arm radius (m) |
| Re | = | mainstream flow Reynolds number base on the inlet velocity and axial chord length or Reynolds number based on hydraulic diameter, $\rho V D_h/\mu$ |
| $Ro$ | = | Rotation number, $\Omega D_h/V$ |
| $S$ | = | equivalent slot width (total inlet hole area / total pitch) |
| T | = | local, calculated temperature (K) |
| $T_{aw}$ | = | local adiabatic wall temperature (°C) |
| $T_{bi}$ | = | inlet coolant bulk temperature (K) |
| $T_{bx}$ | = | local coolant bulk temperature (K) |
| $T_c$ | = | coolant temperature (°C) |
| $T_m$ | = | mainstream temperature (°C) |
| $T_s$ | = | local, coolant temperature from upstream slot (K) |
| $T_w$ | = | local surface temperature (°C) |
| $Tu$ | = | turbulence intensity |
| $V$ | = | bulk velocity in streamwise direction (m/s) |
| $V_c$ | = | coolant velocity (m/s) |
| $V_m$ | = | mainstream velocity (m/s) |
| $V_f$ | = | discrete film hole velocity (m/s) |
| $V_{m1}$ | = | mainstream velocity at the cascade inlet (m/s) |
| $V_{m2}$ | = | mainstream velocity at the cascade exit (m/s) |

$V_s$ = slot injection velocity (m/s)

w = slot width (m)

$W$ = channel width (2 in, 5.08 cm)

$x$ = distance downstream of holes or axial distance from the cascade leading edge (m) or streamwise location (m)

$\alpha$ = lateral injection angle or rib angle

$\beta$ = lateral injection angle or angle of channel orientation

$\theta$ = streamwise injection angle

$\rho$ = density of coolant ($kg/m^3$)

$\rho_{bi}$ = density of inlet coolant ($kg/m^3$)

$\rho_c$ = density of coolant flow ($kg/m^3$)

$\rho_m$ = density of mainstream flow ($kg/m^3$)

$\rho_f$ = density of film coolant ($kg/m^3$)

$\rho_s$ = density of slot coolant ($kg/m^3$)

$\rho_w$ = density of coolant near the wall ($kg/m^3$)

$\Delta\rho/\rho$ = inlet coolant-to-wall density ratio, $(\rho_{bi}-\rho_w)/\rho_{bi} = (T_w-T_{bi})/T_w$

$\eta$ = film cooling effectiveness or thermal performance, $(Nu/Nu_o)/(f/f_o)^{(1/3)}$

$\Omega$ = rotational speed (rad/s)

# TABLE OF CONTENTS

Page

Page

## LIST OF FIGURES

FIGURE Page

FIGURE Page

FIGURE Page

FIGURE Page

# LIST OF TABLES

# INTRODUCTION

## *Gas Turbine Engines and the Need for Turbine Blade Cooling*

Gas turbines play a vital role in the today's industrialized society, and as the demands for power increase, the power output and thermal efficiency of gas turbines must also increase. One method of increasing both the power output and thermal efficiency of the engine is to increase the temperature of the gas entering the turbine. In the advanced gas turbines of today, the turbine inlet temperature can be as high as 1500°C; however, this temperature exceeds the melting temperature of the metal airfoils. Therefore, it is imperative that the blades and vanes are cooled, so they can withstand these extreme temperatures. Cooling air around 650°C is extracted from the compressor and passes through the airfoils. With the hot gases and cooling air, the temperature of the blades can be lowered to approximately 1000°C, which is permissible for reliable operation of the engine.

It is widely accepted that the life of a turbine blade can be reduced by half if the temperature prediction of the metal blade is off by only 30°C. In order to avoid premature failure, designers must accurately predict the local heat transfer coefficients and local airfoil metal temperatures. By preventing local hot spots, the life of the turbine blades and vanes will increase. However, due to the complex flow around the airfoils it is difficult for designers to accurately predict the metal temperature. Figure 1 shows the

---

This dissertation follows the style and format of the ASME Journal of Turbomachinery.

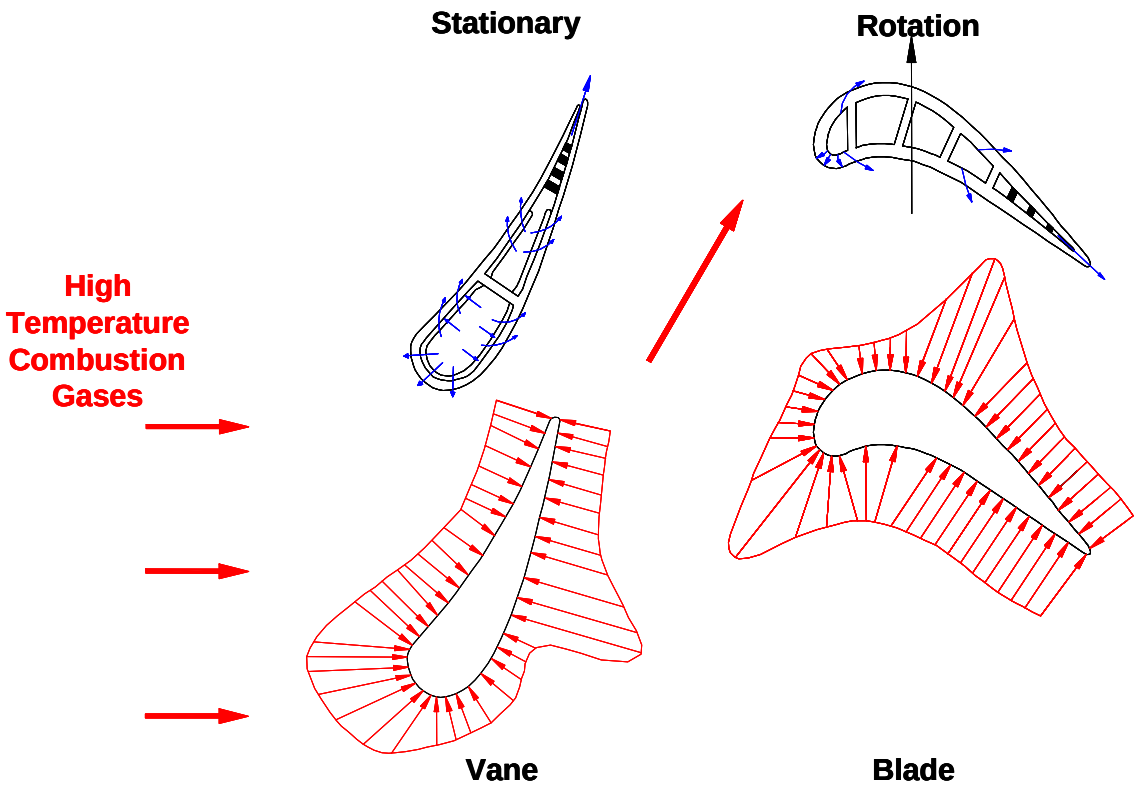


**Fig. 1 Cross-sectional view and heat flux distribution of a cooled vane and blade**

heat flux distribution around an inlet guide vane and a rotor blade. At the leading edge of the vane, the heat transfer coefficients are very high, and as the flow splits and travels along the vane, the heat flux decreases. Along the suction side of the vane, the flow transitions from the laminar to turbulent, and the heat transfer coefficients increase. As the flow accelerates along the pressure surface, the heat transfer coefficients also increase. The trends are similar for the turbine blade: the heat flux at the leading edge is very high and continues decrease as the flow travels along the blade; on the suction surface, the flow transitions from laminar to turbulent, and the heat flux sharply increases; the heat transfer on the pressure surface increases as the flow accelerates around the blade.

Due to the complex flow, designers need data that will aid them in the development of efficient cooling designs. They need detailed hot gas path heat transfer distributions. Heat transfer and film cooling data are also needed for the airfoils. The surface heat transfer on a stator vane is affected by the combustor-generated high turbulence, the laminar-to-turbulent transition, acceleration, film cooling flow, platform secondary flow, and surface roughness. These factors as well as the rotational, centrifugal forces and blade tip clearance and leakage must be considered for the rotating blades.

After the potential hot spots on the airfoil surface are identified, the internal cooling schemes can be developed. Designers need new internal heat transfer data to improve current rotor blade cooling performance. They also need detailed flow and heat transfer data to understand the flow physics and to improve the current internal cooling

designs. Many techniques have been developed to enhance the heat transfer in these passages. The cooling passages located in the middle of the airfoils are often lined with rib turbulators. Near the leading edge of the blade, jet impingement (coupled with film cooling) is commonly used. Jet impingement is also used throughout the cross-section of the stator vanes. Pin-fins and dimples can be used in the trailing edge portion of the vanes and blades. These techniques have also been combined to further increase the heat transfer from the airfoil walls.

A number of traditional cooling concepts are used in various combinations to adequately cool the turbine vanes and blades; these techniques are identified and described throughout this chapter. In addition, newly developed, advanced cooling concepts are also introduced as possible cooling alternatives. The interested reader is referred to *Gas Turbine Heat Transfer and Cooling Technology* by Han et al. [1] for a more in depth description of turbine blade heat transfer and cooling. In addition Lakshminarayana [2] reviewed recent publications involving turbine cooling and heat transfer, and Dunn [3] put together a detailed review of convective heat transfer and aerodynamics in axial flow turbines. A symposium volume discussing heat transfer in gas turbine systems is also available by Goldstein [4].

### *Turbine Blade Platform Cooling*

With the increasing temperature of the mainstream gases exiting the combustor, the stator vanes and rotor blades must be protected, so they can survive the extreme temperatures. Recently, the blade platform has received renewed attention for an

adequate cooling scheme. As shown in Fig. 2, the vane endwall and the blade platforms comprise a large percentage of the area exposed to the hot mainstream gases. There is a strong potential for "hot spots" to form on the endwalls and platforms. Over this large area it is vital to have accurate heat transfer distributions, so efficient cooling schemes can be developed. The cooling schemes should adequately protect the platforms while minimizing the amount of coolant.

A general review of platform (endwall) flow, heat transfer, and film cooling has been completed by Han et al. [1] and Chyu [5]. Several of the papers reviewed by these sources will be considered along with other papers to develop a foundation for platform flow and heat transfer. The secondary flow in a turbine passage is very complex and varies based on the blade profile being considered. Langston et al. [6, 7] performed flow measurements to gain insight into this complex secondary flow. They showed at the inlet of the passage, the boundary splits at the leading edge of the blade. A horseshoe vortex forms with one leg on the pressure side of the blade, and the other leg on the suction side of the blade (in the adjacent passage). The pressure side leg of the horseshoe vortex travels from the pressure side of the passage to the suction side; this pressure side leg of the horseshoe vortex becomes known as the passage vortex. This passage vortex will eventually meet the suction side leg of the horseshoe vortex that has remained near the junction of the suction surface and endwall. Goldstein and Spores [8] also studied the flow through a blade passage. They identified multiple "corner" vortices that developed throughout the passage. A pressure side corner vortex develops

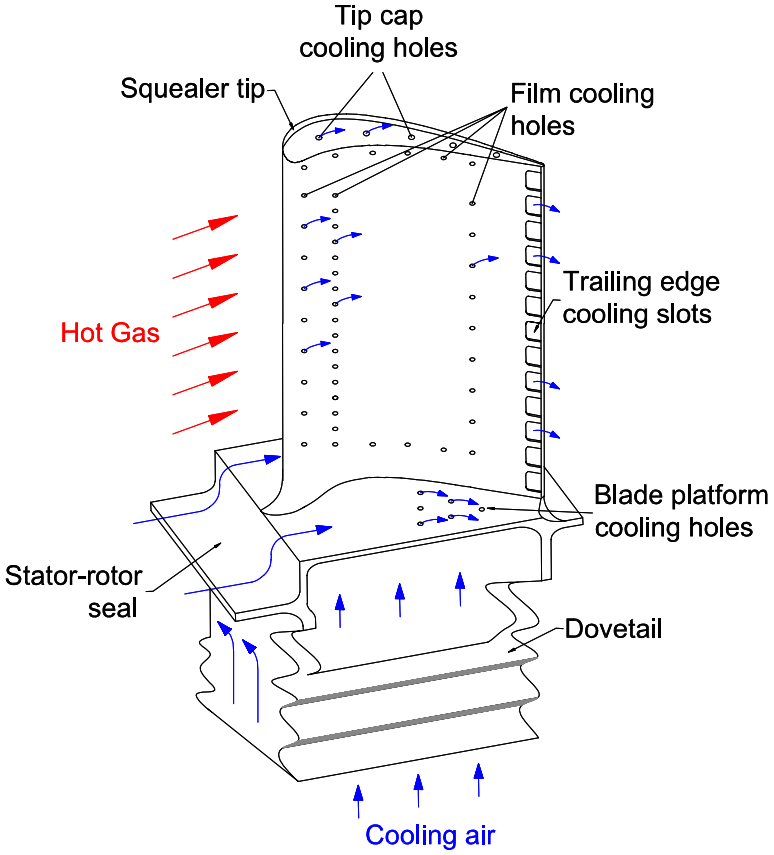


**Fig. 2 Film cooling on a modern gas turbine blade**

just downstream of the leading edge, and the vortex carries about one-third of the chord length. Two suction side corner vortices develop along the suction surface in the latter half of the passage. After the passage vortex carries to the suction side of the passage, it lifts from the endwall surface. Below the passage vortex, along the junction where the suction surface meets the endwall, suction side, counter rotating, corner vortices form.

The highly complex, three-dimensional flow has a strong influence on the heat transferred from the mainstream flow to the blade platform. Blair [9] pioneered the study of endwall heat transfer. He found significant variation of the heat transfer coefficient across the passage and downstream to the trailing edge of the vane due to the secondary flow along the endwall. Graziani et al. [10] also reported large variations in the endwall heat transfer coefficients. They showed the heat transfer coefficients on the suction surface of the blade are also influenced by the secondary flow through the passage; however, the heat transfer coefficients on the pressure surface are not affected by the strong secondary flows. Using a mass transfer technique, Goldstein and Spores [8] showed as the boundary layer splits to form the two legs of the horseshoe vortex near the leading edge of the blades, the heat transfer coefficients increase, and the greatest heat transfer enhancement on the endwall occurs near the leading edge. Other variations are present on the endwall due to the path of the passage and corner vortices. In addition near the trailing edge of the blade, the heat transfer coefficients are elevated as the two flows from the two passages meet at the trailing edge. The heat transfer coefficients were also measured on the endwall of a vane passage [11 – 13]. Similar variations were found, as the heat transfer continues to be dominated by the secondary flow. When the

effect of freestream turbulence was considered [12, 13], it was found that increasing the turbulence intensity increases the heat transfer coefficients on the passage endwall. However, the effect of the freestream turbulence intensity was minimal near the leading edge and the near the suction surface, where the horseshoe and passage vortices dominate the heat transfer behavior.

With the local areas of high heat transfer identified, film cooling can be implemented on the blade platform to reduce the heat load in these areas. Takieshi et al. [14] obtained heat transfer and film effectiveness distributions on a vane endwall with discrete film cooling holes placed at three locations in the passage. They found that the effectiveness is very low near the leading edge on the suction side; with the rollup of the horseshoe vortex, the film coolant lifted from the surface, and offered little or no protection. The path of the coolant was also influenced by the passage vortex transporting the coolant from the pressure to the suction side of the passage. Harasgama and Burton [15] used film cooling near the leading edge, just inside the passage, with the film cooling holes located along an iso-Mach line. Although the row of film cooling holes was evenly distributed to span the passage, no coolant reached the pressure side of the passage. The film cooling configuration used by Jabbari et al. [16] consisted of discrete holes placed on the downstream half of the passage. Similar to the upstream design [15], the film cooling effectiveness varied significantly through the passage, with the coolant moving to the suction side of the passage.

Friedrichs et al. [17 – 19] studied the film cooling effectiveness using the ammonia and diazo technique. They found that a simple layout of the film cooling holes

throughout the passage can result in areas being over cooled (or under cooled) due to the secondary flow. With their proposed "improved design," the film holes were placed, so the strong secondary flow could be used advantageously. Using the same amount of coolant, they were able to provide improved coolant coverage. Recently, Barizozzi et al. [20] compared the film cooling effectiveness on a passage endwall with cylindrical or fan-shaped film cooling holes. With their cooling designs, they showed that by increasing the blowing ratios, the passage vortex is weakened, and the passage cross flow is reduced; therefore, coolant coverage is more uniform across the passage. Similar to flat plate film cooling, shaped film cooling holes offer better protection than cylindrical holes.

A similarity between the vane endwall and the blade platform is the existence of slot (or gap) upstream of the airfoil leading edge. A gap is commonly in place in the transition from the combustion chamber to the turbine vane (stator). Similarly, a gap exists between the stator and rotor, so the turbine disk can rotate freely. To prevent ingestion of the hot mainstream gases, it is a common practice to inject coolant air through these slots. If this preventive measure is utilized properly, unnecessary discrete film holes can be eliminated, so coolant is not wasted by overcooling areas on the rotating platform. Blair [9] also measured the film cooling effectiveness with upstream injection in his pioneering study; he showed large variations in the film cooling effectiveness over the entire passage due to the strong secondary flow. Roy et al. [21] placed coolant slots upstream of their vane. They showed the heat transfer near the leading edge was reduced due to the secondary air injection. Because the slots were

placed directly upstream of the blades, a large area in the center of the passage did not receive adequate film cooling coverage. Slot injection has been the focus of many studies performed at the University of Minnesota [22 – 24]. They found using slots, which span the majority of the passage upstream of their vanes, can provide film coverage over most of the passage to the trailing edge of the vane [22, 23]. They also found that increasing the amount of coolant through the slot can reduce the effect of the secondary flow. In addition, strategically blocking the slot, so the coolant does not exit the slot uniformly provides thermal advantages (and disadvantages) [24].

The heat transfer coefficients and the film cooling effectiveness were measured on the endwall of a vane passage with film cooling combined with upstream slot injection by Nicklas [25]. They found that in the upstream region, the film cooling effectiveness was elevated due to the large amount of cooling flow from the slot. However, the effectiveness near the discrete holes located near the center of the passages suffered due to the passage vortex. Liu et al. [26] used a high volume of discrete holes upstream of their vanes to emulate the effect of upstream slot injection. They determined the film cooling effectiveness was primarily affected by the blowing ratio of the injection; in addition, as the blowing ratio increases, the uniformity of the coverage increases.

The film cooling effectiveness has been measured using pressure sensitive paint by Zhang and Jaiswal [27] and Zhang and Moon [28]. They first measured the effectiveness with two upstream injection geometries: two rows of discrete holes and a single row slot. The effect of a backward facing step was also considered with the

discrete hole configuration. They confirmed that increasing the coolant flow can significantly increase the effectiveness, and they reported that the use of a backward step significantly decreases the effectiveness within the passage. Knost and Thole [29] showed that with increased slot flow, the critical areas of the leading edge and pressure side junction can be adequately cooled. Cardwell et al. [30] extended this work to include mid-passage misalignment. With the misalignment that may occur between two adjacent vanes, the film cooling effectiveness is dramatically reduced.

With the secondary flow strongly influencing both the heat transfer coefficients and the film cooling effectiveness on the platform surface, recently, efforts have been directed at mitigating this destructive secondary flow. One method that is gaining popularity is endwall contouring [31, 32]. Han and Goldstein [33] observed that with a fillet around the leading edge of the blade, the horseshoe vortex disappears, and the passage vortex is delayed with elevated turbulence intensity. However, with low freestream turbulence, the strength of the passage vortex is comparable to that in a passage without the fillet. The drawback of the fillet is the increased heat transfer near the leading edge on the pressure side due to the intensified corner vortices.

### *Internal Turbine Blade Cooling*

With internal cooling, pressurized cooling air is extracted from the compressor and injected into the turbine blade. The coolant circulates through cooling passages to remove heat from the blade. Figure 3 shows that pin-fin cooling is commonly used in the

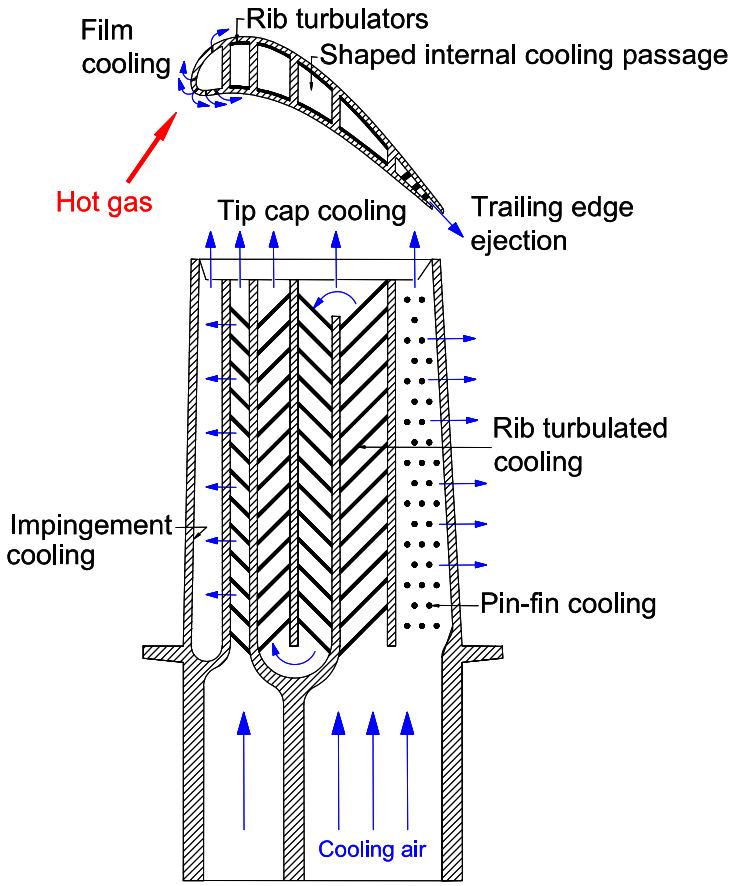


**Fig. 3 Internal cooling techniques applied to a modern gas turbine blade**

trailing edge. These pin-fins not only enhance the heat transfer but also provide the structural support to the thin blade. Jet impingement cooling is the most effective technique to enhance the heat transfer, but these holes weaken the structural strength. Thus, jet impingement cooling is used in the leading edge where the thermal loads are high. Rib turbulators are often used to cool the mid portion of the blade. As the turbine blade rotates, Coriolis and rotational buoyancy forces alter the flow field of the cooling air through the cooling channels, which cause significantly different heat transfer distributions between the leading and trailing surfaces of the channel. These Coriolis and rotational buoyancy forces shift the coolant toward the trailing surface for the radially outward flow; thus heat transfer increases from the trailing surface, and decreases from the leading surface.

The shape and orientation of the cooling channels within the turbine blade vary from the leading edge to the trailing edge of the blades. As the blade becomes thinner toward the trailing edge, the cooling channels become narrower, and the orientation angle ($\beta$) of the channel increases. The knowledge of the flow field induced by rotation in channels with smaller aspect ratios (AR ~ 1:1) cannot simply be applied to large aspect ratio channels. However, the availability of literature is limited concerning the heat transfer distribution for large aspect ratio channels. Therefore, it is necessary to investigate the heat transfer distribution for these narrow channels in the trailing edge portion of the blade.

A comprehensive review of turbine blade internal cooling can be seen in *Gas Turbine Heat Transfer and Cooling Technology* by Han et al. [1]. The book includes

numerous studies that have been conducted over the years on a wide range of rib configurations in various size cooling channels using many experimental techniques. Early studies investigated cooling channels with orthogonal ribs (Han [34]). It was then determined that placing the ribs at an angle to the mainstream flow will result in greater heat transfer enhancement than ribs positioned at 90° to the mainstream flow. Studies by Han and Park [35] and Park et al. [36] investigated the thermal performance of angled ribs compared to orthogonal ribs. The results showed the heat transfer enhancement in angled rib channels is significantly greater than the heat transfer enhancement due to normal ribs.

The focus of rib turbulators began to shift to the investigation of "high performance" ribs. Han et al. [37] studied a square channel with V, Λ, parallel (angled), and crossed ribs. They showed the V-shaped ribs (45° and 60°) perform better than the parallel ribs (45° and 60°).

Using the mass transfer technique, Lau et al. [38] found the V-shaped ribs create the greatest heat transfer enhancement; however, they also create the greatest pressure drop. Their results showed that the V-shaped ribs and the full (angled) ribs had comparable thermal performances.

Han and Zhang [39] then completed a study of a square channel with various angled and V-shaped rib configurations. They concluded that broken ribs (similar to discrete ribs) create heat transfer enhancement levels of 2.5 ~ 4, while the enhancement created by the continuous ribs is only 2 ~ 3. Both the broken and continuous ribs incur a pressure penalty of 7 ~ 8 times.

Taslim et al. [40] studied various configurations of angled and V-shaped ribs using a liquid crystal technique. They also concluded that V-shaped ribs result in the greatest heat transfer enhancement while having the greatest pressure loss. Ekkad and Han [41] also used a liquid crystal technique to obtain detailed heat transfer distributions in a two-pass channel with parallel (angled), V-shaped, and broken V-shaped (discrete V-shaped) ribs. They concluded that the parallel, V-shaped, and broken V-shaped ribs produce similar heat transfer enhancement in the first pass, with the broken V-shaped ribs giving slightly higher enhancement.

Cho et al. [42] recently investigated angled and discrete angled ribs using mass transfer. They concluded that the heat transfer performance of the discrete ribs is similar to that of the angled ribs in a rectangular channel with an aspect ratio of 2.04:1. A very narrow channel (AR = 8:1) with V-shaped, Λ-shaped, and angled ribs was studied by Gao and Suden [43]. Using a liquid crystal technique, they too confirmed that V-shaped ribs result in the highest heat transfer enhancement and the highest frictional losses. They concluded that the V-shaped ribs yield the best overall thermal performance. Rhee et al. [44] also investigated rectangular channels (AR = 3:1, 5:1, and 6.82:1). They studied the thermal performance of V-shaped and discrete V-shaped ribs. Based on their configurations, they concluded the thermal performance of the two configurations were comparable.

All of the above studies focus on the performance of various configurations of ribs in non-rotating channels. Many studies have been performed that investigate the effect of rotation on cooling channels. Johnson et al. [45] experimentally investigated

the heat transfer in multi-pass rotating channels with angled ribs. Johnson et al. [46] performed additional tests with this four-pass test duct to determine the effect of channel orientation on the heat transfer enhancement. From these studies it was concluded that the heat transfer from both the leading and trailing surfaces of the ribbed channel was different from that of a non-rotating channel.

Parsons et al. [47, 48] also studied the influence of channel orientation and wall heating condition on the regionally averaged heat transfer coefficients in a rotating, two-pass square channel with 60° and 90° ribbed walls. This study showed the heat transfer coefficients are greater in channels that are maintained at a constant wall temperature. They found this difference is greater for the channel oriented at 45° than the channel oriented perpendicular to the direction of rotation.

Dutta and Han [49] conducted an experimental study of regionally averaged heat transfer coefficients in rotating smooth and ribbed two-pass channels with three channel orientations. They found the effect of rotation is reduced for non-orthogonal alignment of the heat transfer surfaces with respect to the plane of rotation. They also concluded that the staggered half V-shaped ribs (comparable to the discrete V-shaped ribs of the present study) have better heat transfer performance than the 90° ribs and the 60° angled ribs.

Park et al. [50, 51] conducted naphthalene sublimation experiments to examine the effects of rotation on the local heat and mass transfer distribution in a two-pass ribbed square channel. They also found that the overall heat and mass transfer in a

rotating channel with ribbed surfaces was not affected by the Coriolis force as much as that in a rotating channel with smooth surfaces.

Due to the curved shape of a turbine blade, cooling channels near the trailing edge are rectangular and the orientation angle of the channel increases. The heat transfer trends in a square channel cannot simply be applied to rectangular channels. The effect of the Coriolis and rotational buoyancy forces is altered by the larger aspect ratios and orientation angles. Recently, more studies have focused on these rectangular channels.

Taslim et al. [52, 53] investigated the heat transfer distribution in rotating square and rectangular rib-roughened channels using a liquid crystal technique. They found that the effects of rotation were more apparent in rib-roughened channels with a larger channel aspect ratio and a lower rib blockage ratio.

Kiml et al. [54] examined the heat transfer and pressure drop in a ribbed rectangular channel (AR=2:1) for four rib configurations. (90°, 75°, 60°, and 45° angled ribs). They revealed that 60° ribs produce the highest heat transfer enhancement due to the strong rotational momentum of the rib induced secondary flow. Kiml et al. [55] also investigated heat transfer enhancement mechanisms in rectangular channels with V and Λ−shaped ribs using a flow visualization technique to examine the secondary flow behaviors created by the V−shaped ribs.

Azad et al. [56] conducted an experimental study to determine heat transfer enhancement in a rotating two-pass ribbed rectangular channel with an aspect ratio of 2:1. They showed that the heat transfer decreases from the leading surface and increases

from the trailing surface for the first passage. They also found the 90°-channel orientation produces a greater rotation effect than the 135° channel orientation.

Al-Hadhrami et al. [57, 58] studied the effect of rotation on heat transfer in rotating, two-pass square and rectangular channels (AR=2:1) with rib turbulators for two channel orientations. They found that the parallel and V-shaped ribs produce better heat transfer enhancement than the crossed and inverted V-shaped ribs. They also found that parallel angled ribs produce better heat transfer enhancement than the crossed angled ribs. Furthermore, the 90°-channel orientation produces a greater rotation effect on the heat transfer than a 135°-channel orientation.

Griffith et al. [59] investigated the effect of rotation on heat transfer in a rib-roughened rectangular channel (AR=4:1). They found that the narrow rectangular passage exhibits much higher heat transfer enhancement for the ribbed surfaces than the ribbed surfaces in a smaller aspect ratio channel. They also found spanwise heat transfer distributions exist across the leading and trailing surfaces, and the variation is accentuated by the use of angled ribs. Also, they showed the orientation of the channel significantly effects the heat transfer distribution.

Lee et al. [60] also investigated the heat transfer performance of various rib configurations in a rotating rectangular duct with an aspect ratio of 4:1. They concluded that V-shaped ribs have superior heat transfer performance to the angled rib configurations. This is true for both non-rotating and rotating channels.

More recent studies have begun to focus on the leading edge of the blade. Cho et al. [61] used mass transfer to study the effect of rotation in a rotating two-pass

rectangular channel (AR=1:2) with 70° angled ribs. Agarwal et al. [62] used mass transfer to study a two-pass 1:4 rotating channel. In both channels with smooth walls and 90° angled ribs, they found that the heat/mass transfer in the 1:4 channel is less than that of a square channel.

The cross-section of the internal cooling passages is limited by the size and shape of the turbine blade. Just as the cross-section of the cooling passages are adapted to fit the cross-section of the blade, the length of the cooling channel must also be adapted to meet spatial limitations in the streamwise direction. In other words, the coolant used to internally cool the blade typically does not travel through a single, straight, constant diameter duct. The coolant could be forced to travel through any of a variety of entrance sections, within the dovetail of the blade, before entering the actual cooling channel. Rather than flow being developed upon entering the blade (as in the studies listed above), in most cases the flow must develop both thermally and hydrodynamically within the turbine blade.

A number of studies have investigated the developing flow in various channels. Studies have involved the development of both the thermal and hydrodynamic boundary layers in smooth channels and channels with various rib configurations. However, the studies that involve the entrance effect within cooling channels with rib turbulators are limited to flow through a sudden contraction. Furthermore, all the previous studies of developing flow have a common tie: the effect of the entrance geometry is investigated for non-rotating cooling channels.

Kays and Crawford [63] summarized and presented the work of Boelter et al. [64] regarding developing flow. In this study, the heat transfer within a non-rotating circular tube was measured for various entrance configurations. The entrance length of the heated circular tube is dependent upon the selected entrance geometry. The local Nusselt number ratio for flow through bends or an abrupt contraction is substantially greater than hydrodynamically fully developed flow. The effect of the entrance also has as a substantial effect on the mean Nusselt number ratio in the smooth channels. The mean Nusselt number ratio for flow through the abrupt contraction can be six percent greater than fully developed flow; this increase is primarily attributed to the entrance of the channel where both the thermal and hydrodynamic boundary layers are developing.

Burggraf [65] investigated the effect of entrance flow on the heat transfer in both non-rotating smooth square channels and square channels with rib turbulators oriented 90° to the mainstream flow. The entrance geometries of this study consisted of a long unheated duct which allowed the flow to hydrodynamically develop before entering the heat test section, a short entrance duct (which is similar to a contraction), and a 180° turn positioned immediately upstream of the heated test section. These results showed the heat transfer distributions in the channel with a long entrance and a channel with a short entrance follow the same trends. The heat transfer coefficients (for both cases) are elevated at the cooling channel entrance, and the coefficients decrease to the fully developed value, which is achieved approximately 3.3 hydraulic diameters downstream of the start of the heated test section. His results also showed that the heat transfer coefficients in the channel with the short entrance are approximately 5% greater than

those of the long entrance. However, the heat transfer coefficients at the entrance of the channel with the bend can be up to 38% greater than those of the long entrance. This study also showed the heat transfer coefficients within the channel with the bend were always greater than those of the long channel. The results also show as the Reynolds number increases, the difference between the long entrance and the other two entrances decreases.

Han and Park [35] investigated developing heat transfer in non-rotating rectangular channels. In this study, a variety of rib configurations and channel cross-sections were studied. The coolant flowed through a plenum and into the rectangular test section. The plenum was sufficiently larger than the test section, so the fluid was forced through a contraction and into the test section. From this study they found that in a stationary rectangular (AR = 4:1) channel with angled ribs, the Nusselt number decreases in the streamwise direction from the sharp entrance but increases again at $x/D_h \approx 3$ because of the secondary flow induced by the rib angle. The Nusselt number then remains relatively constant throughout the remaining length of the channel.

Liou and Hwang [66] also investigated the effect of entrance geometry in non-rotating rectangular channels with rib turbulators. They found for ribbed channels the first 12-18 percent of the channel is affected by the abrupt contraction. From this study, they also developed a correlation for developing flows in a ribbed channel with an abrupt contraction. This correlation is independent of the Reynolds number and the rib pitch-to-height ratio.

Park et al. [36] investigated the heat transfer performance of various rib configurations in non-rotating rectangular cooling channels; five different aspect ratio channels were studied with a variety of rib orientations for each channel. The coolant was forced through a contraction before entering the heated test section. The Nusselt number ratio gradually decreases in the entrance portion of the heated test section. In the rib-roughened channels, the ratio becomes fully developed approximately two diameters downstream of the entrance.

### *Objectives of the Current Experimental Study*

Fundamentally, the objectives of this research program are to increase the power output and efficiency of gas turbine engines. This can be achieved by increasing the temperature of the mainstream gases entering the engine's high pressure turbine. However, the metallic components must be capable of withstanding these extreme temperatures. This study will experimentally investigate several cooling techniques and their applicability to gas turbine cooling.

Because the blade platform comprises a significant percentage of the area exposed to the mainstream flow, the entire area must be adequately protected. However, the mainstream flow near the platform is very complex and offers many challenges in order to assure the area is properly protected. With the construction of the engine, a gap exists between the stator and rotor to allow the blades to rotate. Purge flow through this gap is used to ensure the hot gases are not ingested into the engine cavity. The present experimental study will study a variety of gap and seal geometries to determine the

viability of this purge flow doubling a protection for the blade platform. If the purge flow can be properly utilized, additional coolant is not required. Minimizing the amount of air extracted for cooling also serves to increase the engine efficiency.

Heat is also removed from the airfoils by the coolant circulating through the internal cooling passages. Designers would like to remove as much heat as possible while using a minimal amount of cooling air. To do this, high performance turbulators must be employed to increase the level of heat transfer enhancement within these internal cooling channels. However, the level of heat transfer enhancement is influenced by more than simply the turbulator design. Because the airfoils are rotating in the engine, the effect of rotation must be considered to give an accurate portrayal of the heat transfer enhancement within the channel. This study will also experimentally study the effect of rotation on heat transfer enhancement in trailing edge cooling channels, so turbulator designs can be selected which yield increased heat transfer enhancement at a minimal cost.

# STEADY STATE FILM COOLING EFFECTIVENESS MEASUREMENT TECHNIQUES

## *Pressure Sensitive Paint (PSP) Theory and Measurement*

Pressure sensitive paint is a relatively new measurement technique based on luminescence quenching [67]. Luminescent molecules are suspended in a polymer binder to form the paint. The molecules are excited by light at an appropriate wavelength, and the excited molecules emit light at a longer wavelength. As applied to PSP, the luminescent intensity of the light emitted by the paint can be related to pressure.

As shown in Fig. 4, the luminescent molecules are suspended in the polymer binder. This binder is permeable, allowing oxygen molecules to penetrate into the paint, and interact with the luminescent molecules. An excited molecule rises to an upper singlet energy state, and a photon of a longer wavelength is emitted as the molecule returns to its ground state. In the presence of oxygen, the transition to back to the ground state is radiationless; this process is known as oxygen-quenching [68]. At higher partial pressures of oxygen, more quenching of the luminescent molecules occurs, and thus the intensity of the emission light decreases.

The functionality of the PSP is enhanced by introducing a reference condition. For the present application, atmospheric pressure is used as the reference condition. With this reference condition, the emission intensity at any pressure is related to the emission intensity at the reference pressure as shown in Eq. (1).

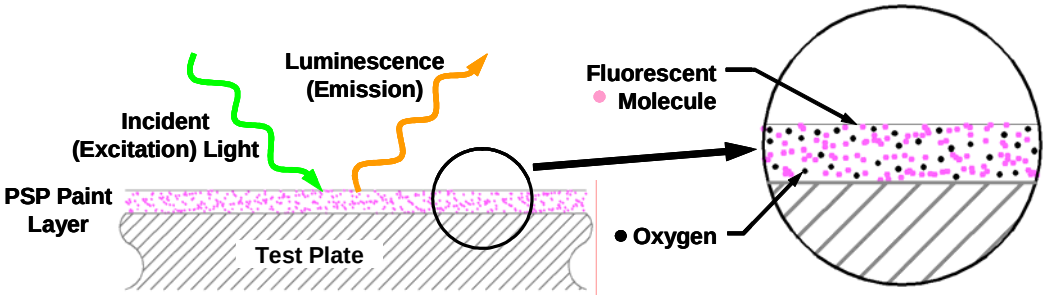


**Fig. 4 Pressure sensitive paint (PSP) model**

$$\frac{I(P)_{ref}}{I(P)} = f\left(P; P_{ref}\right) \tag{1}$$

However, due to the inherent noise associated with optical components, it is necessary to eliminate the background intensity using black images (no excitation light). With the removal of the background intensity, the intensity ratio becomes

$$\frac{I(P)_{ref} - I_b}{I(P) - I_b} = f\left(P; P_{ref}\right) \tag{2}$$

Before PSP can be applied to a test surface in a wind tunnel or other application, it must first be calibrated to determine the relationship between the intensity ratio and the pressure ratio. To perform the calibration, a vacuum chamber is used to control pressure, and the PSP was calibrated from 2.35 – 14.696 psia (16.2 – 101.3 kPa). A test plate was sprayed with Uni-FIB pressure sensitive paint (UF470-750) supplied by Innovative Scientific Solutions, Inc. (ISSI). At each measurement point, the PSP sample was excited using a strobe light with a wavelength of 520 nm. A CCD (charged-couple device) camera with a 610 nm filter records the intensity of the light emitted by the PSP. Black images are also recorded to remove the background intensity. Figure 5 shows the calibration curve developed for the specified PSP at the room temperature of 22°C.

Care must be taken during the calibration to ensure the PSP is calibrated at the same temperature at which it will be used during actual tests. The emission intensity of the luminescent molecules is affected by temperature in two ways [68]. First, just as the molecules return to their ground state in the presence of oxygen, they also are more likely to return to their ground state at elevated temperatures. Also, most polymer binders are temperature sensitive; the permeability of the binder changes with

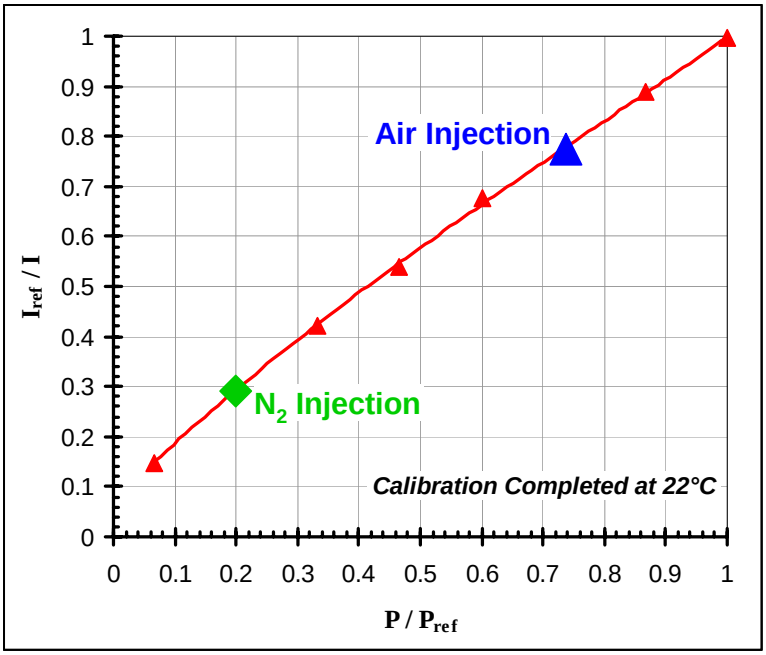


**Fig. 5 PSP calibration curve**

temperature changes. PSP experiments must be performed in isothermal environments, or large errors in the pressure measurements can result from variations in temperature which are not taken into account.

After the PSP has been properly calibrated, it can be applied to the test surface. The film cooling plate inside the wind tunnel is coated with PSP, and the excitation light and camera are positioned, so the emission from the entire surface is recorded with one image. Figure 6 shows the basic setup for PSP measurements, including the test surface and optical components. Because the focus of this study is to determine the film cooling effectiveness, rather than the surface pressure distribution, an additional element is added to the experiment. The film effectiveness is calculated based on the concentration differences created by air coolant injection and nitrogen coolant injection. Therefore, to accurately determine the film cooling effectiveness, four images are required. The first image is the reference image; with this image the PSP is excited with the light source, but there is no mainstream or coolant flow. The second image is the black image; as with the calibration, this image is required to eliminate any noise in the images. The third image is an air image. This image is taken with mainstream and coolant flow, and the coolant through the film cooling holes is air. The fourth and final image is the nitrogen image. Similar to the air image, this image is recorded with mainstream and coolant flow, but now the coolant flow is pure nitrogen ($N_2$).

Expanding Eq. (2) to include both images with air and nitrogen injection, the intensity ratios are re-written in Eqs. (3) and (4).

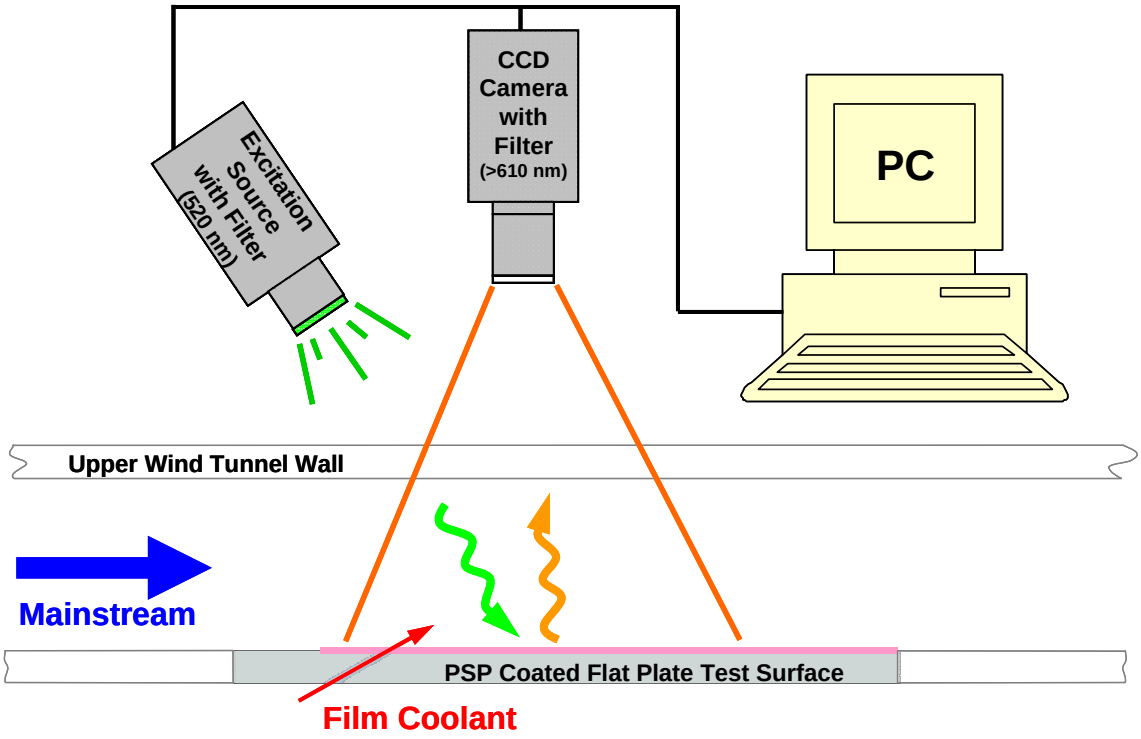


**Fig. 6 Typical PSP experimental setup**

$$\frac{I(P)_{ref} - I_b}{I(P)_{air} - I_b} = f\left(\left(P_{O_2}\right)_{air}; P_{ref}\right) \quad or \quad f\left(P; P_{ref}\right) \tag{3}$$

$$\frac{I(P)_{ref} - I_b}{I(P)_{mix} - I_b} = f\left(\left(P_{O_2}\right)_{mix}; P_{ref}\right) \tag{4}$$

$I(P)_{air}$ is the intensity recorded during the test with air injection, and $I(P)_{mix}$ is the intensity recorded from the test with nitrogen used as the coolant. From the calibration of the PSP, the partial pressure of oxygen on the test surface with both air and nitrogen injection can be calculated. Finally, the film cooling effectiveness is related to the partial pressure of oxygen measured with both air and nitrogen oxygen [27].

$$\eta = \frac{C_\infty - C_{mix}}{C_\infty} = \frac{\left(P_{O_2}\right)_{air} - \left(P_{O_2}\right)_{mix}}{\left(P_{O_2}\right)_{air}} \tag{5}$$

The partial pressure of oxygen with air and nitrogen injection is determined based on the calibration of emission intensity and pressure. With Eq. (5) combined with the PSP calibration, the film cooling effectives can be determined at every pixel giving detailed film cooling effectiveness distributions on the surface of the flat plate, as approximated by Eq. (6).

$$\eta \approx 1 - \frac{I_{air}}{I_{N_2}} \tag{6}$$

***Temperature Sensitive Paint (TSP) Theory and Measurement***

Like PSP, temperature sensitive paint (TSP) is also comprised of luminescent molecules suspended in a polymer binder. However, the photophysical process

associated with TSP is thermal quenching, rather than oxygen quenching. Unlike with PSP, the polymer binder is not oxygen permeable, as shown in Fig. 7. Therefore, the luminescence intensity of the TSP is related only to temperature, and is not a function of pressure (unlike the reverse relationship observed with PSP). Like PSP, the luminescent molecules in the TSP must be excited with the absorption of a photon. The molecules return to their ground state with the emission of the photon at a longer wavelength. Increasing the temperature of the luminescent molecules makes the molecules more likely to return to their ground state (releasing the photon through a radiationless process) [69]. Therefore, the emission intensity from molecules at elevated temperatures is lower than the emission of molecules at relatively lower temperatures. This photophysical process is known as thermal quenching.

Similar to the use of PSP, a reference condition is used for the TSP measurements. Typically, the reference condition is set at the room temperature in which the experiments are performed. However, for cryogenic applications, the reference temperature maybe much lower. With the reference condition, and the black image used to eliminate the background intensity from the optical components, the emission intensity is related to the surface temperature as shown in Eq. (7).

$$\frac{I(T)-I_b}{I(T)_{ref}-I_b}=f(T) \tag{7}$$

A calibration must be completed to determine the relationship between the emission intensity and the surface temperature. The calibration is completed by attaching a thermocouple to the surface of a copper block. The copper block is coated

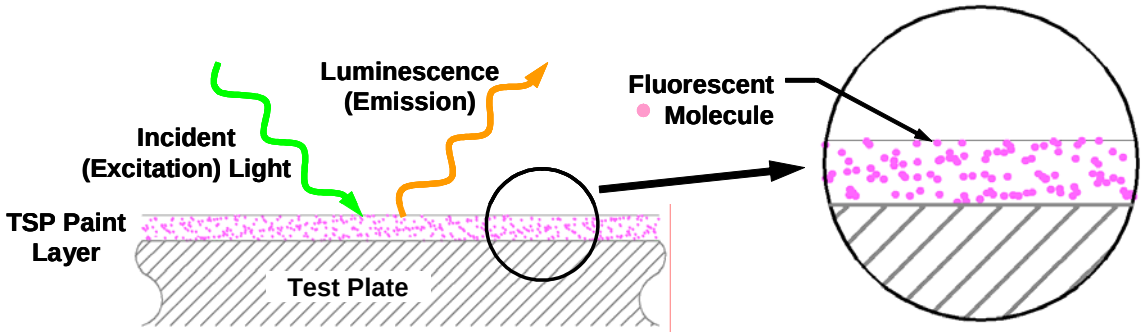


**Fig. 7 Temperature sensitive paint (TSP) model**

with the TSP, and positioned between the excitation light and CCD camera. UniCoat TSP from ISSI is sprayed on the copper plate; the same strobe light for excitation and camera used with PSP are now used with TSP. The copper block is heated from room temperature up to 145°F (24 - 63°C). At specific temperatures, the emission intensity is recorded (coupled with black images), so a relationship between the intensity and temperature can be determined. Figure 8 shows the calibration curve developed for this TSP with 23.9°C used as the reference temperature.

After completion of the TSP calibration, the TSP can be applied to the film cooling plate inside the wind tunnel. The experimental setup is identical to the PSP setup shown in Fig. 9. However, the experimental procedure to determine the film cooling effectiveness with TSP is quite different from the procedure used with PSP. As the name implies, TSP detects changes in temperature; therefore, this method requires a temperature difference. For this study, TSP is used to measure the steady state surface temperature. The surface is heated via hot air injected through the coolant holes. The coolant air is hot, while the mainstream flow is unheated, so the mixing of the mainstream and coolant flows results in temperature variations on the surface of the plate. With a plexi-glass test plate, the surface temperature measured by the TSP is also known as the adiabatic wall temperature, $T_{aw}$. From the measured adiabatic wall temperature, coolant temperature, and mainstream temperature, the film cooling effectiveness can be calculated with Eq. (8).

$$\eta = \frac{T_{aw} - T_m}{T_c - T_m} \tag{8}$$

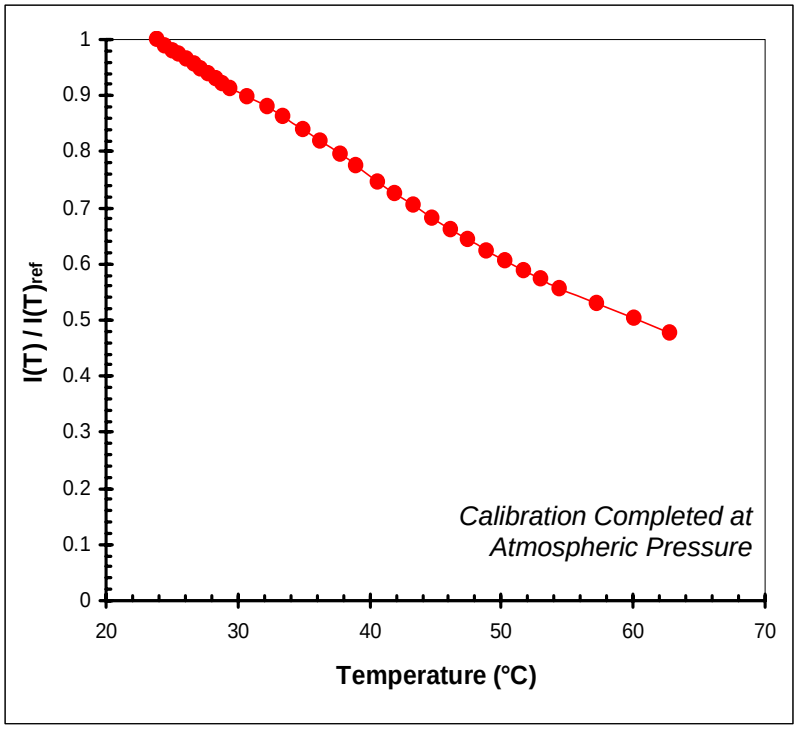


**Fig. 8 TSP calibration curve**

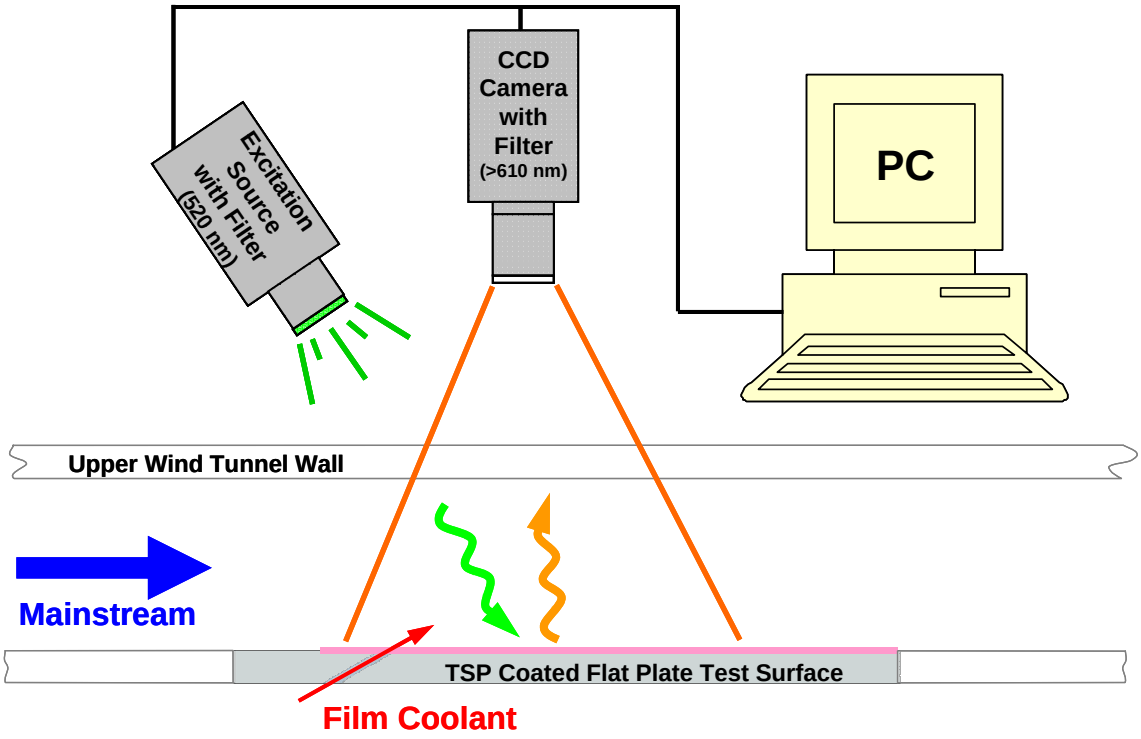


**Fig. 9 Typical TSP experimental setup**

During the actual film cooling experiment, only three images are required: black image (no flow, no excitation light), reference image (no flow, with excitation light), and air image (mainstream and coolant flows, with excitation light). With these images, and the calibration data, the adiabatic wall temperature can be determined. If the reference image corresponds to a different temperature than the reference image from the calibration, this must be taken into account. With a temperature being recorded at every pixel in the viewing window, detailed distributions of the film cooling effectiveness can be obtained on the film cooling plate.

### *Infrared Thermography Theory and Measurement*

The final steady state measurement technique considered in this study is infrared (IR) thermography. IR cameras have been used to measure surface temperatures for many years. Although this measurement technique has been practiced for many years, it is gaining popularity as a method to obtain detailed surface temperature distributions. The current laboratory utilizes a Mikron Thermo Tracer 6T62 to measure the surface temperatures. The IR-system consists of an optical scanner which directs the incoming infrared radiation line by line onto the detector working in a wavelength bandwidth of 8 – 13 microns. The IR camera views the test surface through a sheet of Vinylidene Chloride-Vinyl Chloride co-polymer (Saran Wrap food wrap) which serves as an infrared window in the top wall of the wind tunnel.

The camera was calibrated with the Saran Wrap in place to account for any bias of the detector sensitivity resulting from minor infrared absorptions. The calibration

procedure is similar to the one used for the TSP calibration. A thermocouple was attached to the surface of the copper block, and the copper block was painted black (increasing the emissivity). Temperatures recorded by the thermocouple were compared to temperatures recorded by the IR camera. The relationship between the thermocouple and IR measurements is shown in Fig. 10. A one-to-one relationship between the thermocouple and IR measurement is also shown as a reference. As the temperature increases, the difference between the IR and thermocouple measurements increases. For the present case, the coolant temperature is heated to 43.3°C, so the surface temperature measurements are always on the lower half of the curve, where there is less variation between the measurements. With this calibration curve, the data obtained from the IR camera in the actual film cooling experiment was corrected.

The basic components used for the IR experiment are shown in Fig. 11, with the experimental procedure for the steady state IR experiment being the same as for the TSP experiment. The coolant flow is heated while the mainstream is unheated. From the mixture of the hot coolant and cold mainstream, the film effectiveness on the plate surface can be calculated using Eq. (8). From the detailed surface temperature distributions provided by the IR camera and the calibration, the effectiveness at every pixel can be calculated.

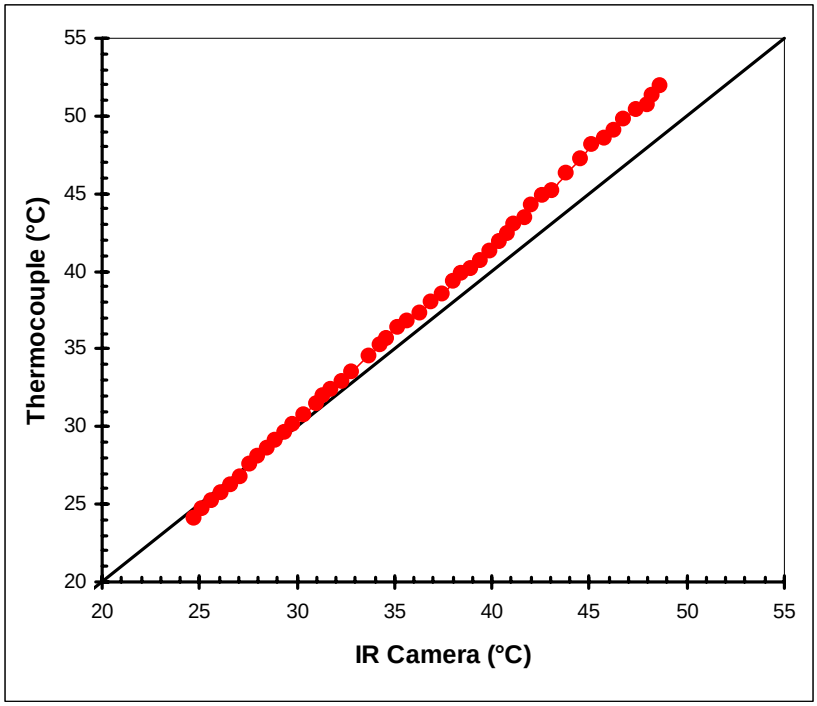


**Fig. 10 IR calibration curve**

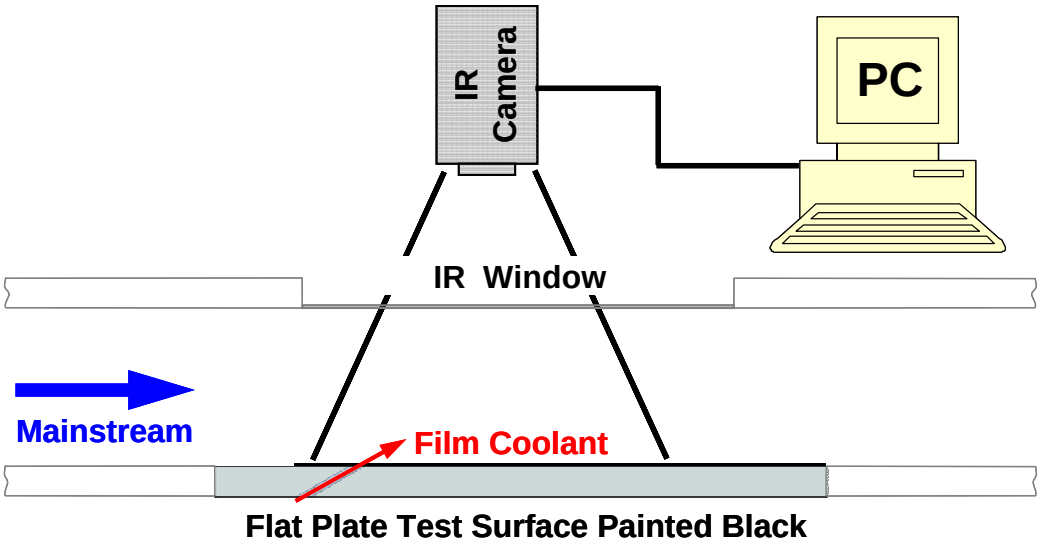


**Fig. 11 Typical IR experimental setup**

### *Measurement Technique Evaluation on a Flat Plate*

*Experimental Facilities (Low Speed Wind Tunnel with Film Cooled Flat Plate)*

A low speed suction-type wind tunnel with a velocity of 25 m/s is used for this study. The 4:1 contraction ratio of the nozzle produces uniform flow at the entrance of the test section. The wind tunnel has an inlet cross-section of 60.96 cm x 30.48 cm. A 5 μm cotton filter and packed plastic straw flow straightener box are installed in front of the nozzle inlet. The test channel cross section is 30.48 cm x 15.24 cm. The wind tunnel operates in the suction mode with a 5.6 kW axial blower. A central air-conditioning system maintained the mainstream temperature at 22°C. A turbulence grid is set upstream of the test surface which creates a turbulence intensity of 6% near the film cooling test plate; without the turbulence grid the freestream turbulence is approximately 0.5% near the film cooling holes. It is composed of a square mesh of aluminum tubes—thirteen tubes in the vertical direction and seven tubes in the horizontal direction. The diameter of each tube is 0.635 cm, so the turbulent length scale near the film cooling holes is approximately 1 cm. Figure 12 shows a 3-D model of the wind tunnel.

The coolant air, supplied from a compressor or nitrogen tank depending on the measurement technique, passes through a flow control valve and orifice flow meter. The coolant then passes through a 5 kW pipe heater and bypass valve before it enters the air plenum, which is directly underneath the film-cooling plate. For all measurement techniques, a T-type thermocouple is used to measure the inlet mainstream temperature.

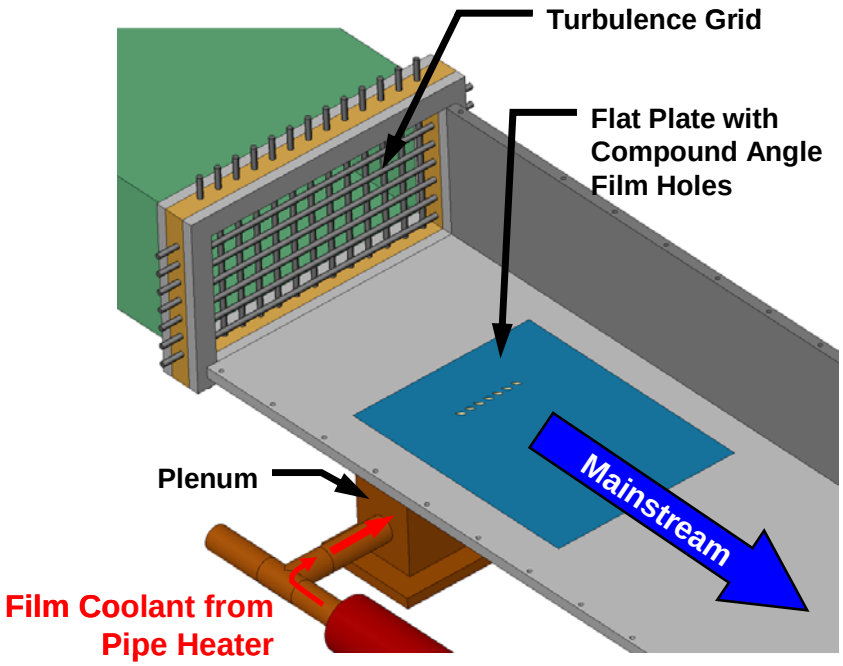


**Fig. 12 3D Model of the low speed wind tunnel and test plate**

For the coolant temperature, two T-type thermocouples are attached on the bottom of the film-cooling plate — one at the each entrance of the two outside holes. The thermocouple readings are measured by either a Fluke 2285B Data Logger or with National Instruments' LabVIEW software.

One film-cooling hole geometry is considered for this study: compound angle cylindrical holes. Figure 13 shows a detailed view of this hole geometry. The plexi-glass film-cooling plate is 304.8 mm x 228.6 mm x 15 mm. The plate consists of a single row of seven holes. The diameter of the cylindrical holes is 4 mm, and the spanwise spacing of the holes is 12 mm (3$D$). The holes have a 30º streamwise angle ($\theta$) and a 45º spanwise angle ($\beta$). The film-cooling plate is screwed onto the air plenum so that the top surface of the plate rests flush with the bottom surface of the wind tunnel. The film-cooling holes are located 21.75 cm ($x/D$ = 54.4) from the turbulence grid.

*Measured Film Cooling Effectiveness on a Flat Plate*

As previously mentioned, the scope of this investigation is to compare experimental methods rather than the optimization of a film hole configuration. As previously described, a compound angle configuration was chosen for this study. Figure 14 conceptually shows the interaction of the film coolant with the mainstream coolant on the test surface. The coolant is ejected from the film cooling holes, and as it exits the holes, the mainstream flow changes the direction of the coolant flow. As the coolant is re-directed downstream, the coolant also spreads, so the film coverage area is greater

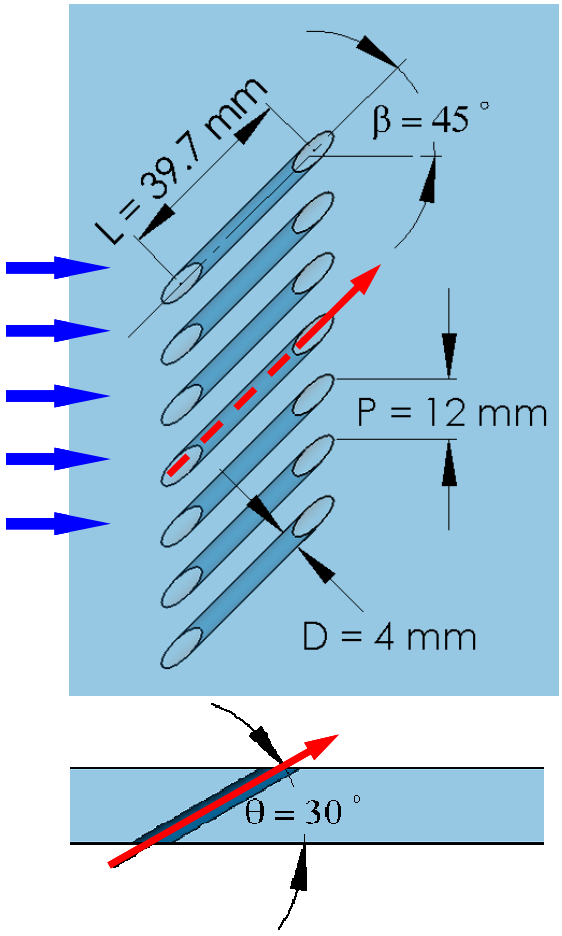


**Fig. 13 Schematic of the compound angle film cooling holes**

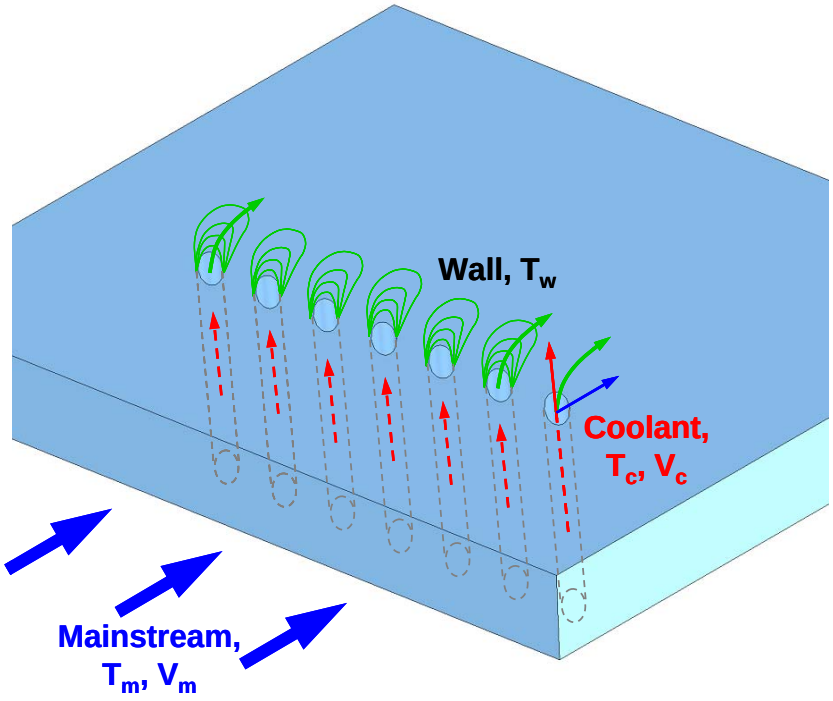


**Fig. 14 Conceptual view of coolant flow from compound angle film cooling holes**

than with simple cylindrical holes. With this general behavior in mind, the discussion will continue to the various experimental techniques.

Figures 15 and 16 show the contour plots of the effectiveness for cylindrical compound holes at the blowing ratios of $M$ = 0.4, 0.6, 1.2, and 1.8. The effectiveness distributions in Fig. 15 were measured without the turbulence grid in the wind tunnel, and the distributions shown in Fig. 16 were measured with the turbulence grid, so the mainstream flow has a turbulence intensity of approximately 6%. As shown in Fig. 15, as the blowing ratio increases, the effectiveness of the film coolant tends to cover more area downstream of the holes. The higher blowing ratios cover more distance in the downstream direction than the lower blowing ratios. For the lower blowing ratios, the mainstream pushes the coolant towards the downstream direction, which creates more uniform coverage in the lateral direction. However, the higher blowing ratios increase the coolant momentum, so the coolant flow is not so easily deflected by the mainstream. As a result, the lateral coverage of the coolant is not as uniform. Therefore, optimizing the blowing ratio involves finding a balance between uniform lateral coverage and the distance covered downstream of the holes.

The trends shown in Fig. 16 for cases with the turbulence grid are very similar to those shown in Fig. 15 without the turbulence grid. From only a comparison of the contour plots it is difficult to notice any appreciable variation due to the increased turbulence. Figure 17 shows the spanwise averaged film cooling effectiveness over five holes in both low and high turbulent flows. These plots clearly show the separation and reattachment of the jets immediately downstream of the holes. The maximum

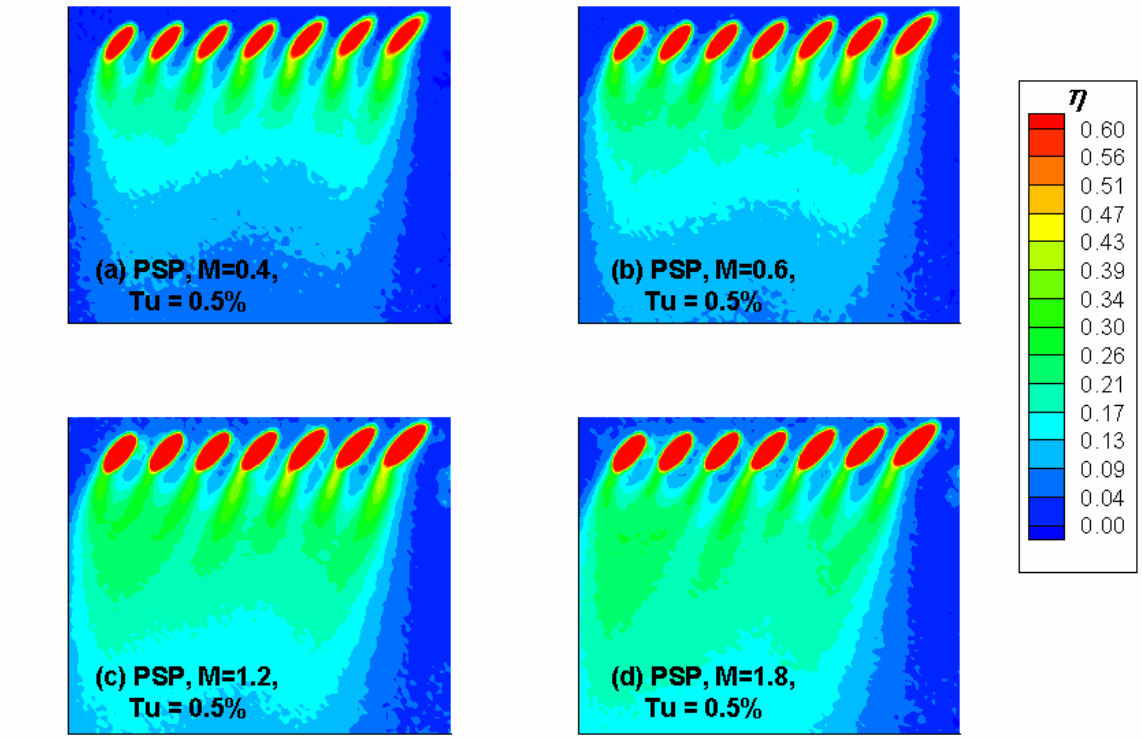


**Fig. 15 Film cooling effectiveness distributions measured using PSP with a freestream turbulence of 0.5% (75.9 mm (streamwise) x 92.4 mm (spanwise))**

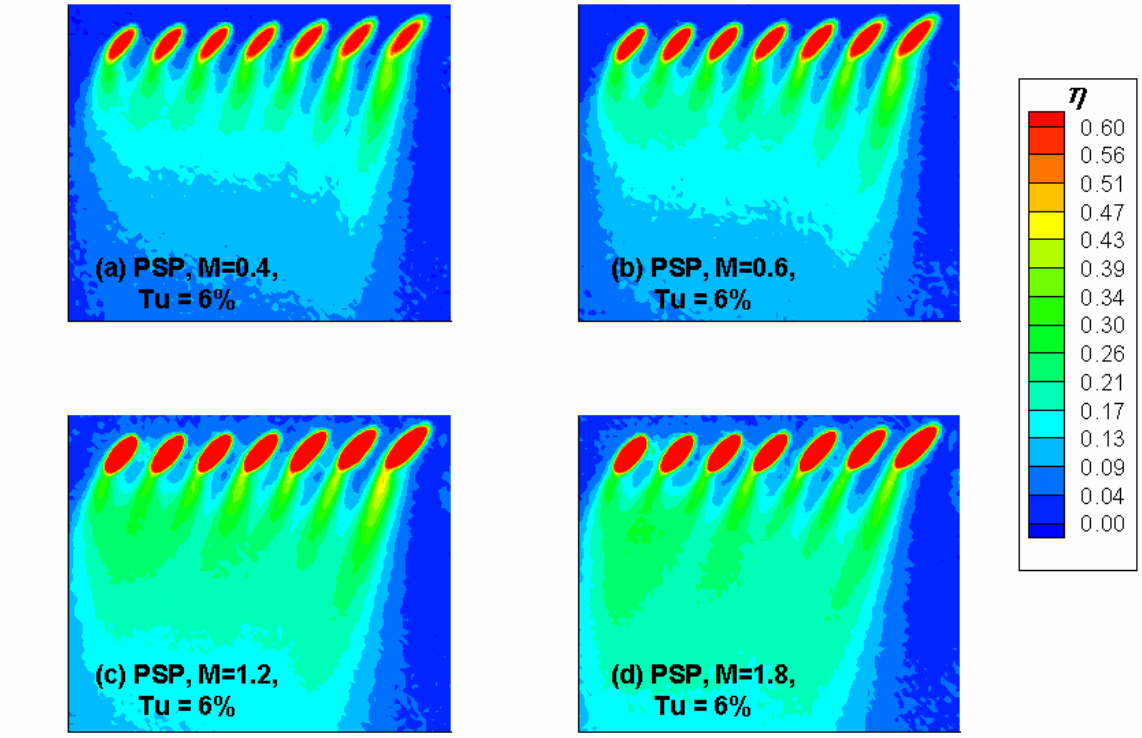


**Fig. 16 Film cooling effectiveness distributions measured using PSP with a freestream turbulence of 6% (75.9 mm (streamwise) x 92.4 mm (spanwise))**

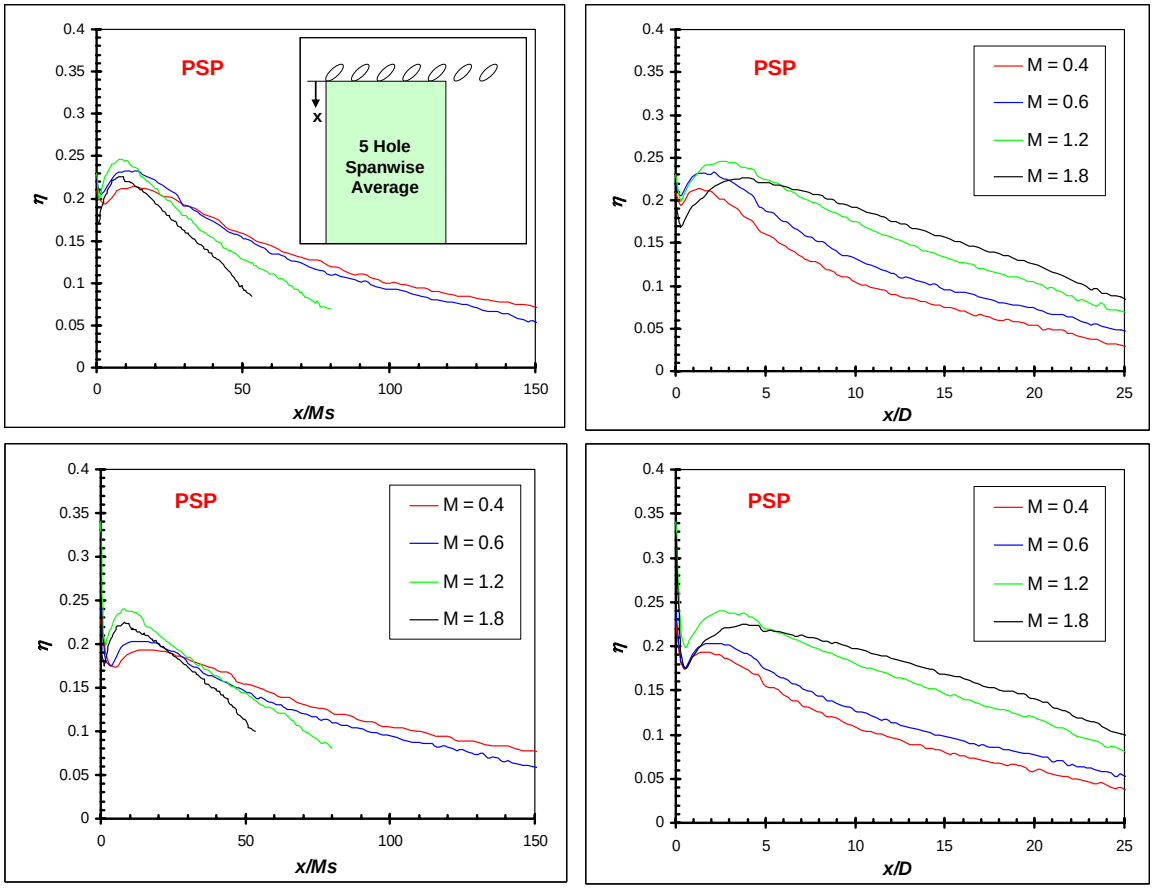


**Fig. 17 Five hole spanwise averaged film cooling effectiveness measured using PSP**

effectiveness does not occur at x = 0, as the jet has blown off the surface of the plate. The effectiveness increases to a maximum where the jet reattaches on the plate, and from that point, the film effectiveness gradually decreases. However, the effect of turbulence is not easily seen in this figure, so Fig. 18, shows a direct comparison of the freestream turbulence effect. With the selected film hole configuration, turbulence does not significantly effect the film cooling effectiveness. Near the holes, the film cooling effectiveness is generally higher in the low turbulent flow, and downstream the effect of turbulence diminishes as the low and high turbulence curves merge together.

The resolution of the PSP shows good data in the near hole region. The PSP data is not affected by the edges of the holes or sharp corners (ex. the beginning of the test plate). For effectiveness measurements, this is one strong advantage for PSP. Other methods that involve heating will have more uncertainty around these types of areas because of conduction effects and the 1-D heat transfer assumption, which is made for the transient liquid crystal measurements.

The uncertainty analysis performed on the film effectiveness measurements of the PSP was based on that described in the Kline and McClintock [70]. The uncertainty of the pressure distribution is estimated to be ± 5.9%, and the film effectiveness was estimated to be ± 9.4%. This yielded a deviation of ± 0.02 effectiveness units for the highest laterally averaged cases.

The problems associated with steady state heat transfer experiments became very obvious with the steady state TSP technique. A plenum located under the film cooling plate effectively distributes the coolant flow evenly through the discrete film holes;

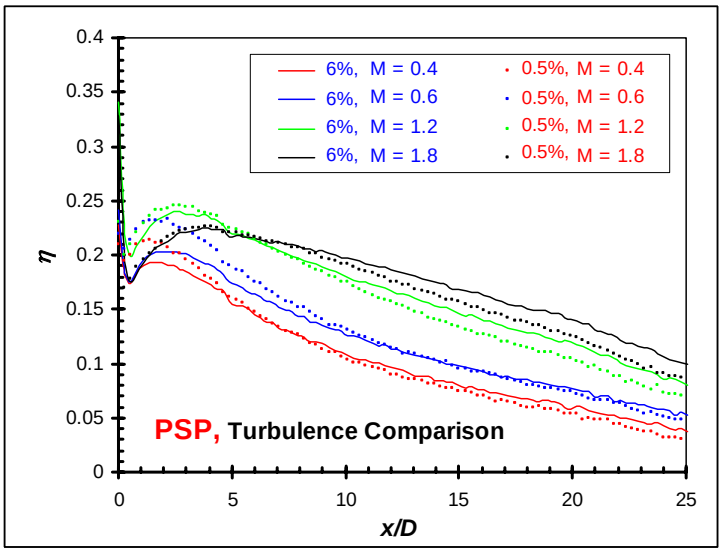


**Fig. 18 Turbulence comparison of the five hole spanwise averaged film cooling effectiveness measured using PSP**

however, with the test plate serving as the top of the plenum, a large area directly beneath the film cooling holes is directly exposed to the hot coolant. Although plexi-glass, with a relatively low thermal conductivity, is used as the test surface, it is not a perfect insulator, and actually conducts a large amount of heat from the plenum to the top surface of the test plate. This coupled with the conduction from the coolant traveling through the holes, makes it very difficult to obtain accurate film effectiveness measurements near the holes.

In an effort to demonstrate this fundamental problem with steady state heat transfer techniques, the film cooling effectiveness results are presently differently for the TSP technique than the PSP technique. Figure 19 shows four film cooling effectiveness distributions measured at four different times for a single blowing ratio ($M = 0.6$). When the hot coolant is first directed to the flat plate and through the holes, heat conduction is occurring on both sides of the flat plate: on the bottom due to the plenum and the top from the relatively warm mixture of the coolant and mainstream traveling downstream. As shown in Fig. 19(a), the resolution after only 15 seconds is very poor; the coolant temperature exiting the film cooling holes is relatively low, resulting in a small temperature difference between the coolant and mainstream temperatures. After five minutes, Fig. 19(b) shows better resolution after 5 minutes as the temperature difference between the mainstream and coolant flows increases. However, an effectiveness is obtained both upstream of the holes and between the holes. As this is physically impossible, the elevated temperature in these areas is due to the conduction through the plexi-glass plate. As time increases to 10.5 minutes and onto 30 minutes,

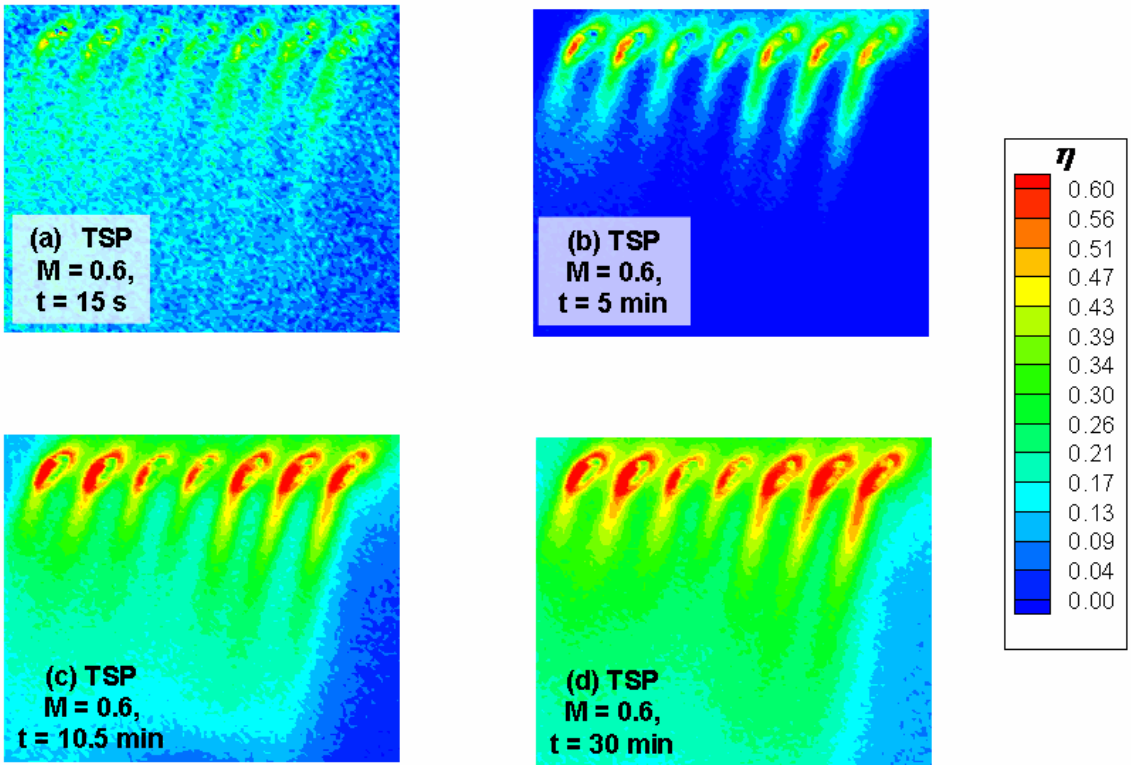


**Fig. 19 Film cooling effectiveness distributions measured using TSP with a mainstream turbulence of 6% at various times (*M* = 0.6, 77.7 mm (streamwise) x 85.0 mm (spanwise))**

the area of zero film cooling effectiveness diminishes. The image taken after 30 minutes poorly compares to the high turbulence distribution obtained with the PSP (where conduction problems do not exist).

Similar trends are shown for the blowing ratio of 1.2 in Fig. 20. Although distinct film cooling traces are seen on the test plate, the effect of conduction is seen over the entire viewing area. Figure 21 shows the how effectiveness varies with time at specific locations downstream of the holes. At each location, the effectiveness is averaged over same five hole area as previously shown. For both blowing ratios, the same trend is observed for the film cooling effectiveness; the effectiveness decreases to some minimum value, and then begins increases until the film cooling effectiveness eventually levels to what would be considered steady state. The initial decrease in effectiveness occurs as the relatively warm mixture of the mainstream and coolant is transferring heat to the top surface of the test plate, and the heat travels through the plate due to conduction. As time progresses, the effectiveness begins to rise as the conduction from the bottom of the plate (from the plenum) begins to dominate. At some time (approximately 20 minutes), the plate is in thermal equilibrium, with balanced conduction through the plate. Due to this conduction through the plate, the surface temperature of the plate is much warmer than one would expect if the conduction effects were minimized.

Based on the Kline and McClintock uncertainty analysis and the estimated uncertainty of TSP surface temperature measurement of 1°C [70], the uncertainty of the film cooling effectiveness measurements was estimated to be 9%. However, the

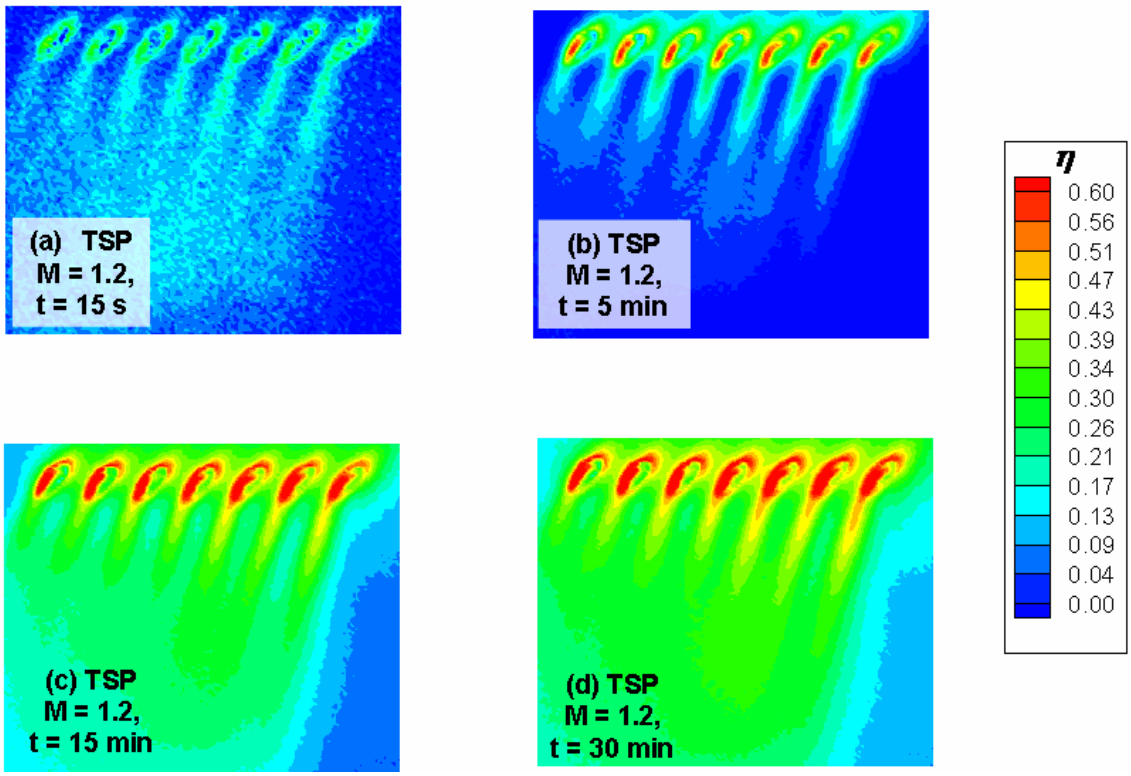


**Fig. 20 Film cooling effectiveness distributions measured using TSP with a mainstream turbulence of 6% at various times (*M* = 1.2, 77.7 mm (streamwise) x 85.0 mm (spanwise))**

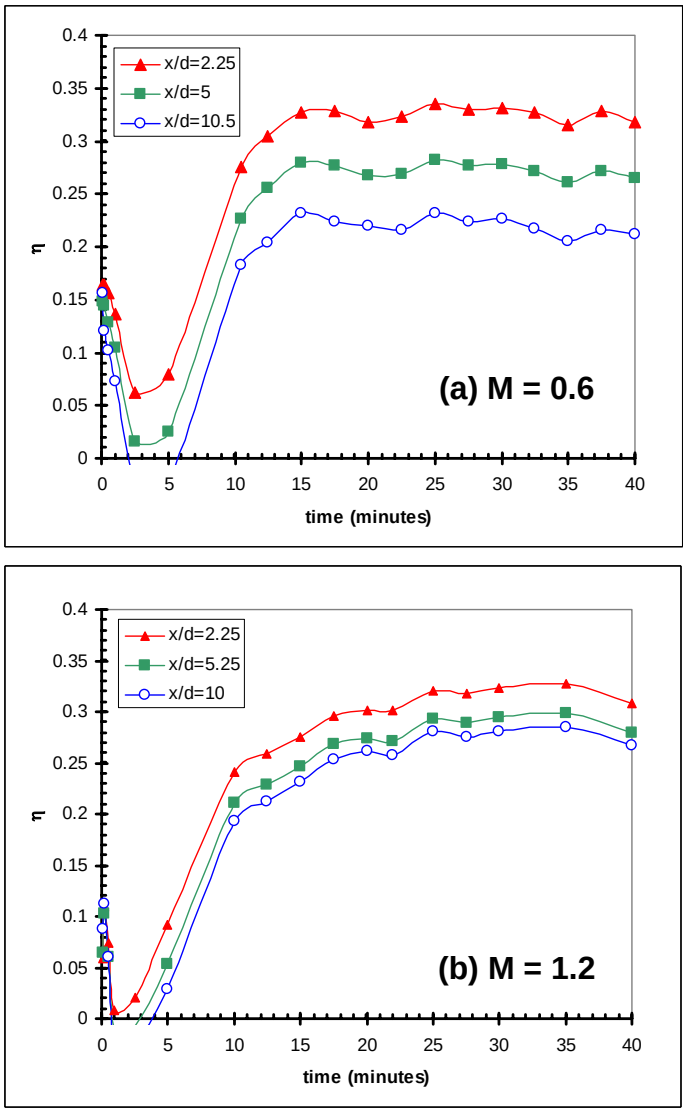


**Fig. 21 Spanwise averaged film cooling effectiveness as a function of time at specified locations measured using TSP (Tu = 6%)**

uncertainty increases as the temperature difference between the surface and mainstream decreases. At very low effectivenesses (approaching zero), the temperature difference between the surface and mainstream approaches zero, magnifying the 1°C uncertainty with the TSP temperature measurement.

Obvious problems arise with the implementation of a steady state heat transfer experiment. Not only is the accuracy near the holes compromised, but the area downstream of the holes is also affected by conduction through the plexi-glass plate. Although temperature sensitive paint was successfully used to measure the surface temperature of the test plate, problems with the nature of the experiment compromise the validity of the film effectiveness results. When compared with the results obtained using PSP, the PSP technique is far superior for the measurement of the film cooling effectiveness.

The final method considered is the steady state IR method. Because this is a heat transfer technique the same problems that arose with the TSP are prevalent with the IR technique. As the detailed effectiveness plots show for both the low (Fig. 22) and high freestream turbulence (Fig. 23) cases, conduction between and upstream of the holes is a problem. The comparison between the high and low freestream turbulence cases reveals only minimal differences, as Fig. 24 shows. Each blowing ratio in the steady state IR experiments was run for approximately 30 minutes, with a coolant temperature maintained at approximately 110°F (43.33°C). Lowering the coolant temperature is likely to decrease the conduction through the plate, but that also decreases

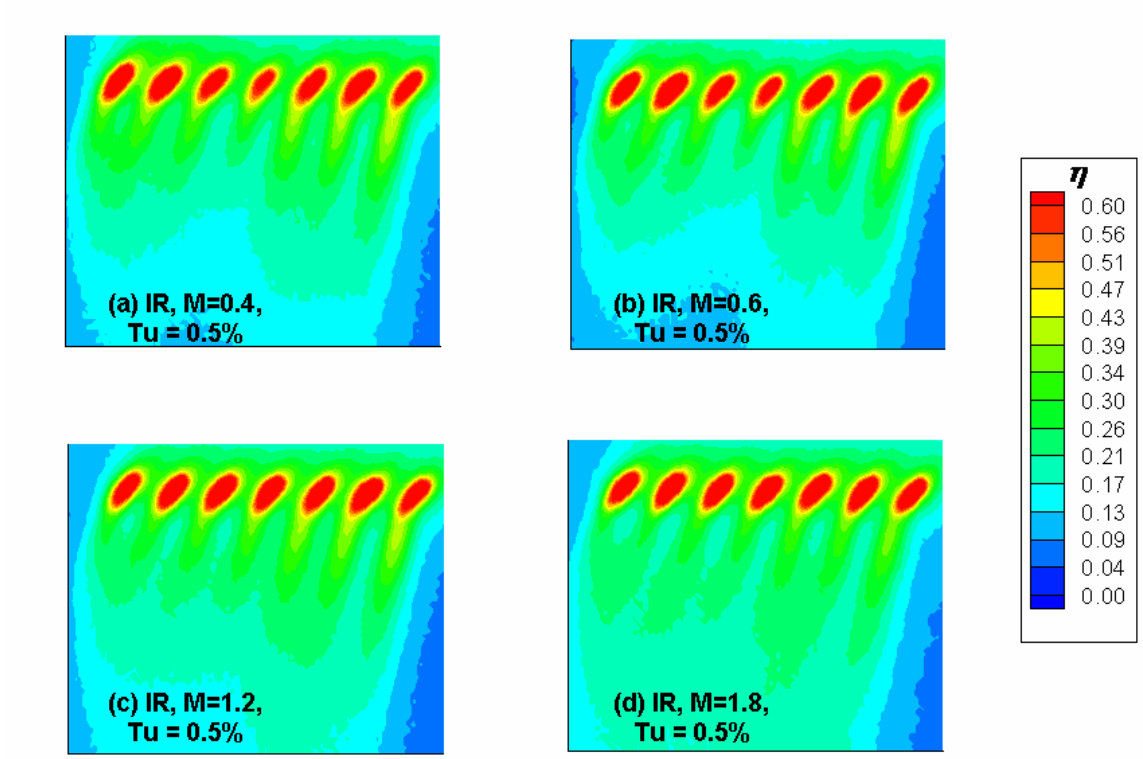


**Fig. 22 Film cooling effectiveness distributions measured using IR thermography with a freestream turbulence of 0.5% (71.4 mm (streamwise) x 86.6 mm (spanwise))**

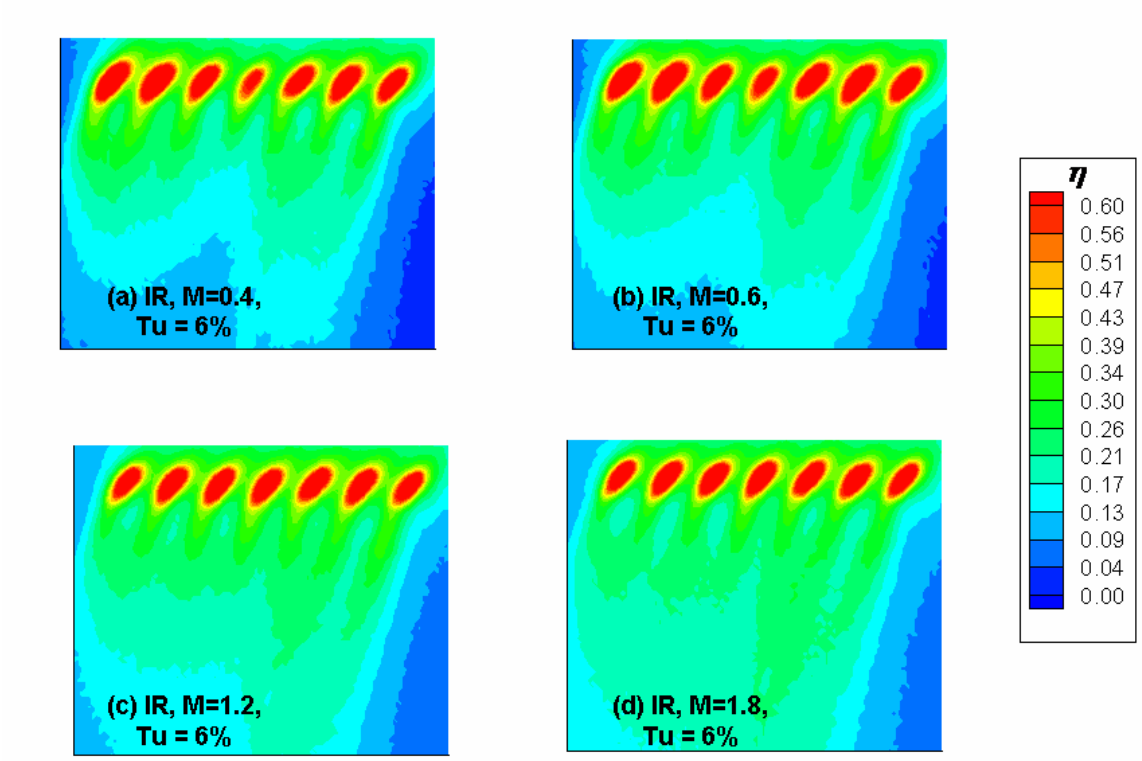


**Fig. 23 Film cooling effectiveness distributions measured using IR thermography with a freestream turbulence of 6% (71.4 mm (streamwise) x 86.6 mm (spanwise))**

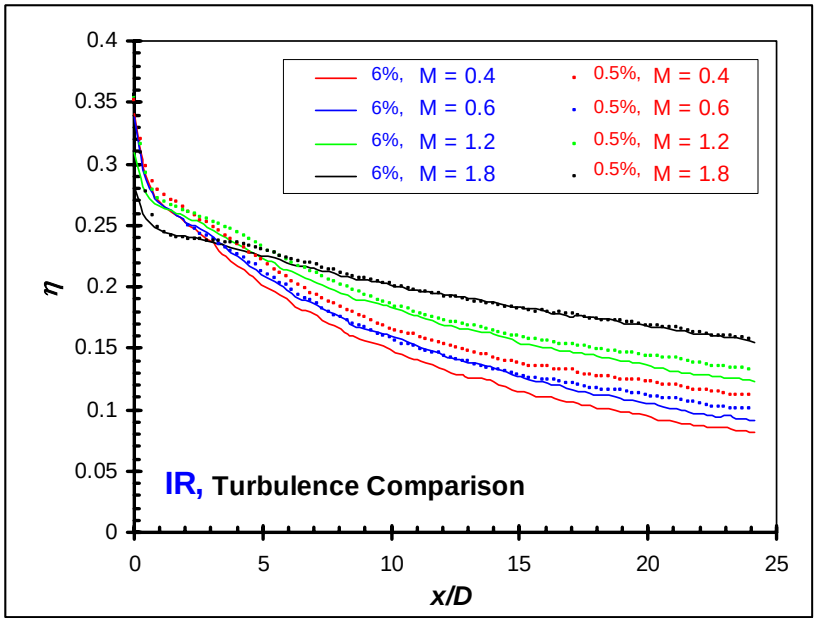


**Fig. 24 Turbulence comparison of the five hole spanwise averaged film cooling effectiveness measured using IR thermography**

the temperature difference used to calculate the film cooling effectiveness, which increases the uncertainty of the measurements.

Figure 24 not only compares the effectiveness in low and high freestream turbulence, it also shows the conduction near the holes. As Fig. 17 showed with the PSP results, the maximum effectiveness occurs downstream of the holes where the jet reattaches to the surface. However, the steady state IR technique shows the maximum effectiveness occurs at x = 0. This is misleading as the elevated effectiveness reading comes from the elevated surface temperature due to heat conduction between the holes.

The uncertainty of the infrared thermography was calculated by the procedure discussed in Kline and McClintock [70]. The uncertainties of the mainstream ($T_m$) and coolant ($T_c$) temperatures were each ± 0.2ºC, and the uncertainty of the surface temperature ($T_w$) was ± 0.1ºC. The average uncertainty of the effectiveness ($\eta$) was estimated at ± 8.8%. Therefore, the accuracy of the measurements was within ± 0.02 effectiveness units for the worst case.

Clearly the steady state IR technique suffers from the same problems as the steady state TSP technique. Although both TSP and IR techniques can be applied over a wide range of temperatures, for the TSP method, the surface must be coated with the temperature sensitive paint. This makes IR more desirable; if an in situ calibration is used, the surface of the test plate does not have to be altered. However, if one chooses, the surface can be painted black to increase the emissivity of the surface.

Figure 25 shows the spanwise average film cooling effectiveness plotted for the three methods considered in this study; the effectiveness obtained at various times with

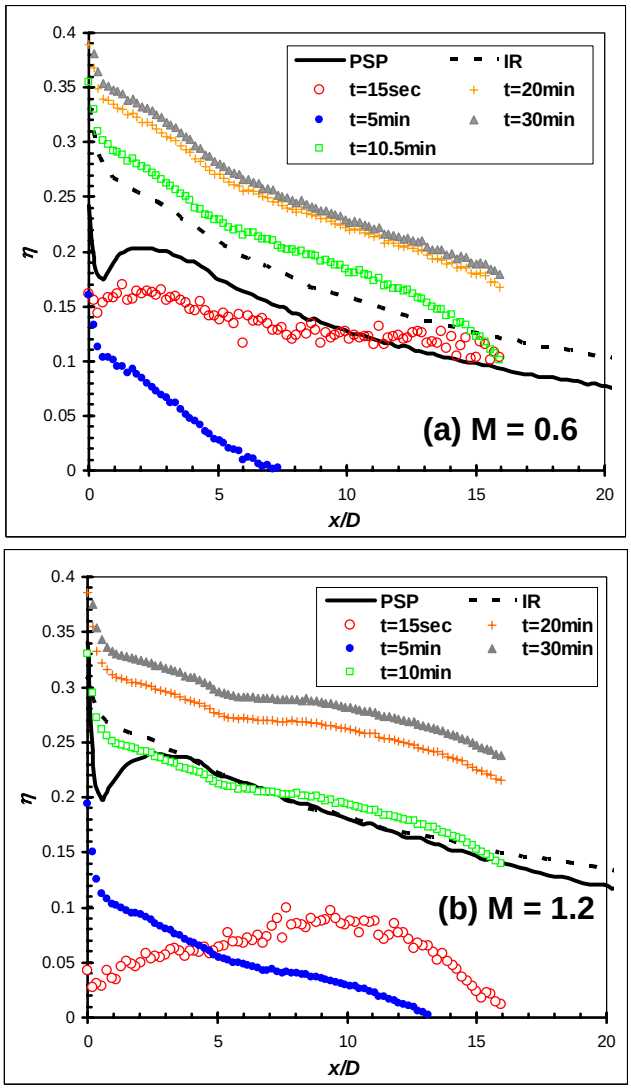


**Fig. 25 Five hole spanwise averaged film cooling effectiveness comparison for the steady state measurement techniques (Tu = 6%)**

the TSP is also shown for comparison. The results shown in this figure represent the high freestream turbulence for all cases. Beginning with Fig. 25(a) with $M = 0.6$, it is clear the results obtained from the IR camera are greater than those obtained with the PSP. The difference is amplified near the holes, and far downstream, the difference between the two curves remains constant. For the TSP method, the curve corresponding to 10 minutes most closely matches the IR data. However, one would expect the curve for 30 minutes to correspond to the steady state IR data. The difference in coolant temperatures of these two experiments could account for the different film cooling effectivenesses. Conduction through the plexi-glass plate is dominated by the coolant temperature; if the coolant temperature is excessively high, more heat is transferred through the plate due to conduction, and the measured wall temperature is artificially high.

If only Fig. 25(b) was presented, it would appear the 3 experimental methods considered are in excellent agreement. However, that would be very misleading. After the coolant reattaches to the surface, the IR and PSP techniques show good agreement in the measured film cooling effectiveness, until they begin to diverge very far downstream. Also in good agreement with these two curves is the effectiveness measured by the TSP at 10 minutes. However, as shown in Fig. 21, steady state has not been achieved after only 10 minutes. If TSP at a greater time (20 or 30 minutes) is compared to the PSP and IR data, the effectiveness measured by the TSP is much higher.

Pressure sensitive paint is the superior steady state method for measuring the film cooling effectiveness. Because PSP relies on the mass transfer rather than heat transfer,

inherent problems associated with heat transfer methods are avoided. Detailed distributions can be obtained in the critical area around the holes, and the true jet separation and reattachment behavior is captured with the PSP.

# FILM COOLING EFFECTIVENESS ON A TURBINE BLADE PLATFORM

### *Low Speed Wind Tunnel with Five Blade Linear Cascade*

The low speed wind tunnel facility used to study the platform film cooling effectiveness, is shown in Fig. 26. Modifications were made to the endwall of the wind tunnel that was previously used by Zhang and Han [71]. The open-loop wind tunnel operates in suction with two mesh screens located at the inlet of the wind tunnel. To produce uniform flow entering the cascade, a 4.5:1 contraction nozzle guides the flow to the linear cascade. The test area is 25.4 cm high by 75.0 cm wide, and has a 107.49° turning angle to match the turning of the five-blade cascade. Head- and tailboards were added to the leading and trailing edges of the inner and outer airfoils to further guide the flow into the cascade. The cascade inlet velocity was maintained at 20 m/s and was set using a variable frequency controller attached to the 15 hp (11.2 kW) blower. The inlet velocity was measured (and continuously monitored) using a pitot tube placed inside the wind tunnel. The mainstream accelerates through the cascade, so the mainstream velocity at the cascade exit is 50 m/s.

The freestream turbulence through the cascade was varied by placing a turbulence grid 30 cm upstream of the cascade. The grid is made of square bars that are 1.3 cm wide, and they are spaced 4.8 cm in both the horizontal and vertical directions. Zhang and Han [71] used hot wire anemometry and showed the inlet turbulence intensity increases from 0.75% (without the grid) to 13.4% with a length scale of 1.4 cm. The

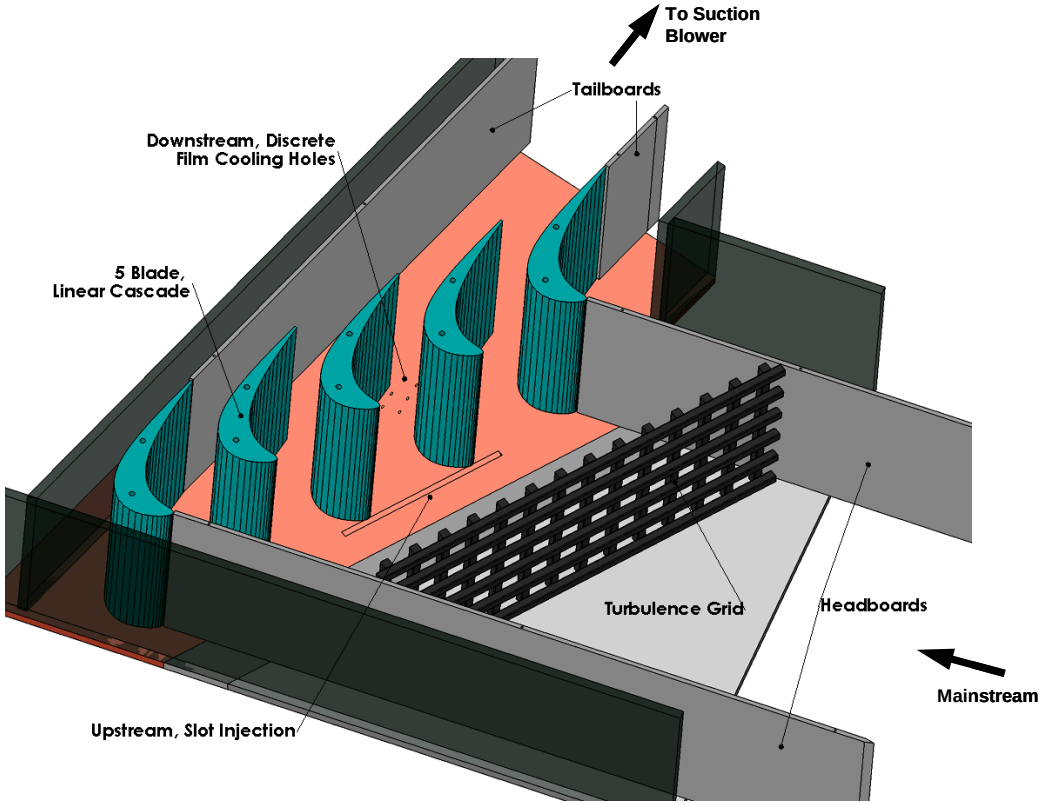


**Fig. 26 Overview of the low speed wind tunnel used to study platform cooling**

turbulence intensity decreases with the flow acceleration through the passage to a level of 5% at the cascade exit.

Figure 27 shows the typical, advanced, high pressure turbine blade used for this study. The blade, which was scaled up five times, has a 107.49° turning angle with an inlet flow angle of 35° and an outlet flow angle of -72.49°. The chord length of the blade is 22.68 cm and the height of the blade is 25.4 cm. The blade-to-blade spacing at the inlet is 17.01 cm with a throat-to-span ratio of 0.2. The mainstream flow accelerates from 20 m/s at the inlet to 50 m/s at the outlet of the cascade. The inlet flow periodicity and uniformity for the blade design has been measured and reported by Zhang and Han [71]. In addition, the velocity (pressure) distributions along the pressure and suction surfaces of the blades have also been measured. With the turbulence grid placed in the wind tunnel, the freestream turbulence ranges from 13.4% at the cascade inlet to 5% at the outlet of the cascade, as measured using a hot wire anemometer [71]. The mainstream Reynolds number (based on the inlet velocity and blade chord) is $3.1*10^5$.

***Cooled Platform with Inclined Slot and Streamline Film Cooling Holes***

To study the film cooling effectiveness on the blade platform, the original smooth platform was altered to include both upstream slot injection and downstream discrete film cooling holes. The upstream slot, shown in Fig. 28, covers 1.5 passages. The width of the slot is 0.44 cm wide and is at a 30° angle to the mainstream flow. The length of the slot is 2.54 cm, so the length-to-width ratio ($l_s/w$) is 5.7. The downstream edge of the slot is aligned with the leading edge of the cascade. Considering the angled,

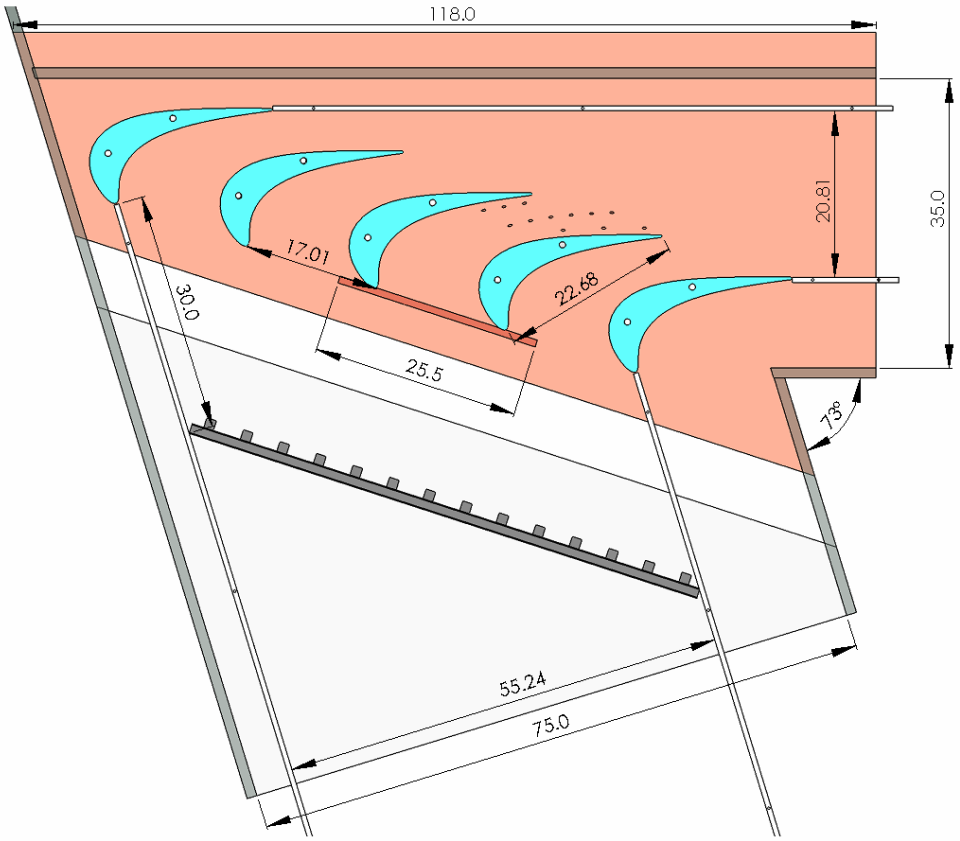


**Fig. 27 Low speed wind tunnel and turbine blade details**

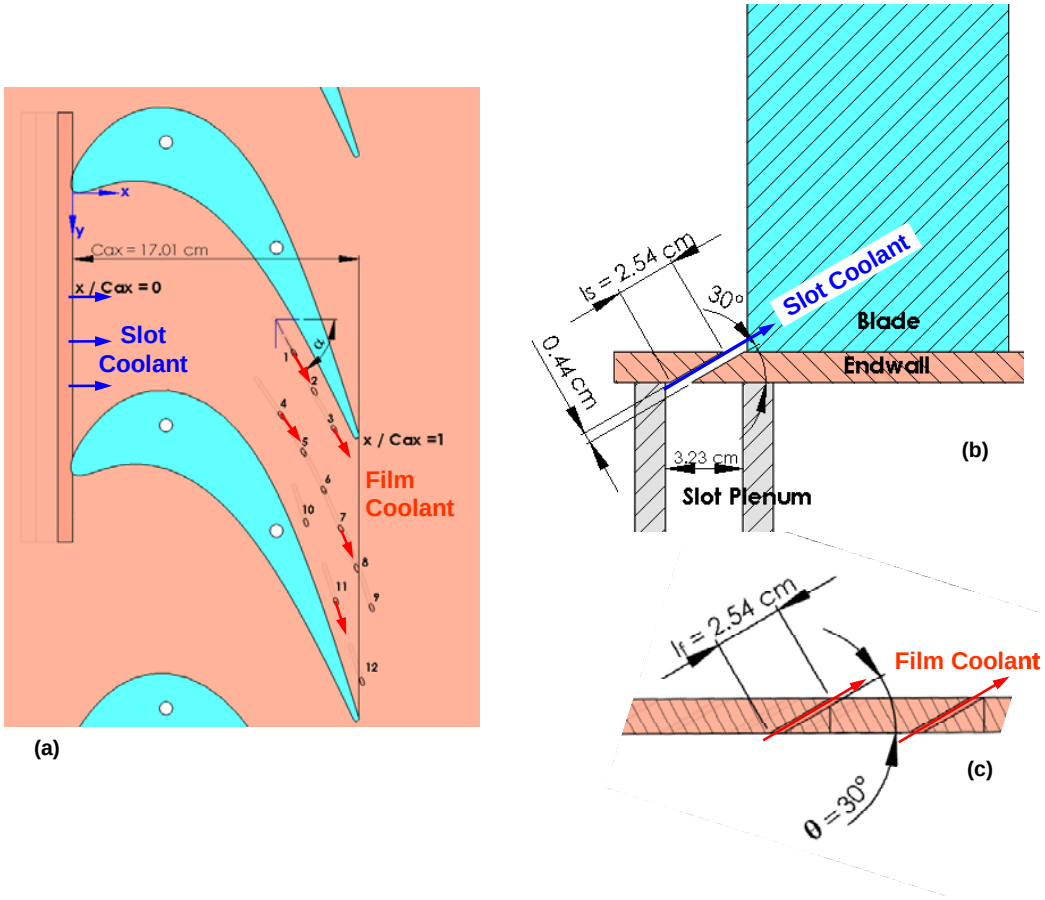


**Fig. 28 Platform film cooling configurations. (a) Detailed view of cooled passage, (b) Upstream slot injection details, and (c) Cross-sectional view of 2 discrete film holes**

downstream half of the slot as part of the blade platform, this geometry allows for a fundamental study of the coolant flow from the stator-rotor gap. Because the seal geometry was not taken from a specific engine, actual designs may consist of a longer slot length, so the platform extends further upstream of the blade leading edge. Coolant (air or nitrogen) is metered through a square edge, ASME orifice flow meter and piped to a plenum located directly beneath the slot. The plenum is sufficiently large enough to ensure the coolant is uniformly distributed at the exit of the slot. The flow rate of the slot coolant can be varied, so the film cooling effectiveness can be measured over a range of flow rates varying from 0.5% to 2.0% of the mainstream flow.

With the slot expected to provide adequate film coverage over the upstream half of the passage, discrete film cooling holes are only used on the downstream half of the passage. As shown in Fig. 28, the 12 film cooling holes are positioned to approximately follow the blade profile. The holes have a diameter of 0.25 cm, a streamwise angle, $\theta$, of 30° (as with the slot), and the lateral (compound) angle varies to match the blade profile. With a hole length of 2.54 cm, the length-to-diameter ratio (l/d) is 10. Table 1 shows the relative location and angle of the film cooling holes. The coolant (air or nitrogen) is supplied to the film cooling holes via a second plenum located directly beneath the film cooling holes. The coolant flow rate is measured using a volumetric flow meter, and the flow is varied to achieve average blowing ratios varying from 0.5 to 2.0 (based on the velocity of the mainstream at the exit of the cascade).

**Table 1 Discrete film hole location and orientation**

| Film Hole Number | x (cm) | y (cm) | d (cm) | $\alpha$ | $\theta$ |
|---|---|---|---|---|---|
| **1** | 13.3 | 9.8 | 0.25 | 61° | 30° |
| **2** | 14.5 | 12.1 | 0.25 | 61° | 30° |
| **3** | 15.7 | 14.4 | 0.25 | 61° | 30° |
| **4** | 12.6 | 13.5 | 0.25 | 55.5° | 30° |
| **5** | 13.9 | 15.8 | 0.25 | 61° | 30° |
| **6** | 15.1 | 18.0 | 0.25 | 64° | 30° |
| **7** | 16.1 | 20.4 | 0.25 | 67° | 30° |
| **8** | 17.1 | 22.7 | 0.25 | 72° | 30° |
| **9** | 18.0 | 25.1 | 0.25 | 72° | 30° |
| **10** | 14.0 | 20.0 | 0.25 | 72° | 30° |
| **11** | 15.9 | 24.7 | 0.25 | 72° | 30° |
| **12** | 17.4 | 29.6 | 0.25 | 72° | 30° |

The presentation of the results begins with the film cooling effectiveness obtained on the passage endwall with slot injection upstream of the cascade. This includes experimental results obtained over a wide range of slot flow rates. The effect of turbulence on this film cooling effectiveness is also experimentally considered. This discussion is followed by the presentation of the film cooling effectiveness measured downstream with coolant only from the downstream discrete holes, including the effects of various blowing ratios and turbulence intensities. The detailed film cooling effectiveness is then obtained for upstream slot injection combined with downstream discrete film cooling. After comparing the detailed film effectiveness distributions for all of these cases, final comparisons will be made using the spanwise averages of the film cooling effectiveness. Table 2 shows a summary of the 24 experimental cases considered. The slot injection rate is commonly considered as a percentage of the mainstream. However, the blowing ratio (velocity ratio, as coolant and mainstream densities are equal) is also presented as a reference. The slot blowing ratio is based on the mainstream velocity at the inlet of the cascade (20 m/s). The blowing ratio for the downstream film holes is also shown, but because the film cooling holes are located on the downstream half of the passage, the blowing ratio for the discrete holes is based on the exit velocity of the mainstream flow (50 m/s).

The detailed film cooling effectiveness was obtained on a single passage with various slot injection rates. Figure 29 shows the detailed effectiveness distribution on the platform with a freestream turbulence intensity of 0.75%. The effect of the blowing ratio is clearly seen comparing figures 29(a) – 29(d). At the lowest flowrate of 0.5%, the

**Table 2 Experimental conditions considered for the inclined slot**

***Upstream Inclined Slot Injection***

| Slot Injection Rate ($m_s$) | $M_s$ | $I_s$ | DR | Tu |
|---|---|---|---|---|
| **0.5%** | 0.29 | 0.084 | 1.0 | 0.75%, 13.4% |
| **1.0%** | 0.57 | 0.325 | 1.0 | 0.75%, 13.4% |
| **1.5%** | 0.86 | 0.740 | 1.0 | 0.75%, 13.4% |
| **2.0%** | 1.14 | 1.30 | 1.0 | 0.75%, 13.4% |

***Downstream Discrete Film Holes***

| $M_f$ | $I_f$ | DR | Tu |
|---|---|---|---|
| **0.5** | 0.25 | 1.0 | 0.75%, 13.4% |
| **1.0** | 1.00 | 1.0 | 0.75%, 13.4% |
| **1.5** | 2.25 | 1.0 | 0.75%, 13.4% |
| **2.0** | 4.00 | 1.0 | 0.75%, 13.4% |

***Combined Upstream Slot and Downstream Film***

| Slot Injection Rate ($m_s$) | $M_s$ | $M_f$ | $MFR_{total}$ | Tu |
|---|---|---|---|---|
| **1.0%** | 0.57 | 0.5 | 1.11% | 0.75% |
| **1.0%** | 0.57 | 1.0 | 1.22% | 0.75% |
| **1.0%** | 0.57 | 1.5 | 1.34% | 0.75% |
| **1.0%** | 0.57 | 2.0 | 1.46% | 0.75% |
| **2.0%** | 1.14 | 0.5 | 2.11% | 0.75% |
| **2.0%** | 1.14 | 1.0 | 2.22% | 0.75% |
| **2.0%** | 1.14 | 1.5 | 2.34% | 0.75% |
| **2.0%** | 1.14 | 2.0 | 2.46% | 0.75% |

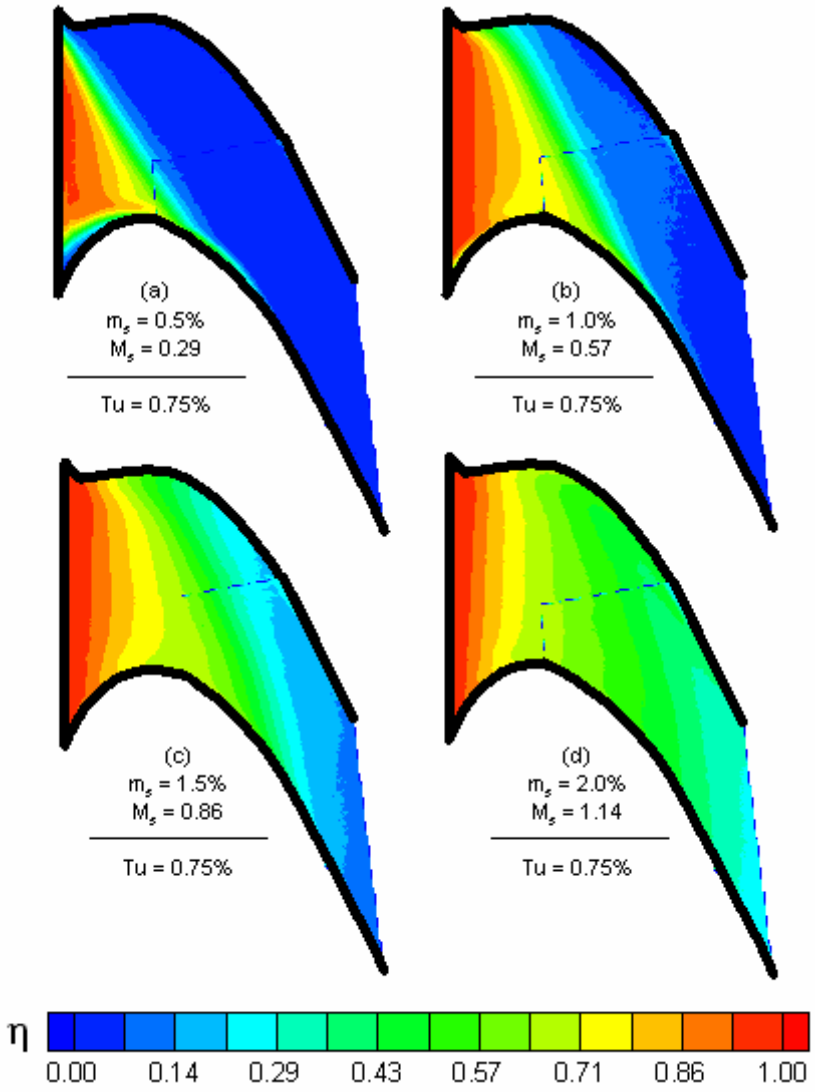


**Fig. 29 Measured film cooling effectiveness with various slot injection rates (Tu = 0.75%)**

coolant ejection does not cover the entire slot. The coolant is quickly swept from the pressure side of the passage to the suction side. Although the effectiveness approaches the ideal value of unity at the exit of the slot, the effectiveness quickly diminishes, and a large area of the passage is left unprotected. This non-uniform flow and distribution of the coolant on the platform was also observed on the endwall of multiple vane studies [23, 27, and 29]. If the injection rate is increased to 1%, the flow from the slot is more uniform. However, the general trend for the effectiveness is the same as with 0.5%: the coolant is carried from the pressure side of the passage to the suction side. The area of protection extends further downstream; however, the downstream half of the passage still does not receive adequate protection. Increasing the injection rate to 1.5% results in more uniform film coverage on the upstream half of the passage. The area of coverage increases, but coverage remains inadequate near the trailing edge of the pressure side. At the maximum flowrate of 2.0%, the effectiveness bands are more uniformly distributed through the entire passage, with the entire passage receiving protection. Zhang and Jaiswal [27] showed similar results for slot injection upstream of a vane. They concluded that at low injection rates (0.5% to 1.5%), the coolant did not reach the pressure side of the passage, and the effectiveness quickly diminished downstream of the slot. However, at high injection rates (2% to 3%), uniform film coverage was measured in the downstream half of the passage with the coverage extending to the trailing edge of the passage [27].

It was noted in previous studies upstream slot injection is an effective tool for weakening the passage vortex. The finding is observed in the present results. At the

highest injection rate of 2.0%, the effectiveness distribution is much more uniform than at the lower injection rates of 0.5% and 1.0%. The high momentum coolant disrupts the secondary flow behavior including the horseshoe and passage vortices. However, with the lower momentum coolant flows, the coolant flow is greatly affected by the passage secondary flows.

With an understanding of secondary flow on the passage endwall, the effect of an additional complexity on the film cooling effectiveness can be considered. With a turbulence grid added upstream of the cascade, the freestream turbulence intensity at the cascade inlet is raised to 13.4% [71]. Comparing the effectiveness distributions in Fig. 30 with those for the freestream turbulence level of 0.75% in Fig. 29, the general trends are the same: increasing the injection rate increases the coverage area and the uniformity of the coverage. For the lowest injection rate of 0.5%, the coverage area extends further downstream with the increased turbulence; although the coverage area increases, the majority of the passage remains unprotected. A significant increase is observed in the protection are with the injection rates of 1.0% and 1.5%. In addition, at 1.5% the shape of the effectiveness contours changes from the low freestream turbulence case. The contours are more uniform across the passage. At 2.0% the uniformity of the effectiveness continues to increase. The passage vortex is weakened with the increased freestream turbulence. The mitigated secondary flow results in better coverage of the slot coolant.

Figure 31 compares the film cooling effectiveness obtained from discrete film holes on the downstream half of the passage with turbulence intensities of 0.75% and

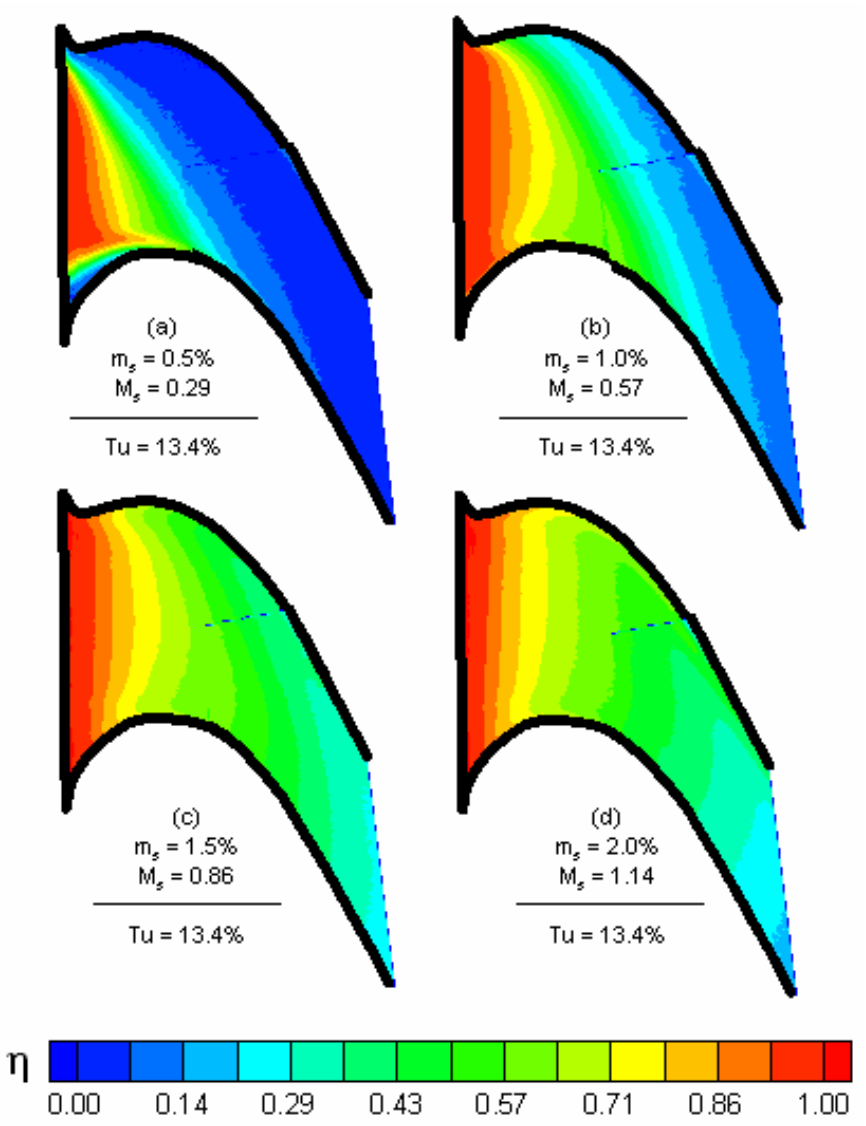


**Fig. 30 Measured film cooling effectiveness with various slot injection rates (Tu = 13.4%)**

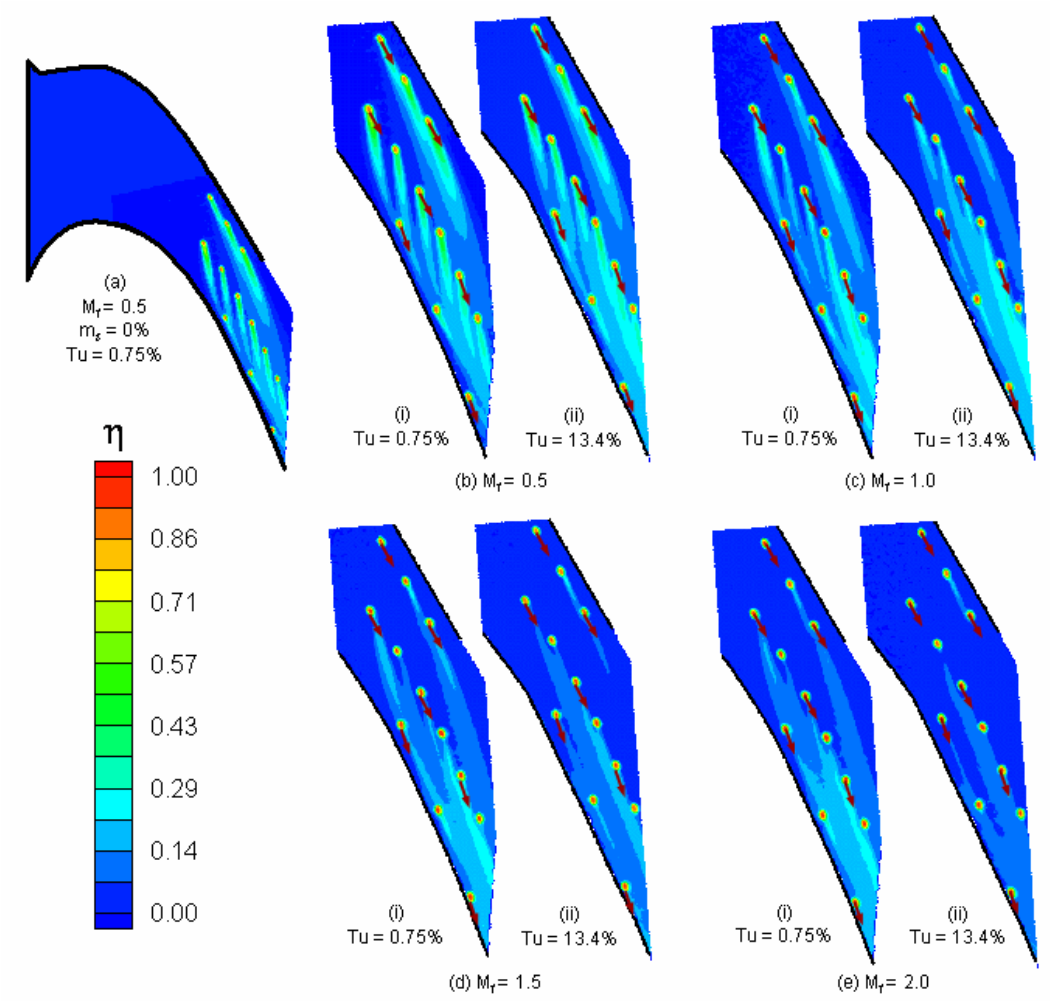


**Fig. 31 Measured film cooling effectiveness with downstream discrete film cooling**

13.4% (measured at the cascade inlet), respectively. The average blowing ratio varies from 0.5 to 2.0 based on the mainstream velocity at the cascade exit. As shown in this figure, increasing the blowing ratio decreases the film cooling effectiveness. At the lowest blowing ratio of 0.5, very distinct film traces are seen from each of the 12 film cooling holes. Increasing the blowing ratio increases the momentum of the jets exiting the holes, the jets blow off the endwall, and the coolant is carried away with the mainstream flow. From flat plate film cooling studies, it is accepted that the optimum blowing ratio occurs between 0.5 and 1.0; increasing the blowing ratio beyond 1.0 for cylindrical holes results in decreased film cooling effectiveness because the coolant does not remain attached to the surface. The strong secondary flow behavior is very clear in Fig.31(b-i); arrows added to the figure indicate the compound angle of the film cooling hole, designed to follow the blade profile. Regarding the three holes along the pressure side of the passage, the coolant traces follow the discharge angle of the holes. Near the trailing edge of the blades, the passage vortex as already crossed the passage from the pressure side to the suction side of the passage. Therefore, the coolant from these pressure side holes does not significantly deviate from their injection angles. The migration of the passage vortex is clearer with the middle row of film cooling holes. The film traces are altered significantly from the flow direction, and the coolant is pushed to the suction side of the passage. The coolant from the suction side holes covers less area than the other holes. The passage vortex has continued to gain strength, and as shown previously with the upstream slot, the coolant along the suction surface tends to

lift off the endwall and attach to the suction surface of the blade due to the growing passage vortex.

The effect of increased turbulence intensity is opposite of the effect observed for the upstream injection. Figure 31 also shows the measured film effectiveness with the turbulence grid in the wind tunnel. The turbulence intensity at the inlet of the cascade is 13.4%, but as the mainstream continues through the passage, the turbulence intensity drops, and near the exit of the cascade, the turbulence intensity is approximately 5% [71]. The effect of blowing ratio with the increased freestream turbulence is the same as the previous case: the blowing ratio of 0.5 offers the best film cooling coverage. However, increasing the freestream turbulence decrease the film effectiveness for all for blowing ratios. At $M_f$ = 1.0, the peak effectiveness clearly drops, but the increased turbulence causes the jet to spread, and more area is covered between the holes. At the highest blowing ratio of 2.0, the discrete holes provide coverage for a very small area, and the majority of the area is left unprotected. It is also seen in Fig. 31(b-ii) that the traces from the middle row of jets merge together as the increased turbulence spreads the cooling jets.

The detailed film cooling effectiveness is measured on the endwall with upstream slot injection combined with discrete film cooling downstream for a freestream turbulence intensity of 0.75%. Figure 32 shows the film cooling effectiveness distribution on the platform with a slot injection rate of 1.0% and various blowing ratios for the downstream film cooling holes. From Fig. 29(b) a large area of the endwall was left uncooled where the slot coolant did not cover. The discrete film cooling holes

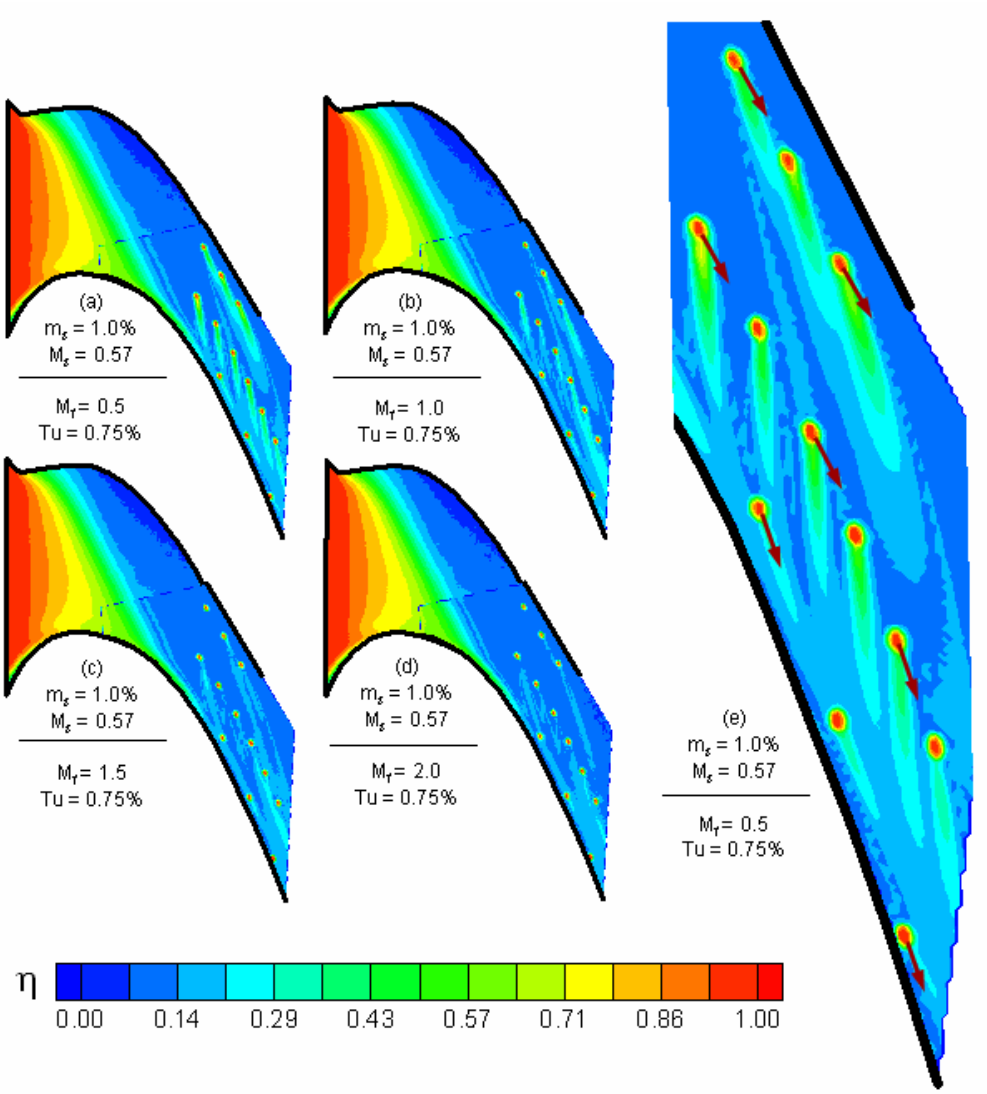


**Fig. 32 Measured film cooling effectiveness with combined slot cooling (1%) and downstream film cooling (Tu = 0.75%)**

obviously increased the effectiveness in the region near the holes, but a large area along the pressure side of the channel remains unprotected. The trends observed in this figure are the same those observed in Fig. 29(a) and Fig. 31. Because the slot coolant is quickly carried to the suction side of the passage, there is no interaction between the slot coolant and the coolant from the film holes.

Increasing the slot injection rate to 2.0% yields protection throughout the entire passage. Now with the addition of downstream film cooling holes, the two coolants will interact. At the lowest film blowing ratio of 0.5, the peak effectiveness near the film holes is very high, as shown in Fig. 33. The peak effectiveness can be as high as 0.81 immediately down stream of the first hole in the middle row. However, when there was not upstream slot injection, the corresponding effectiveness was only 0.67 (an increase of approximately 21%). The increased effectiveness is due to the film accumulation between the slot and film coolants. This effect is less obvious with the other film blowing ratios, as the jets tend to lift off the surface. Although the peak effectiveness is not as significantly affected at the increased blowing ratios, the effectiveness on the downstream half of the passage does increase when compared to the measured effectiveness with only upstream injection. When the downstream film holes are combined with the upstream slot injection, the film coolant begins to cumulate. In addition, without the upstream slot injection, the high momentum downstream coolant readily blows off the surface (Fig. 31). However, with the upstream injection, even the high momentum does not lift off as readily, as it is deflected by the slot coolant and remains attached to the passage endwall.

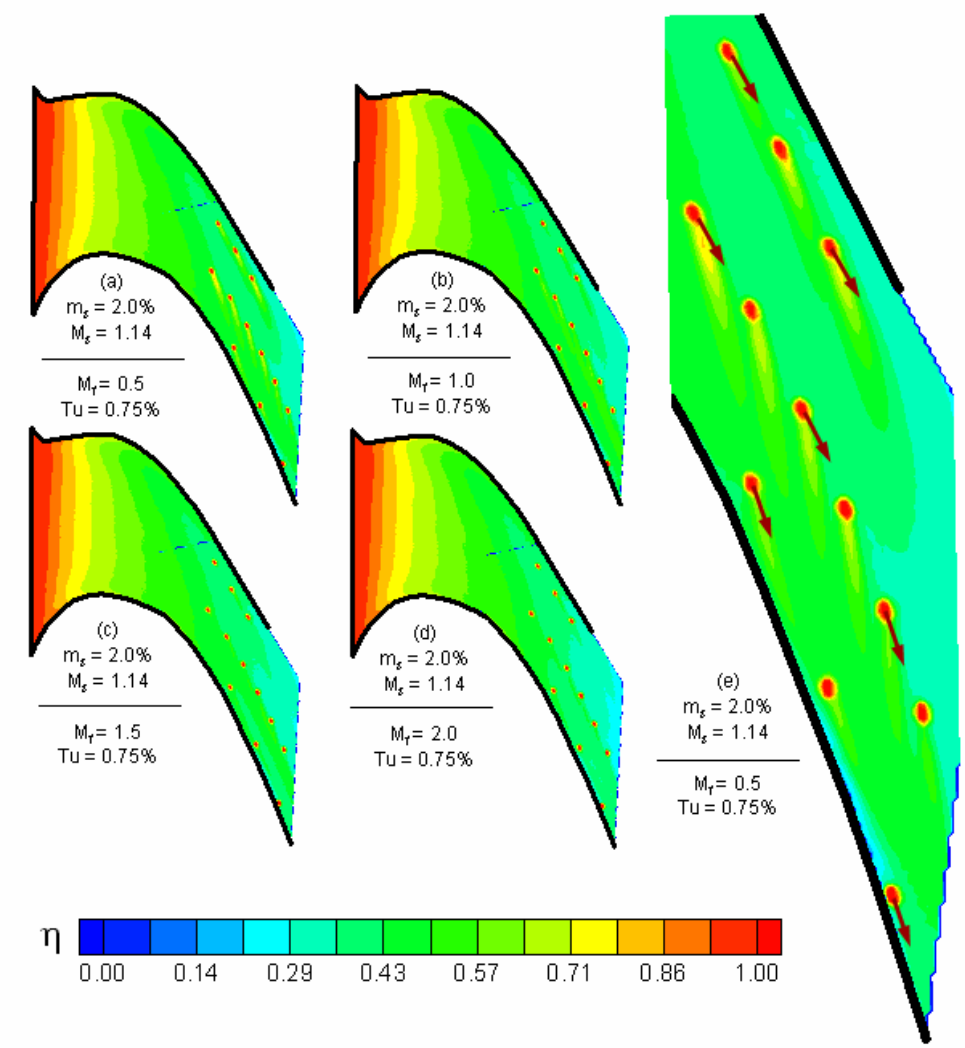


**Fig. 33 Measured film cooling effectiveness with combined slot cooling (2%) and downstream film cooling (Tu = 0.75%)**

Although valuable insight can be obtained from the detailed distributions, many times spanwise averaged plots offer additional insight and provide clear comparisons for large amounts of data. Figures 34 – 37 make such comparisons of the cases previously discussed. The effectiveness is averaged from the suction side to the pressure side of the passage in the x-direction, as shown in Fig. 28(a). The effect of the freestream turbulence and injection rate on the effectiveness from the upstream slot injection can be seen in Fig. 34. First, increasing the injection rate increases the film cooling effectiveness. At the exit of the slot, the effectiveness of the injection rates of 1.0%, 1.5%, and 2.0% is unity, and the effectiveness gradually decreases. The maximum film cooling effectiveness is only 0.74 (Tu = 0.75%) for $m_s$ = 0.5%. The average is significantly lower because the coolant does not cover the entire passage, as shown in Fig. 6(a). Near the slot ($x/C_{ax} < 0.4$), the level of the film cooling effectiveness for $m_s$ ranging from 1.0 to 2.0 is the same (including Tu = 0.75% and 13.4%). The blowing ratio effect is clearly seen on the downstream half of the channel ($x/C_{ax} > 0.4$), with the effectiveness being proportional to the injection rate. The effect of freestream turbulence is also shown in this figure; as discussed previously, increasing the turbulence intensity increases the film cooling effectiveness because the passage secondary flow is weaken. The combined effect of weakening the secondary flow by increased injection and increased turbulence increases the film cooling effectiveness by a maximum of 20%. The greatest combined effect is seen for $m_s$ = 1.5%, were the film cooling effectiveness is increased by as much as 80%.

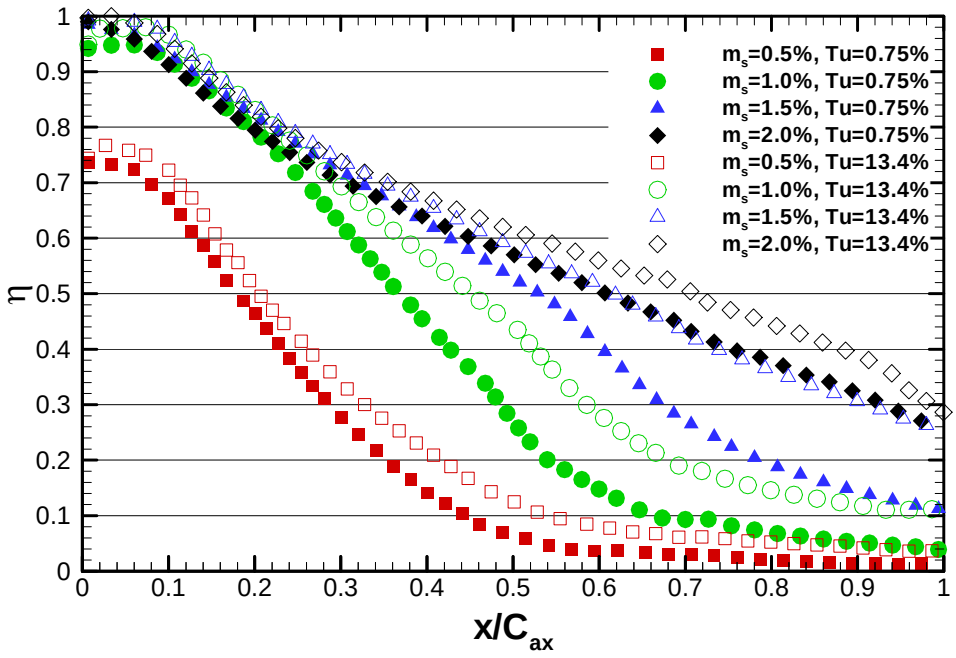


**Fig. 34 Laterally averaged film cooling effectiveness on the passage endwall with upstream slot injection**

The lateral averages for the downstream film cooling holes are shown in Fig. 35. The effect of blowing ratio is seen by comparing Figs. 35(a), (b), (c), and (d). For both turbulence intensities, the film cooling effectiveness decreases with increasing blowing ratio. The effect of freestream turbulence is more complicated. In general, increased freestream turbulence decreases the film cooling effectiveness on the platform (as also shown in Fig. 31). This finding varies from studies of film cooled flat plates. For flat plate studies, it has been shown that increasing the freestream turbulence decreases the film cooling effectiveness at low blowing ratios and increases the effectiveness at high blowing ratios. The film cooling effectiveness on the platform is influenced by both the freestream turbulence intensity and the passage induced secondary flow (passage vortex). Increasing the freestream turbulence increased the effectiveness upstream due to the slot injection. With the turbulence intensity being 13.4% at the inlet of the cascade, the passage vortex was weakened. Near the trailing edge of the passage, where the turbulence intensity is significantly lower (5%) and the passage vortex is weakened, the coolant from the discrete holes can more readily lift off the platform (when compared to the cases without the turbulence grid). Therefore, the effectiveness decreases with increased freestream turbulence due to the combined effect of the freestream turbulence and the passage induced secondary flow.

Figure 36 clearly shows the combined effect of upstream slot injection and downstream discrete film cooling holes. Beginning with the slot injection rate of 1.0%, from the reference case (only upstream slot injection with $m_s = 1.0\%$), the effectiveness drops quickly. However, with the addition of downstream discrete film hole cooling, the

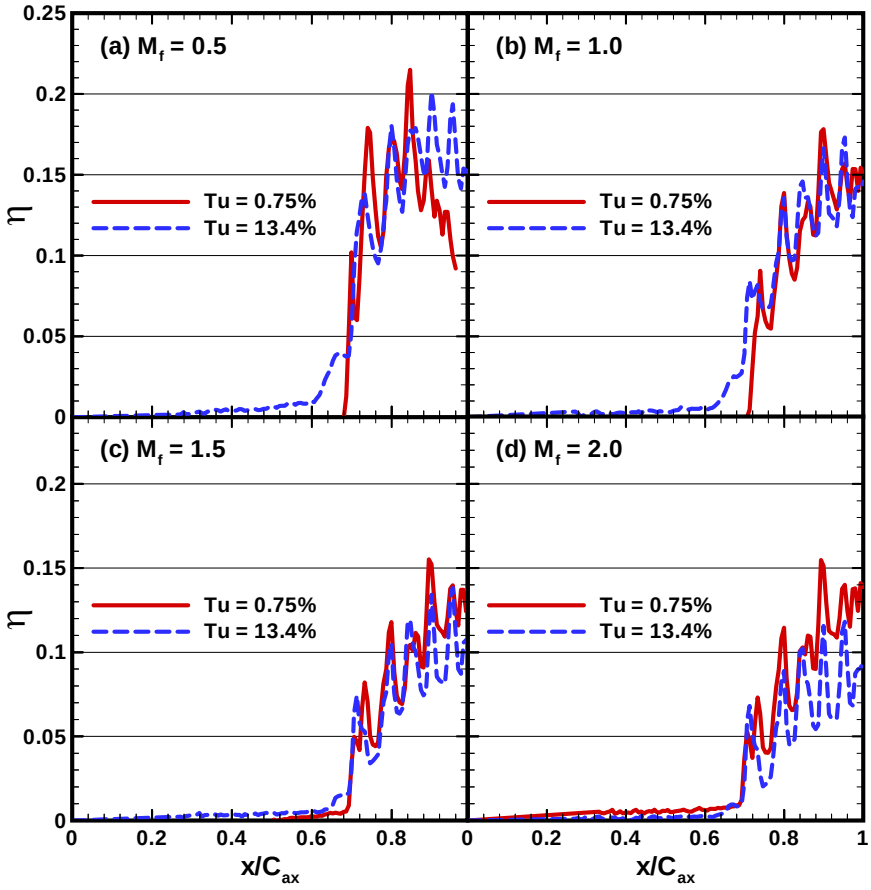


**Fig. 35 Laterally averaged film cooling effectiveness on the passage endwall with downstream discrete film hole cooling**

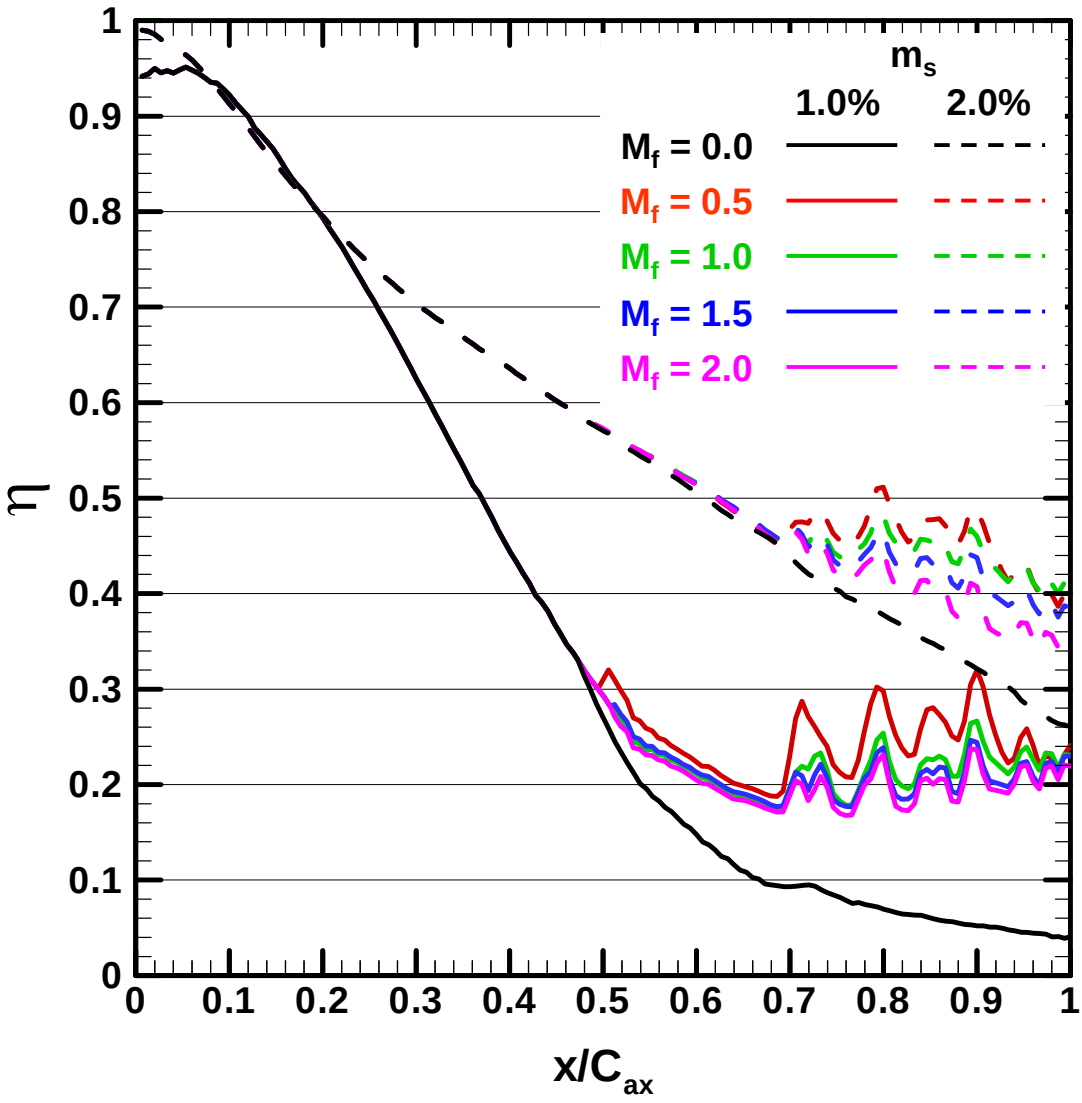


**Fig. 36 Laterally averaged film cooling effectiveness on the passage endwall with combined upstream slot injection and downstream discrete film hole cooling (Tu = 0.75%)**

film cooling effectiveness increases more than 3 times the amount without the discrete film holes, with the greatest increase coming the with lowest film blowing ratio of $M_f$ = 0.5. With the slot injection of 2.0%, the film cooling effectiveness is greater than with 1.0%. The film cooling effectiveness is elevated with the film cooling holes; however, the increase is not as significant as with the injection rate of 1.0%.

When considering the film cooling effectiveness on the passage endwall, there has been a tendency to apply data or correlations obtained from flat plate studies directly to the endwall. Figure 37 illustrates flat plate correlations should be applied to the endwall cautiously. Goldstein [72] gathered experimental data and correlations for the film cooling effectiveness measured downstream of both a slot and discrete film holes. Plotted with the laterally averaged data from the present study are both a correlation for the effectiveness due to discrete, inclined film cooling holes, and a correlation for tangential slot injection. The film cooling effectiveness of the present study is clearly higher than the accepted correlation for discrete hole film cooling. The coolant exiting a discrete film hole is highly three-dimensional with multiple pairs of vortices. These vortices increase the interaction between the coolant the mainstream flow, and thus reduce the film cooling effectiveness. However, when the coolant exits a full coverage slot, the flow is more two-dimensional, with mixing occurring at the coolant – mainstream interface. The reduced mixing results in better film coverage, and therefore, increased film cooling effectiveness.

The interesting comparison is between the present results and the correlation for tangential slot injection. Near the slot ($x/M_sS < 30$), the current experimental data for

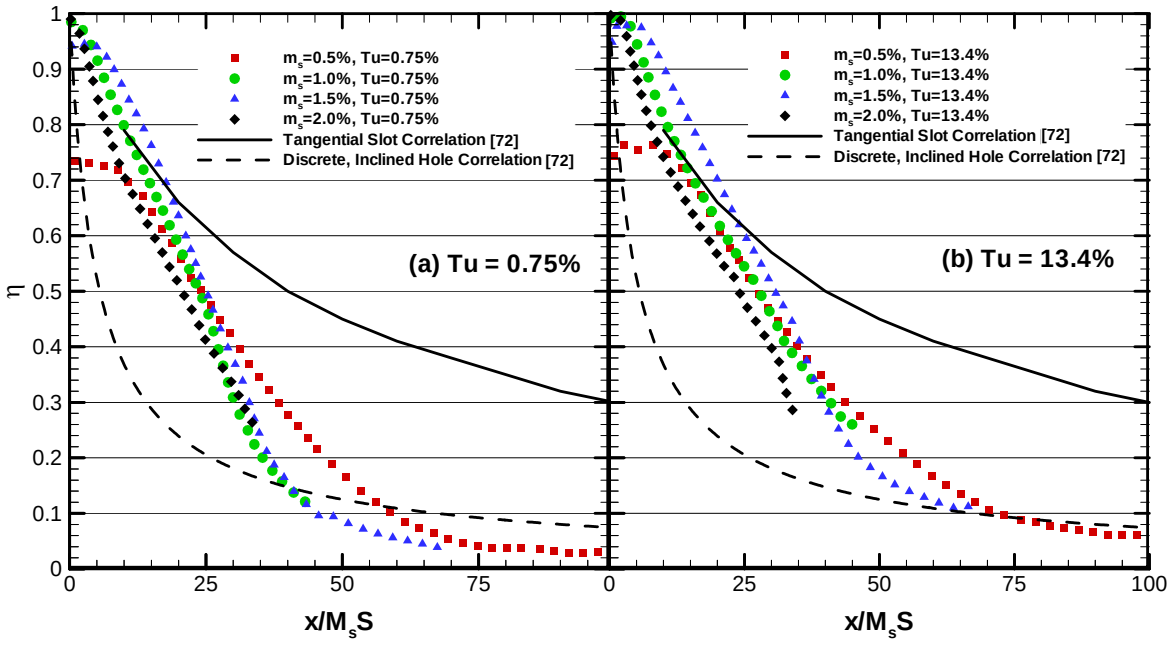


**Fig. 37 Comparison of the laterally averaged film cooling effectiveness on the passage endwall with upstream slot injection with correlations for discrete, inclined film cooling holes and tangential slot injection over a flat plate**

slot injection rates of 1%, 1.5%, and 2% collapse together with the established correlation. The injection rate of 0.5% is lower than the correlation because the coolant does not exit the slot uniformly (Fig. 29(a)). Therefore, the lateral average for this lowest injection rate is lower than the other experimental data and the correlation for tangential injection. However, as $x/M_sS$ increases, the current experimental data deviates significantly from the correlation. Beyond $x/M_sS = 22$, the current experimental data is much lower than the established correlation. The contour plots in Fig. 29 clearly show the skewed effectiveness profiles through the passage. Unlike flow over a flat plate, the effectiveness on the passage endwall decreases due to the passage secondary flow. This variation from the tangential slot correlation is seen for both freestream turbulence levels (Figs. 37(a) and (b)).

***Cooled Platform with Simulated Stator-Rotor Seals***

To study the film cooling effectiveness on the blade platform, the platform was altered, so the advanced seal configurations could be considered upstream of the blades. Three separate seals are considered in the present study. The complexity of the seals gradually increases, to the most complex design, which most closely models actual engine seals. For all cases the upstream seal, shown in Fig. 38, covers 1.5 passages, and the seals are located 4.39 cm upstream of the blades, Fig. 38.

The first seal injects the coolant vertically into the mainstream flow. As shown in Fig. 39(a). The slot width is 0.44 cm, and the coolant travels 1.91 cm through the slot, so $l_s/w = 4.34$. The second seal actually redirects the coolant just before it is

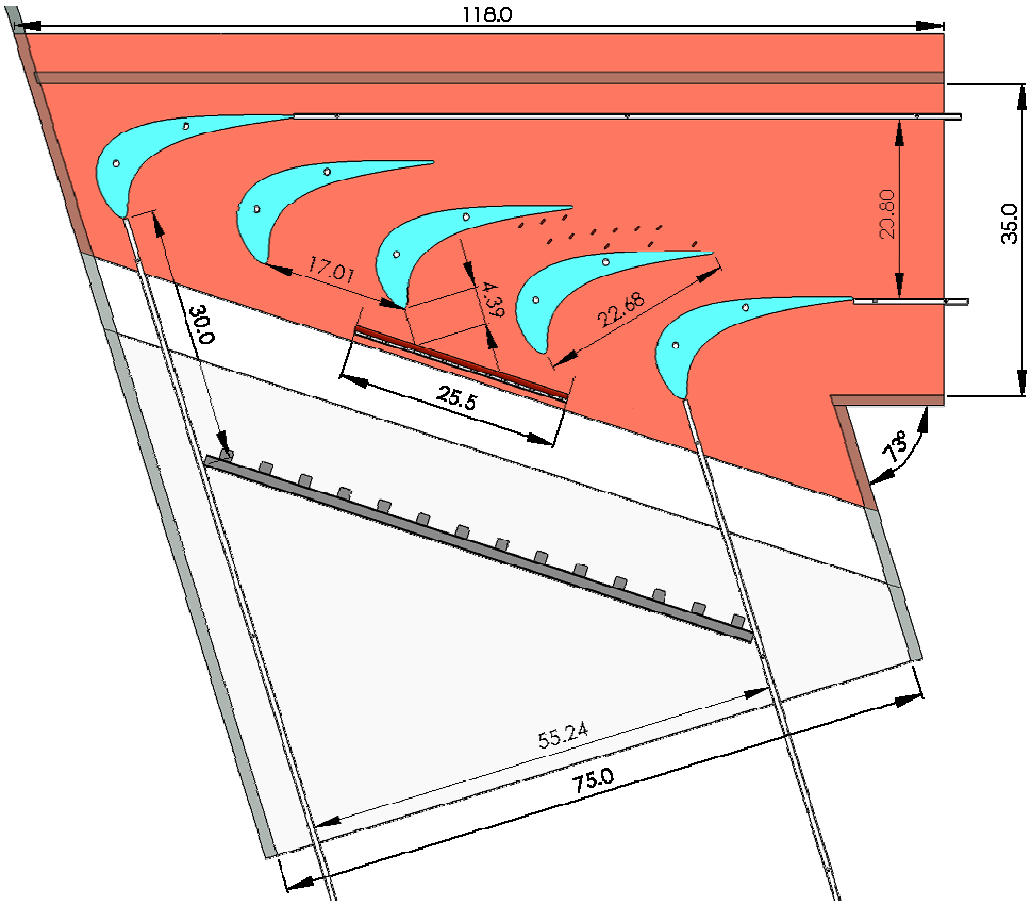


**Fig. 38 Low speed wind tunnel and turbine blade details**

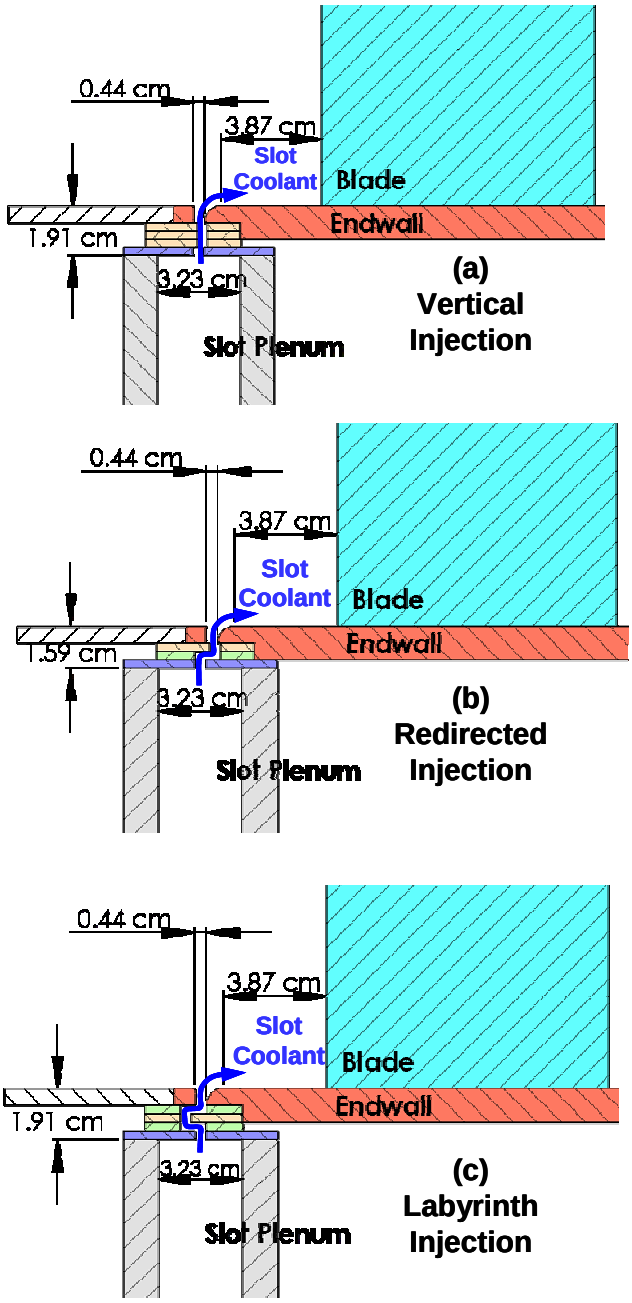


**Fig. 39 Stator-rotor seal configurations. (a) Vertical injection, (b) Redirected injection, and (c) Labyrinth injection**

injected onto the platform. As shown in Fig. 39(b), the coolant is not directly injected into the mainstream flow. This redirection gives a slot length – to – width ratio of 4.84. The third configuration is the most advanced seal configuration. Figure 39(c) shows a configuration that models a labyrinth seal. The coolant is actually turned 180° before it is expelled onto the platform. In this case the distance the coolant travels through the seal increases, so the length – to – width ratio increases to 6.84.

Coolant (air or nitrogen) is metered through a square edge, ASME orifice flow meter and piped to a plenum located directly beneath the slot. The plenum is sufficiently large enough to ensure the coolant is uniformly distributed at the exit of the slot. The flow rate of the slot coolant can be varied, so the film cooling effectiveness can be measured over a range of flow rates varying from 0.5% to 2.0% of the mainstream flow.

The detailed film effectiveness is presented for each configuration over the range of coolant flow rates. Following the discussion of the detailed effectiveness distributions, the seal configurations will be compared, based on the laterally averaged film cooling effectiveness through the passage. The film effectiveness obtained from the present three configurations will also be compared to the film effectiveness resulting from more simplistic (or fundamental) seal configurations.

The film cooling effectiveness measured on the platform with vertical coolant injection upstream of the blades is shown in Fig. 40. As Fig. 40(a) shows, at the lowest coolant flow rate of 0.5%, coolant exits over the entire length of the slot; however, the coolant does not exit the slot uniformly. In addition, the film cooling effectiveness quickly decays from the seal through the passage. From the PSP measurement, the

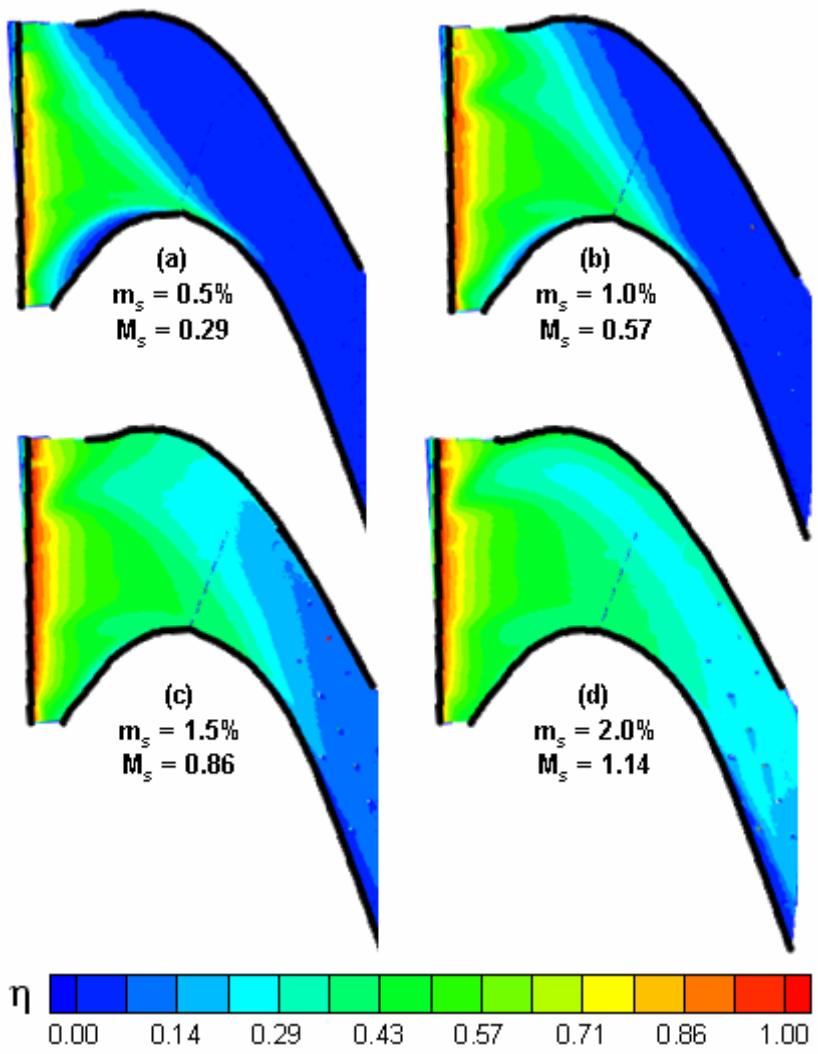


**Fig. 40 Measured film cooling effectiveness with vertical upstream injection**

strong effect of the passage induced secondary flow on the film cooling effectiveness is seen. The coolant is carried from the pressure side of the passage to the suction side with the passage vortex. At this low flow rate, a large area of the passage, both along the pressure side and trailing edge, is left unprotected and exposed to the mainstream gas. Similar trends have been observed with other cooling configurations.

Increasing the coolant flow rate increases the coverage area in the passage. As Fig. 40(b) shows, more area near the pressure side of the passage is covered by the coolant. However, the same behavior of the coolant being forced to the suction side is still observed. Further increasing the flow rate to 1.5% of the mainstream flow (Fig. 40(c)) yields increased film cooling effectiveness on the upstream half of the passage with the film penetrating further downstream. Increasing the coolant flow rate also reveals how non-uniformly the coolant exits the slot. As shown in Fig. 40(d), a large area of relatively low effectiveness develops near the pressure side of the passage. With the coolant being injected into the mainstream upstream of the blades, the path of the coolant is heavily influenced by the formation of the horseshoe vortex. As Friedrichs et al. [17] showed from oil and dye surface visualizations, the horseshoe vortex forms in the stagnation region upstream of the blade. With this vertical injection of the coolant, there is strong interaction between the coolant and the mainstream. With the formation of the horseshoe vortex, the pressure side leg becomes the passage vortex as it moves from the pressure to the suction side of the passage. This passage induced flow carries the majority of the coolant from the pressure side of the passage to the suction side. Downstream of the passage vortex, near the pressure side of the passage, a large area of

relatively low film cooling effectiveness is present. With the large amount of coolant from the seal, 100% of the coolant is not swept to the suction side of the passage. Although the effectiveness is less near the pressure side, the film cooling effectiveness is not zero.

At the largest flow rate of 2.0% of the mainstream flow, the passage is completely covered from the leading edge to the trailing edge. However, if the present results are compared to an inclined slot, the effectiveness near the trailing edge is much lower for this vertical injection, at a given flow rate. This should be expected as with the present vertical injection, the coolant tends to blow off the platform, and the cooling advantage is minimized. Whereas, when the coolant is injected at an angle to the mainstream flow, the coolant is more likely to remain attached to the platform.

With this vertical injection, there is a strong interaction of the coolant flow with the mainstream flow (including the passage induced secondary flow). The formation and migration of the passage vortex across the passage is clearly seen by the measured film cooling effectiveness. Due to this strong interaction of the coolant with the mainstream, the film cooling effectiveness distribution through the passage is very non-uniform from the leading edge to the trailing edge of the passage.

The film cooling effectiveness measured on the platform with the upstream seal redirecting the coolant is shown in Fig. 41. As with the previous geometry, the film effectiveness is measured on the platform with four different coolant flow rates. The general behavior of the coolant being carried by the passage vortex from the pressure side to the suction side of the passage is still apparent. However, with the present

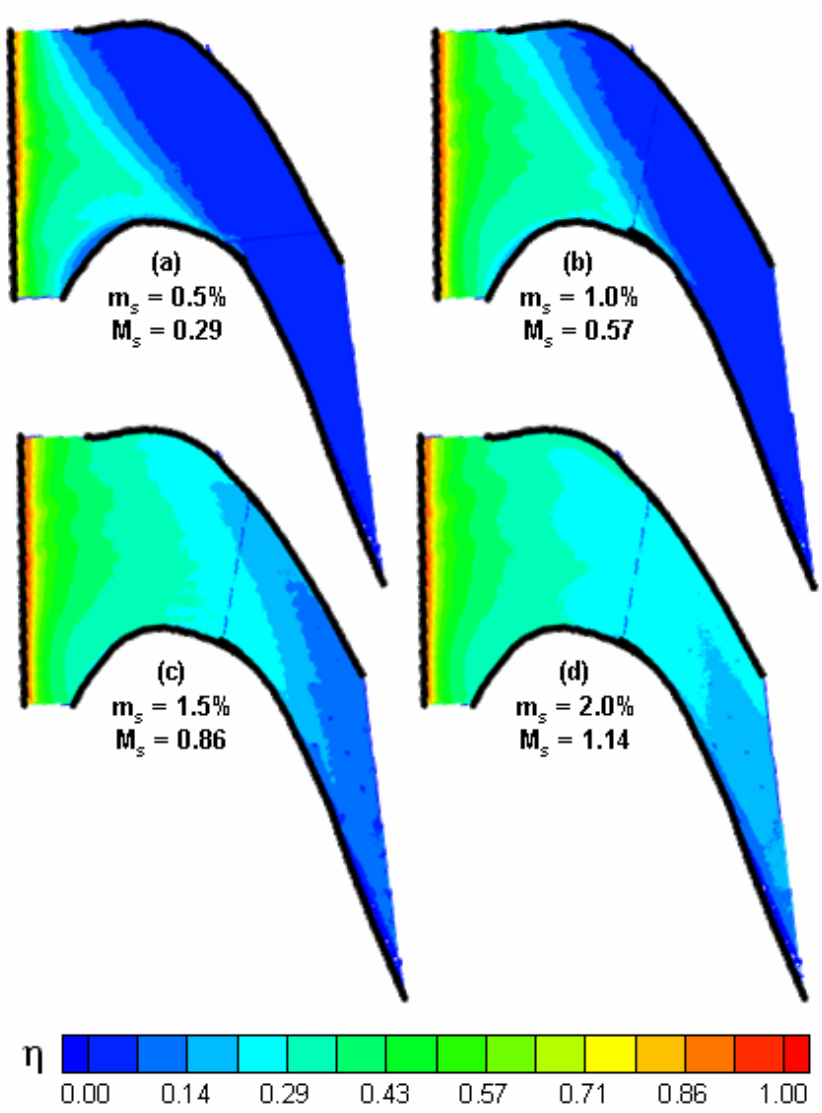


**Fig. 41 Measured film cooling effectiveness with redirected upstream injection**

configuration, the coolant exits the seal more uniformly than with the previous case. At the lowest flow rate of 0.5%, the protection offered by this seal redirecting the coolant is equitable to the seal which injects the coolant vertically onto the platform.

At the increased coolant flow rates, the effectiveness trends vary significantly from those of the vertical injection. The film cooling effectiveness is more uniform across the passage, but the effectiveness decays rapidly through the passage. Almost immediately downstream of the slot, the effectiveness drops from 1.0 to approximately 0.6. The coolant exits the slot more uniformly, at the expense of the effectiveness rapidly decaying. With this more advanced flow configuration, the severe effects of vertical injection are reduced, so the coolant more readily remains attached to the platform.

Figure 42 shows the film effectiveness distributions measured with the most advanced stator-rotor seal: a labyrinth-like seal. The effectiveness distributions for this most complex seal configuration are very similar to those with the coolant redirection (Fig. 41). This might be anticipated as the two configurations are identical near the exit of the seal. The effect of the passage induced secondary flow remains very obvious, most notably at the lower flow rates. However, with the more complex labyrinth-like seal, the film cooling effectiveness is reduced through the passage.

As it is likely anticipated, increasing the complexity of the seal configuration reduces the film cooling effectiveness on the blade platform (Figs. 40 – 42). The point is reiterated by comparing the present configurations to the more idealistic inclined slot. With all three of the present configurations, the effectiveness immediately

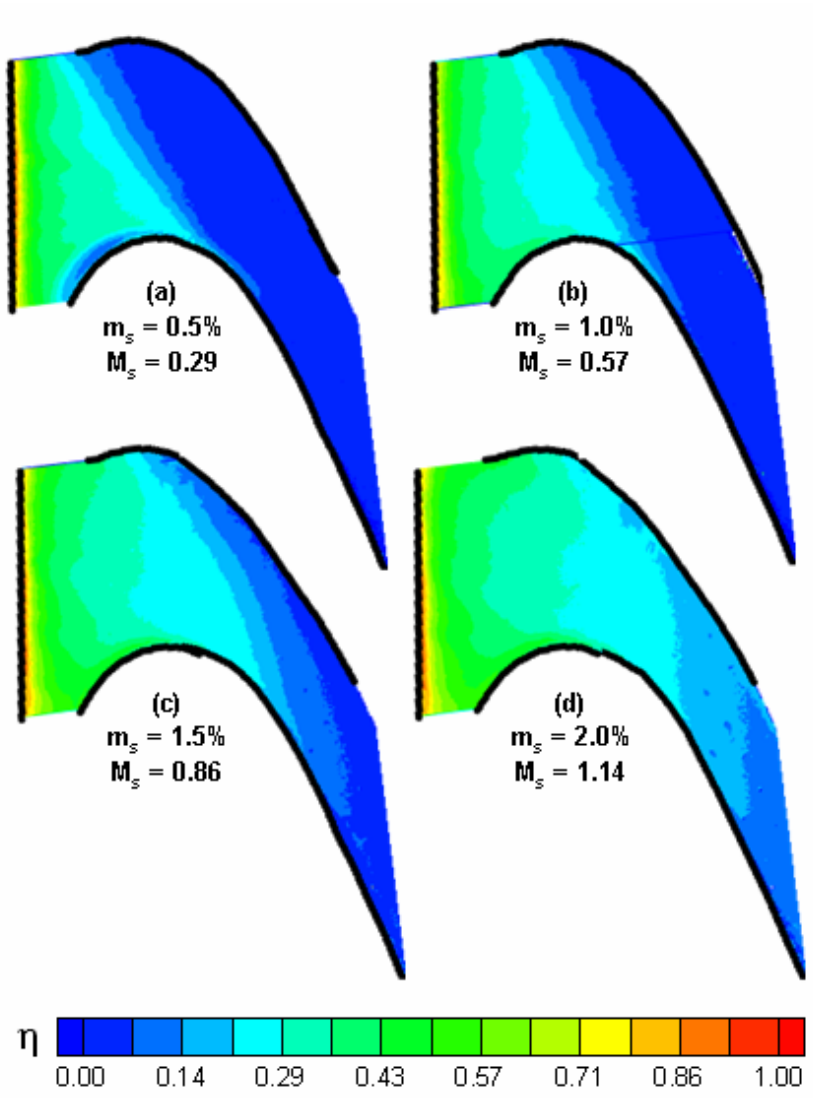


**Fig. 42 Measured film cooling effectiveness with labyrinth upstream injection**

downstream of the slot quickly decays; this is the due to the injection of the coolant nearly perpendicular to the mainstream flow. Depending on the amount of coolant through the seal, the passage vortex strongly influences the behavior the coolant remaining near the platform. With lower flow rates (less momentum flows), the coolant is carried by the passage vortex from the pressure side of the passage to the suction side. When the coolant flow rate is increased, the effect of the passage vortex is weakened, and the coolant covers a larger area of the passage, extending nearly to the trailing edge of the blades.

For more direct comparisons of the different seal configurations, the laterally averaged film cooling effectiveness is plotted in Figs. 43 – 46. The three configurations of the present investigation are considered along with the fundamental inclined slot. Figure 43 shows the effect of the coolant flow rate on the film cooling effectiveness for each seal configuration. The leading edge of the blades is located at x = 0. As shown in the Fig. 39, the seals of the present study are located upstream of the leading edge, and thus the effectiveness is plotted upstream of x = 0. As shown in Fig. 43, increasing the coolant flow rate increases the effectiveness through the passage for all seal configurations. The film cooling effectiveness for the three current geometries decays rapidly from the initial injection, and this was clearly shown with the previously discussed contour plots.

Figure 44 shows the effect of the seal configuration at each of the given flow rates. These plots clearly indicate how the effectiveness on the platform decreases with the more advanced geometries. At the lowest coolant flow rate of 0.5%, the three

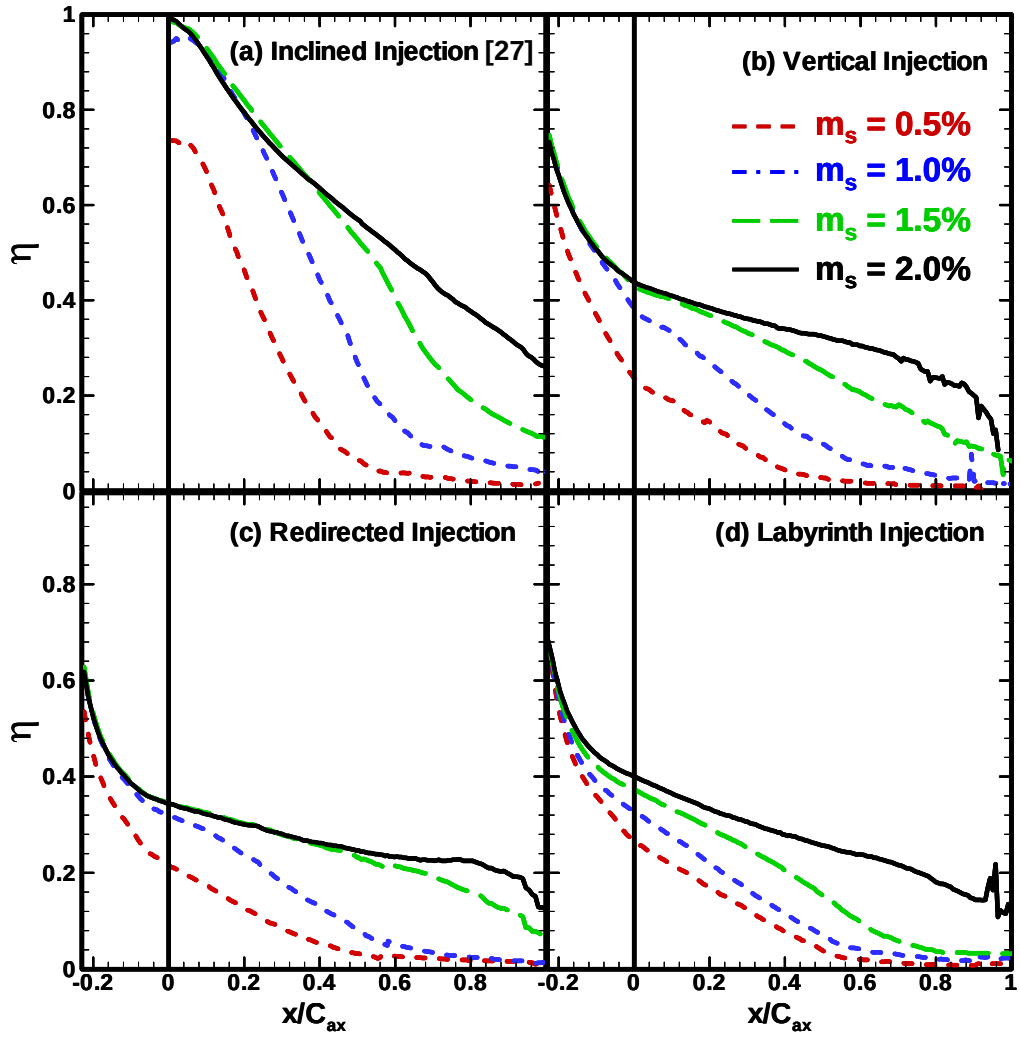


**Fig. 43 Laterally averaged film cooling effectiveness on the passage endwall for different seal configurations (coolant flow rate effect)**

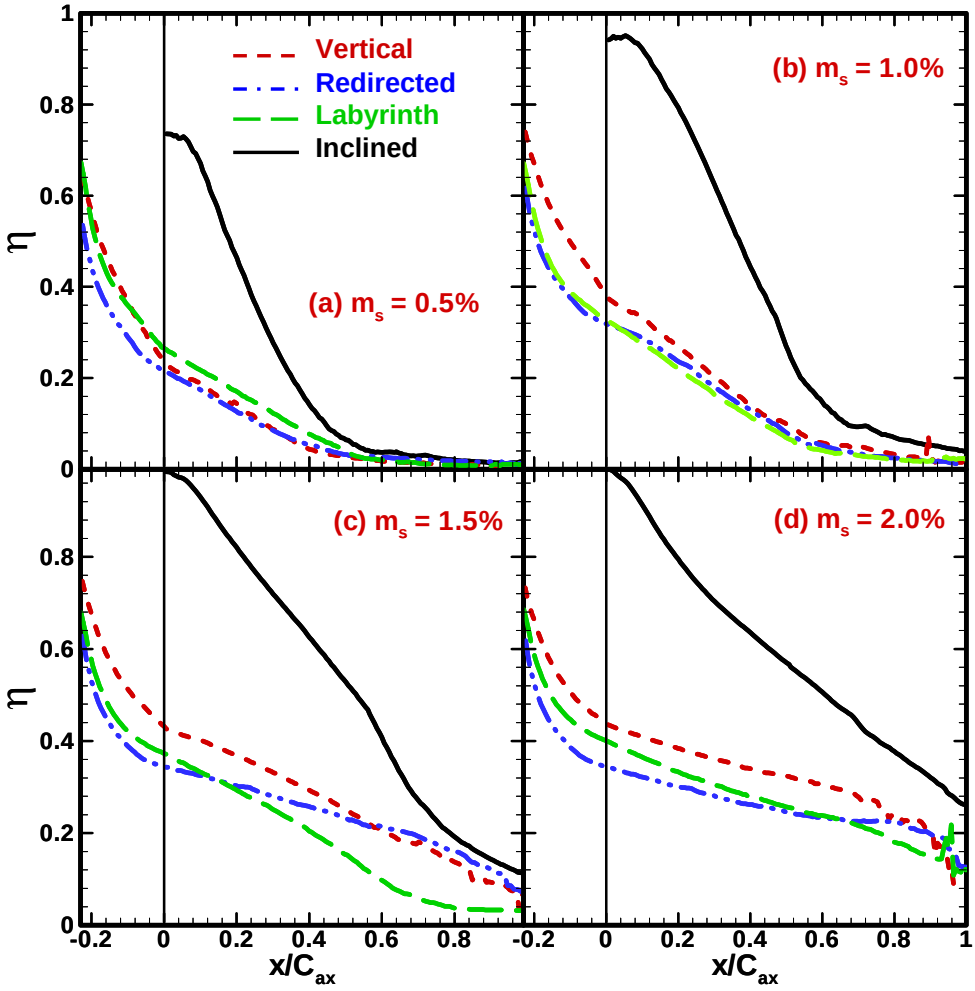


**Fig. 44 Laterally averaged film cooling effectiveness on the passage endwall for different coolant flow rates (seal configuration effect)**

current configurations produce the same level of cooling protection. The film effectiveness quickly diminishes as the coolant is whisked away by the passage vortex. Increasing the coolant flow rates produces marginal variations between the present seal configurations. However, for all four coolant flow rates, the film effectiveness for these advanced configurations is significantly lower than for the incline slot. This plot also clearly shows why the incline slot is advantageous, as the film effectiveness decreases through the passage, the decline is not as severe as with the advanced seals. Although the effectiveness decreases quickly from the seal, it should be noted with the seals located upstream of the blades, more area is covered by the coolant. At the highest flow rates, the purge gas covers the entire passage from upstream to the trailing edge of the blades.

Figures 45 and 46 show the laterally averaged film cooling effectiveness plotted versus $x/M_s s$. It must be noted that coordinates for the current configurations have been adjusted, so the exit of the seal is considered the starting point ($x = 0$). This has been for a more direct comparison with other slot configurations. As Fig. 45 shows, the flow rate (blowing ratio) effect is eliminated from the laterally averaged effectiveness. In addition to the three present configurations and the previous inclined slot, the measured effectiveness is also compared to the most ideal case of tangential slot injection over a flat plate [72]. As explained by previously, the averaged effectiveness near the slot collapses with the established correlation near the slot (Fig. 45(a)). However, downstream of the slot, the effectiveness on the platform drops quickly due to the passage induced secondary flow. Comparing the three current seals, even near the seal,

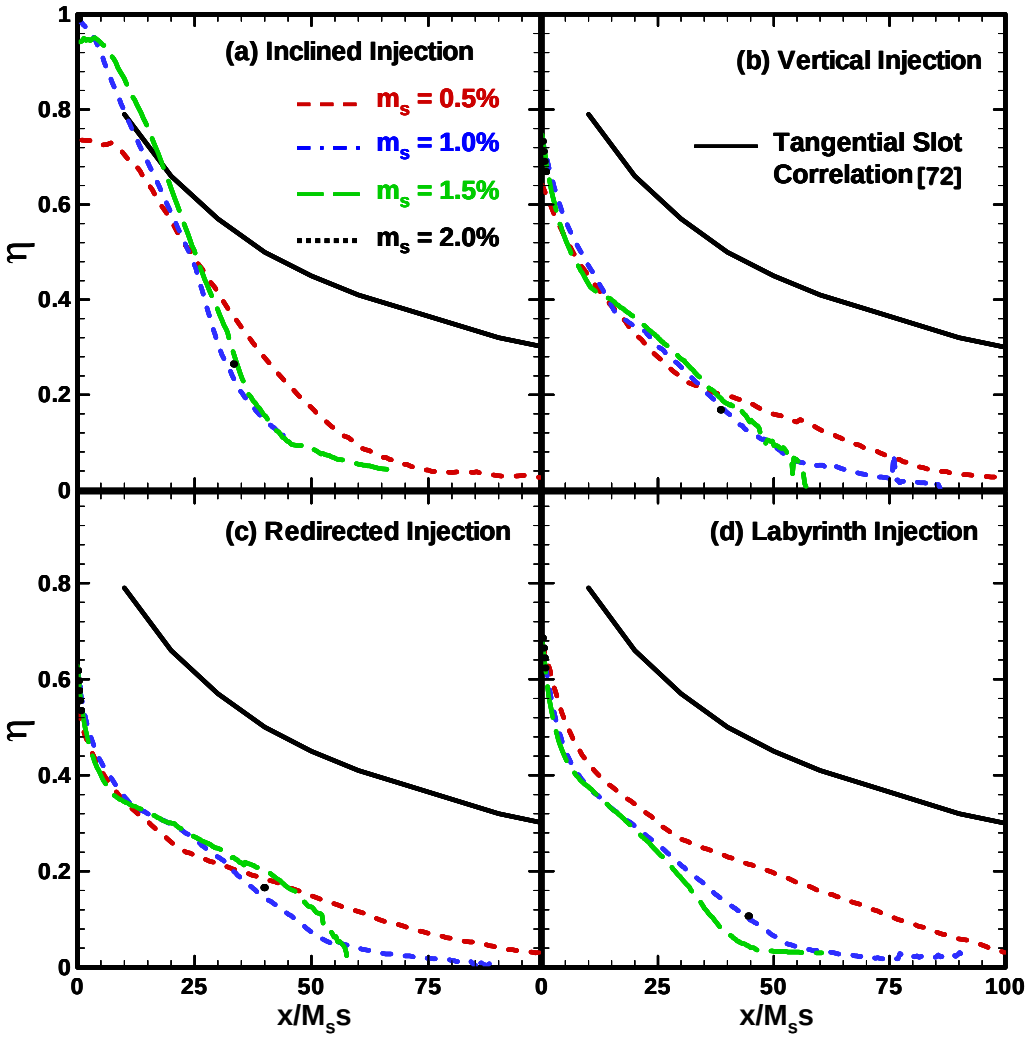


**Fig. 45 Laterally averaged film cooling effectiveness on the passage endwall for different seal configurations (coolant flow rate effect)**

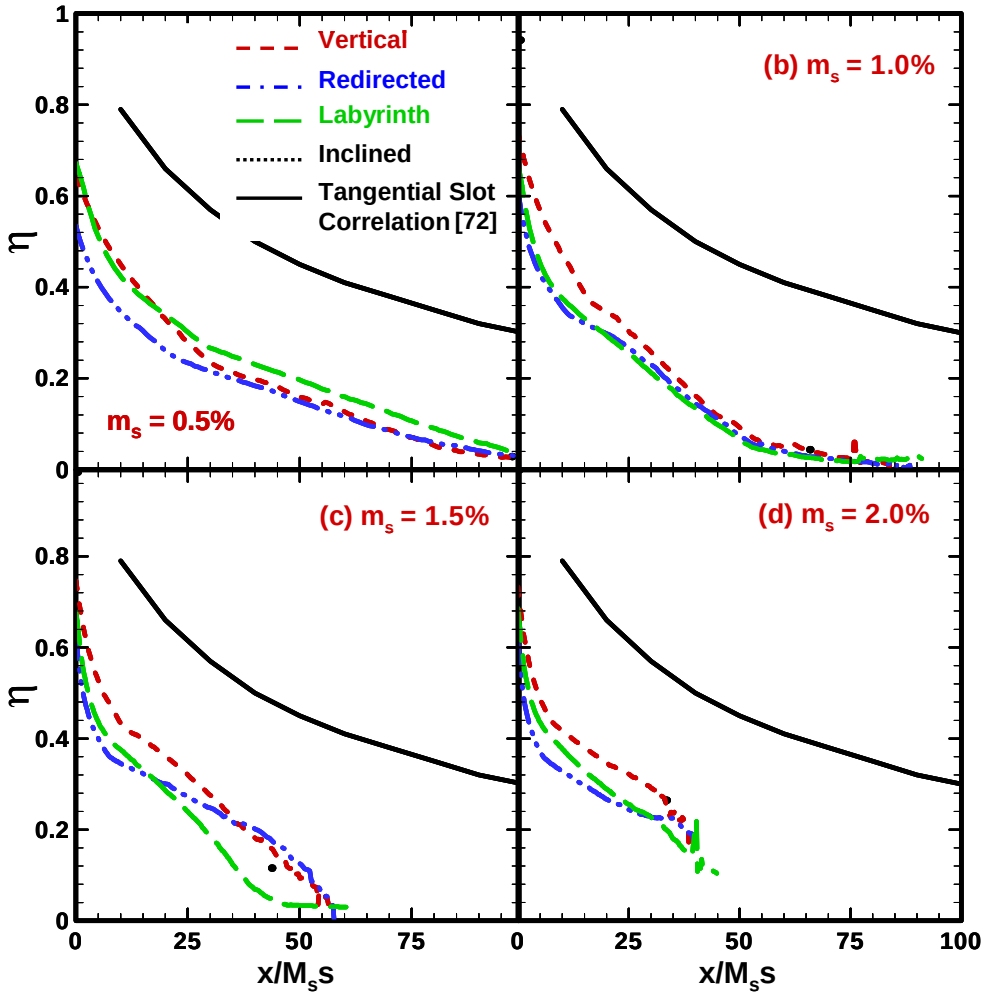


**Fig. 46 Laterally averaged film cooling effectiveness on the passage endwall for different coolant flow rates (seal configuration effect)**

the effectiveness is significantly lower than with the tangential injection. This is understood due to the nearly vertical injection of the coolant into the mainstream. Finally, the effect of each seal configuration can be seen in Fig. 46. As the figure clearly shows, the vertical, redirected, and labyrinth seals yield the same leave of protection, and the film effectiveness from these seals is much lower than the inclined slot and the tangential slot.

***Cooled Platform with Stator-Rotor Purge Flow and Compound Film Cooling Holes***

The platform within the linear cascade has been altered to incorporate an advanced, labyrinth-like seal upstream of the blades. As shown in Fig. 47, the seal covers 1.5 passages within the linear cascade. The width of the slot is 0.44 cm, and the coolant travels through the labyrinth-like geometry ($l_s/w = 6.84$), turning 180° before being expelled on the passage endwall. The seal is located upstream of the leading edge of the blades. It is placed 4.34 cm upstream of the blades, so it is approximately halfway between the leading edge of the blades and trailing edge of the stator vanes. An ASME orifice meter is used to measure the coolant flow rate before the coolant fills a plenum and is then expelled onto the platform. The flow rate of the coolant is varied, so the film cooling effectiveness can be measured over a range of flow rates varying from 0.5% to 2.0% of the mainstream flow.

Figure 47 also shows the location of the discrete film holes. With the upstream seal providing protection to the upstream half of the passage, additional holes are limited to the downstream half of the passage. Twelve holes are positioned to follow the

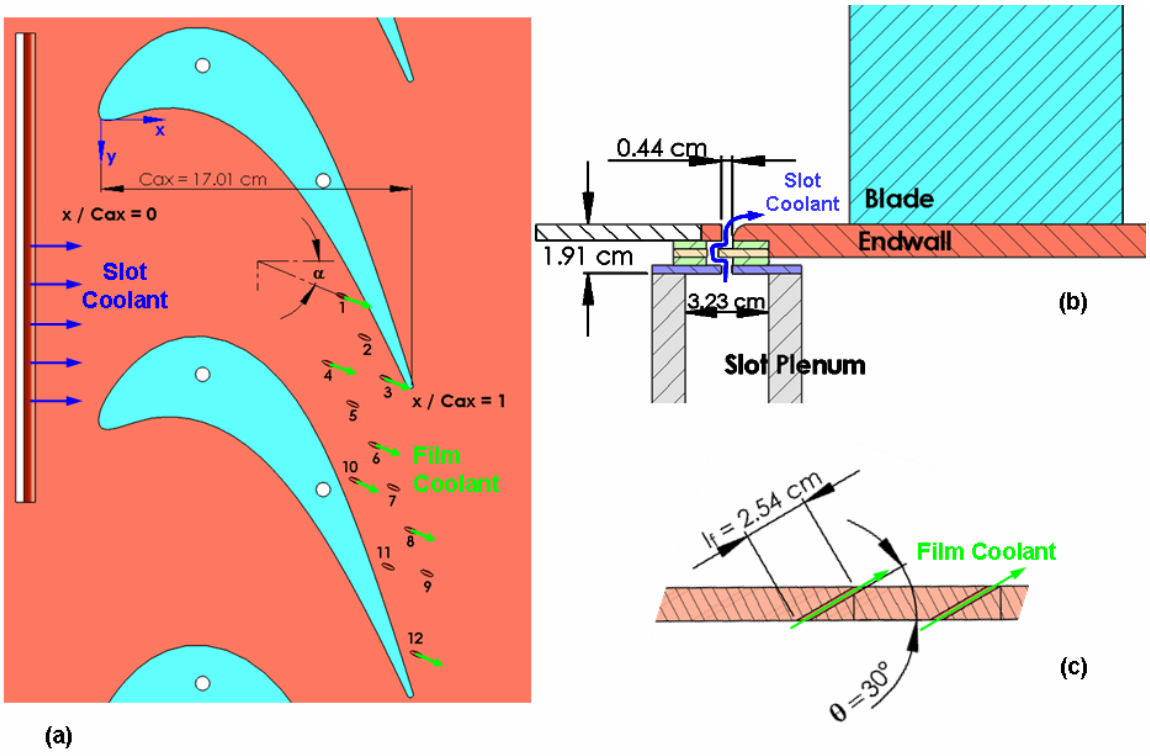


**Fig. 47 Platform film cooling details. (a) Detailed view of the cooled passage, (b) Labyrinth-like stator-rotor seal, and (c) Cross-sectional view of 2 discrete film holes**

potential streamlines through the passage. However, they are placed at a compound angle to the approximate streamlines. The holes are turned 45° toward the pressure side of the passage from the streamline injection angle. Table 3 gives the detailed location and flow angle for the twelve film cooling holes. Although the flow angle of the holes varies, the injection angle through the platform remains constant for each hole at 30°. A second plenum supplies coolant to the holes after the coolant is metered through a volumetric flow meter. The flow rate is varied to achieve average blowing ratios varying from 0.5 to 2.0 (based on the velocity of the mainstream at the exit of the cascade).

The baseline case of the measured film cooling effectiveness on the platform with upstream injection from the labyrinth seal is shown in Fig. 48 (Tu = 0.75%). The effect of the passage secondary flow is clearly seen in this figure. At the lowest coolant flow rate of 0.55, the coolant exits the seal, and as the coolant travels into the blade passage, it is quickly carried from the pressure to the suction side of the passage. As other studies have shown, the pressure side leg of the horseshoe vortex, which forms near the leading edge of the blades, becomes known as the passage vortex as it crosses the passage from the pressure side to the suction side. Beginning at the leading edge of the blades, the film cooling effectiveness quickly diminishes, and the coverage area is skewed to the suction side of the passage. With the stator-rotor seal located upstream of the leading edge of the blades, the coolant exits the seal uniformly over the entire length of the seal. This trend was not observed with an inclined slot located at the leading edge of the blades. The combination of the advanced seal configuration and the location of

**Table 3 Discrete film hole location and orientation**

| Film Hole Number | x (cm) | y (cm) | d (cm) | $\alpha$ | $\theta$ |
|---|---|---|---|---|---|
| **1** | 13.3 | 9.8 | 0.25 | 16° | 30° |
| **2** | 14.5 | 12.1 | 0.25 | 16° | 30° |
| **3** | 15.7 | 14.4 | 0.25 | 16°° | 30° |
| **4** | 12.6 | 13.5 | 0.25 | 10.5° | 30° |
| **5** | 13.9 | 15.8 | 0.25 | 16° | 30° |
| **6** | 15.1 | 18.0 | 0.25 | 19° | 30° |
| **7** | 16.1 | 20.4 | 0.25 | 12° | 30° |
| **8** | 17.1 | 22.7 | 0.25 | 27° | 30° |
| **9** | 18.0 | 25.1 | 0.25 | 27° | 30° |
| **10** | 14.0 | 20.0 | 0.25 | 27° | 30° |
| **11** | 15.9 | 24.7 | 0.25 | 27° | 30° |
| **12** | 17.4 | 29.6 | 0.25 | 27° | 30° |

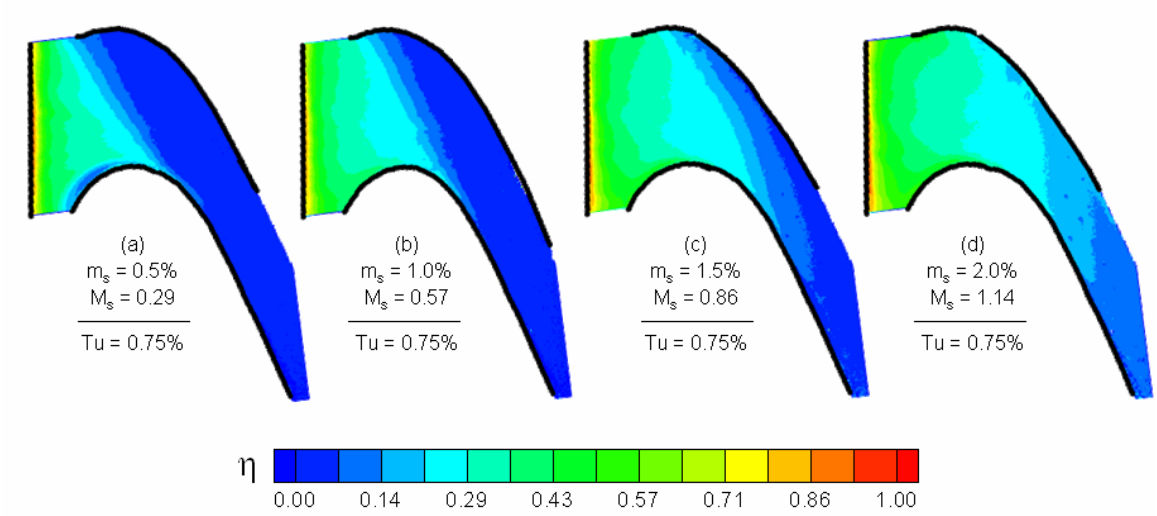


**Fig. 48 Film cooling effectiveness with various seal injection rates (Tu = 0.75%)**

the seal, with respect to the blades, offers added protection against the ingestion of the hot mainstream gases into the engine cavity.

Increasing the coolant flow rate offers added to protection to the downstream half of the passage. However, coolant does not reach the exit of the passage until the seal flow rate is increased to 2.0%. With the intermediate flows of 1.0% and 1.5%, a large area of the platform is left unprotected, and the coolant is adversely affected by the passage induced secondary low. At the greatest flow rate of 2.0%, the film cooling effectiveness distributions are the most uniform from the pressure side to the suction side of the passage. As other studies [24] have indicated, the effect of the passage vortex is weakened by the upstream purge flow. Therefore, the coolant from the seal is more uniformly distributed across the passage.

Although it is convenient to measure the film cooling effectiveness with a low freestream turbulence level of 0.75%, this flow condition is poorly represents the actual engine environment. To combat this problem, a turbulence grid is added to the wind tunnel upstream of the blades, so the freestream turbulence intensity is raised to 13.4% at the cascade inlet. Figure 49 shows the measured film cooling effectiveness on the passage platform with this increased freestream turbulence. A quick comparison of Figs. 5 and 6 does not reveal appreciable difference between the two mainstream flow conditions. However, upon a more careful assessment, several differences can be observed. At the lowest two flow rates of 0.5% and 1.0%, the coverage area extends further into the passage with the increased turbulence intensity of 13.4% than 0.75%. The reduced effect of the passage vortex is further shown at the increased flow rate of

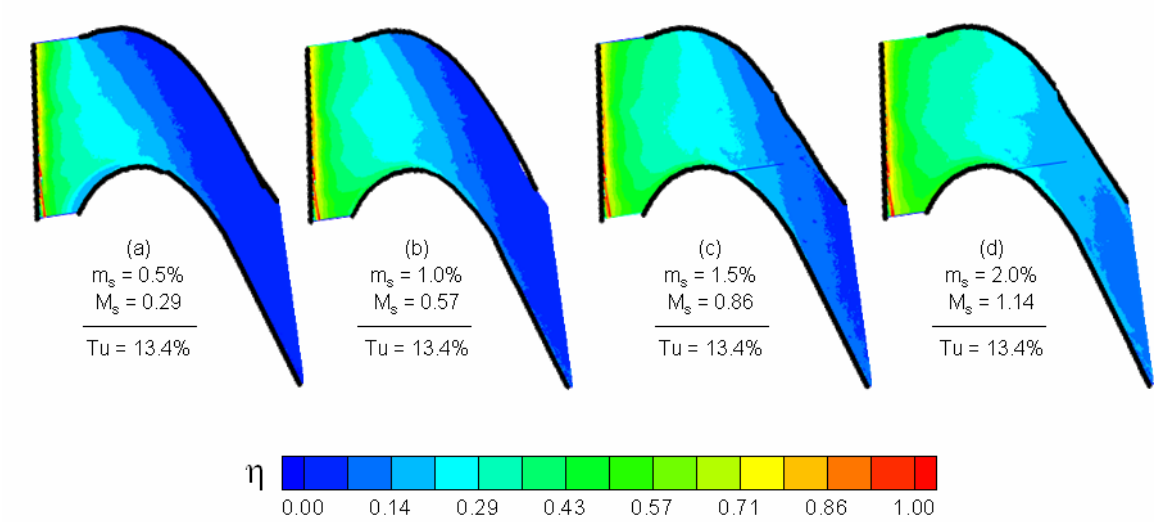


**Fig. 49 Film cooling effectiveness with various seal injection rates (Tu = 13.4%)**

1.5%. At this coolant flow rate, a large area of the passage remains protected by the coolant, but the film cooling effectiveness distributions are more uniform from the pressure side to the suction side of the passage. With a final comparison of the greatest seal flow rate of 2.0%, the film cooling effectiveness distributions obtained under the two freestream turbulence levels show only marginal differences.

The film cooling effectiveness on the platforms is averaged to yield a direct comparison between the various cases. Figure 50 shows the laterally averaged effectiveness through the passage with both freestream turbulence levels. With the seal placed upstream of the turbine blades, the effectiveness is averaged beginning at the exit of the seal, through the passage, to the trailing edge of the blades. Immediately downstream of the seal, all flow rates give the same level of film cooling effectiveness. With the specific geometry of the seal, the film cooling effectiveness directly downstream of the seal is less than unity. However, downstream of the seal, the level of effectiveness begins to disperse depending on the coolant flow rate: the greatest film cooling effectiveness is the result of the greatest flow rate and vice versa. When considering the cases with the turbulence intensity of 0.75%, the effectiveness decreases to approximately zero at the same location in the passage with the lowest coolant rates of 0.5% and 1.0%. However, this point occurs further downstream with the increased flow rate of 1.5%, and with the greatest flow rate of 2.0%, this point is never reached.

In addition to the effect of the coolant flow rate, Fig. 50 also presents the effect of the freestream turbulence intensity. In general, increasing the turbulence intensity increases the film cooling effectiveness, as the adverse effect of the passage vortex is

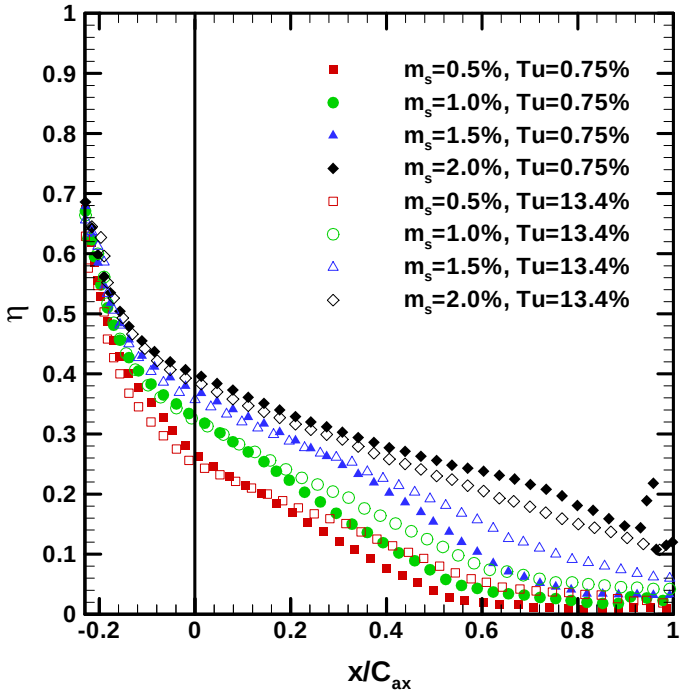


**Fig. 50 Laterally averaged film cooling effectiveness on the passage endwall with upstream seal injection**

reduced. At the highest coolant rate of 2.0%, there is only a slight difference between the two turbulence intensities. The effect of the passage vortex has already been weakened by the large amount of coolant injected onto the platform upstream of the blades. Therefore, no additional weakening of the passage induced secondary flow is observed.

The laterally averaged film cooling effectiveness has been re-plotted in Fig. 51, so comparisons can be made with the fundamental, tangential slot injection over a flat plate. The film effectiveness has been plotted verses the non-dimensional $x/M_s s$ parameter, and it should be noted for this plot, the starting point of $x = 0$ is taken at the exit of the seal (and not at the leading edge of the blades). Near the exit of the slot, all the coolant flow rates collapse together; however, the trends begin to change beyond $x/M_s S = 25$. For both freestream turbulence level of 0.75% and 13.4%, the coolant flow rates of 1.0% and 1.5% approach an average effectiveness of zero. However, with the flow rate of 0.5%, the effectiveness does not approach zero until $x/M_s S$ extends beyond 100.

Figure 51 also offers an interesting comparison with the fundamental tangential slot injection over a flat plat from Goldstein [72]. The coolant exits the tangential slot at $x/M_s S = 0$, as the current labyrinth seal has been shown. A dramatic difference in the film cooling effectiveness can be quickly observed. It was previously observed that near the exit of their inclined slot, the effectiveness is comparable to that predicted by the tangential correlation, and deviation from the correlation was not observed until the effect of the passage induced secondary flow dominated the film cooling effectiveness

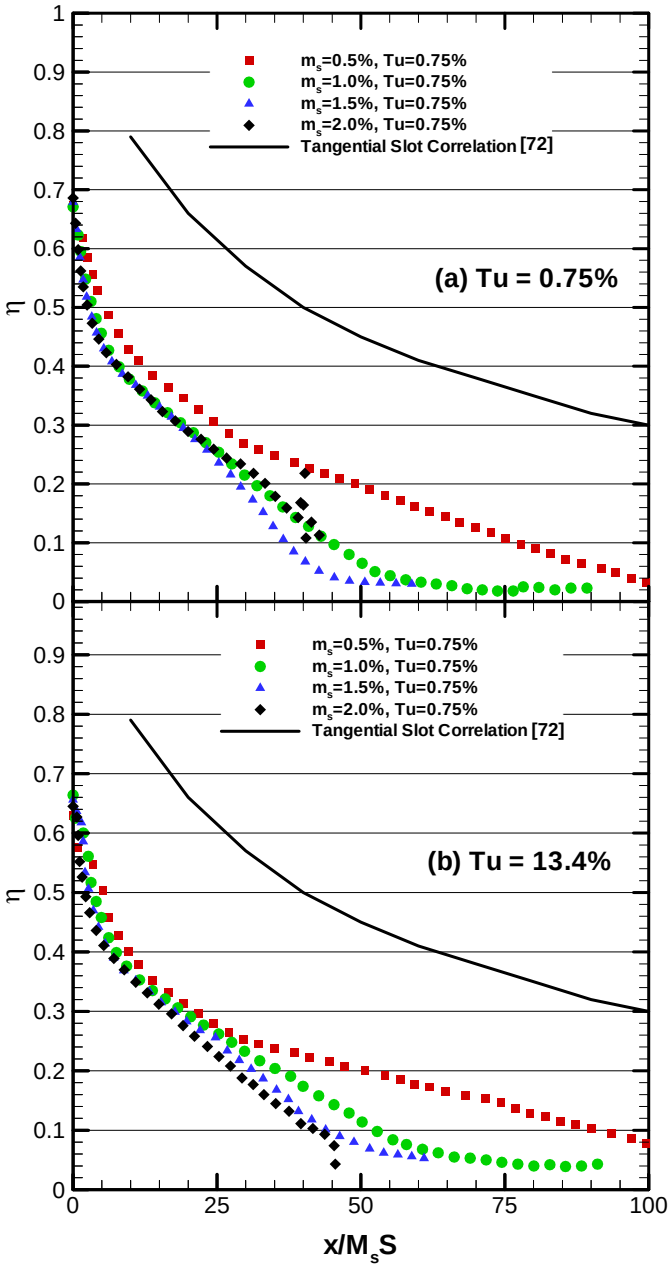


**Fig. 51 Comparison of the laterally averaged film cooling effectiveness on the passage endwall with upstream seal injection and tangential slot injection over a flat plate**

on the platform. The present labyrinth geometry gives much lower effectiveness than the tangential slot, so beginning at the exit of the seal, the large deviation from the correlation is observed. The difference continues through the passage coolant is adversely effected by the passage vortex.

Before considering the more realistic cooling design of seal flow combined with discrete film cooling, is isolated effects should first be understood. Therefore, it is necessary to consider the discrete film holes separately from the seal coolant. Figure 52 shows the measured film cooling effectiveness due to the downstream, discrete film cooling holes with both freestream turbulence level of 0.75% and 13.4%. Before discussion of the discrete film cooling begins, several items should be noted and remembered as the discussion progresses. Although the elevated turbulence intensity is stated as 13.4%, this level occurs at the inlet of the cascade. At the exit of the cascade, near the discrete holes, the turbulence intensity reduces to approximately 5% [71]. In addition, as described earlier, the location of the holes follow the streamlines through the passage, and have a compound angle 45° toward the pressure side of the passage. The blowing ratios stated for the holes are average blowing ratios based on the mainstream velocity at the exit of the cascade.

As Fig. 52(b) shows at the lowest blowing ratio of $M_f = 0.5$, distinct traces are seen from each of the 12 film cooling holes. However, the path of each of the coolant traces is rather interesting. Arrows have been added to the plot to indicate the injection angles of selected holes. The deviation of the coolant traces from the injection angles is very apparent. The twelve holes can be divided into three groups: pressure side, center

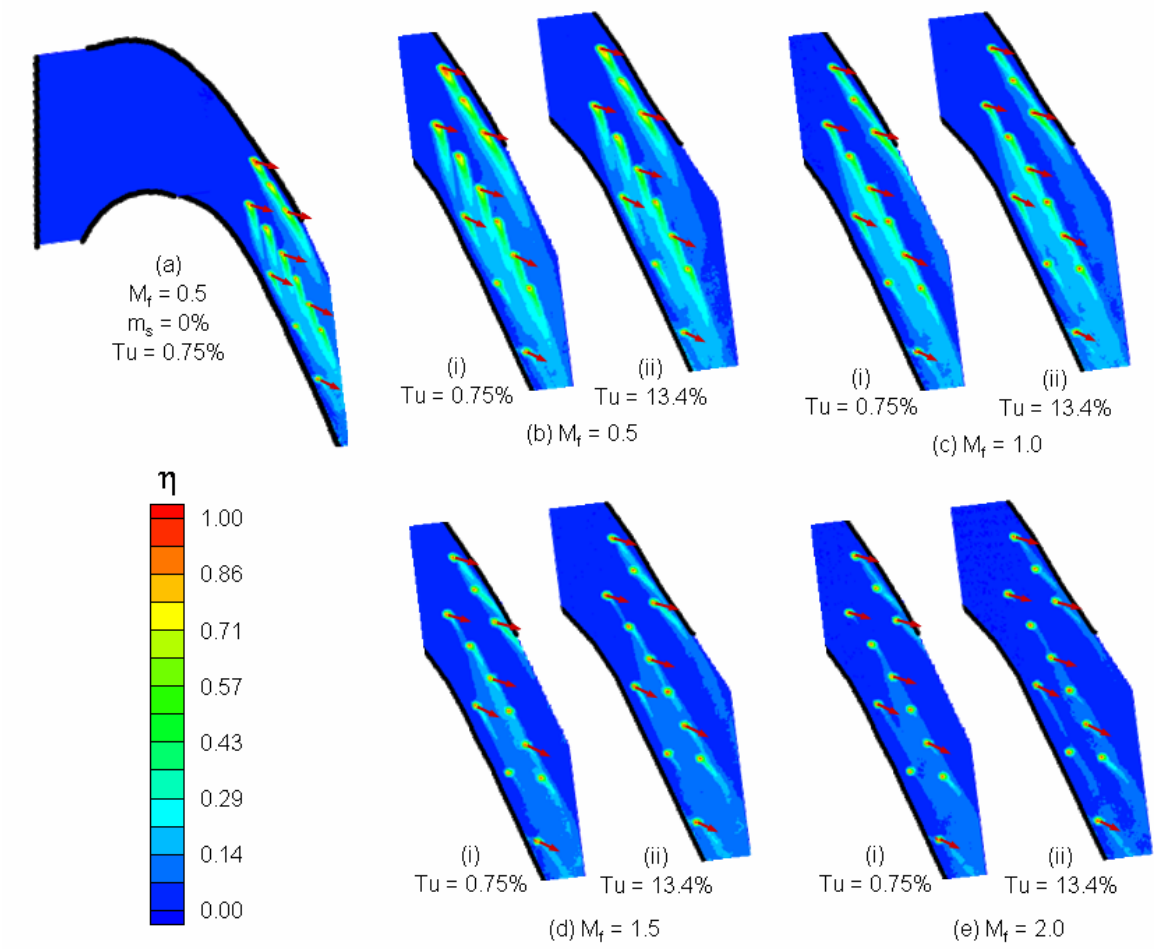


**Fig. 52 Film cooling effectiveness with downstream discrete film cooling**

of the passage, suction side. The coolant from the three holes along the pressure side of the passage follows the curvature of the blade (mainstream flow). Although the injection of the coolant is directed toward the pressure side of the passage, the flow of the coolant is dominated by the mainstream flow.

Moving to the center of the passage, the path of the coolant changes dramatically. The traces are nearly from the pressure side to the suction side of the passage, especially with the upstream holes. For this center row of holes, the path of the coolant is dominated by the passage induced secondary flow. The passage vortex moving from the pressure side to the suction side of the passage severely influences the path of the coolant. This behavior was previously observed with holes angled with the streamlines. With these compound angle holes, the coolant traces are wider, and the coolant spreads more as it is directed toward the suction side of the passage. These wider traces come at the expense of shorter traces, which can be expected when the same amount of coolant is used for both cooling designs. Near the trailing edge of the passage (still considering the middle row of holes), the deflection of the coolant toward the suction side of the passage is reduced. At this point the passage vortex has already crossed the passage, so the effect is reduced, although the effect of the passage vortex is not mitigated.

Finally, with the three holes located along the suction side of the passage, the coolant traces are very weak. This is again a result of the passage vortex. Others have shown after the passage vortex crosses to the suction side of the passage, it wraps around the suction leg of the horseshoe vortex and lifts off the platform near the trailing edge of

the blade. With the passage vortex lifting off the surface, the coolant is also lifted off the surface, minimizing the protection offered by the coolant.

Increasing the blowing ratio beyond 0.5 decreases the film cooling effectiveness on the platform. Similar to flat plate studies, increasing the momentum of the jets, causes the film coolant to blow off the surface. When the coolant lifts off the surface, the platform is left unprotected. Although increasing the blowing ratio, decreases the film cooling effectiveness, the coolant traces are also altered. With the increased momentum, the coolant is more closely follows the injection angle of the holes; although the true injection angle is never fully realized.

Figure 52 also shows the effect of freestream turbulence intensity on the discrete film cooling. However, there is no defining trend to characterize the effect of increased freestream turbulence. In other words, the film cooling effectiveness distributions obtained for both freestream turbulence levels are very comparable. On this latter half of the passage, the turbulence intensity is reduced (Tu = 5%). The effect is further reduced by the film cooling holes placed at the compound angle to the mainstream flow and the strong effect of the passage induced secondary flow. Figure 53 shows the laterally averaged effectiveness with the downstream discrete film cooling holes. This figure reiterates that no clear differences can be seen between the two freestream turbulence levels.

Finally the film cooling effectiveness is measured with combined seal injection and discrete film holes. With the freestream turbulence having only a marginal effect on the film cooling effectiveness, the effectiveness is presented without the turbulence grid,

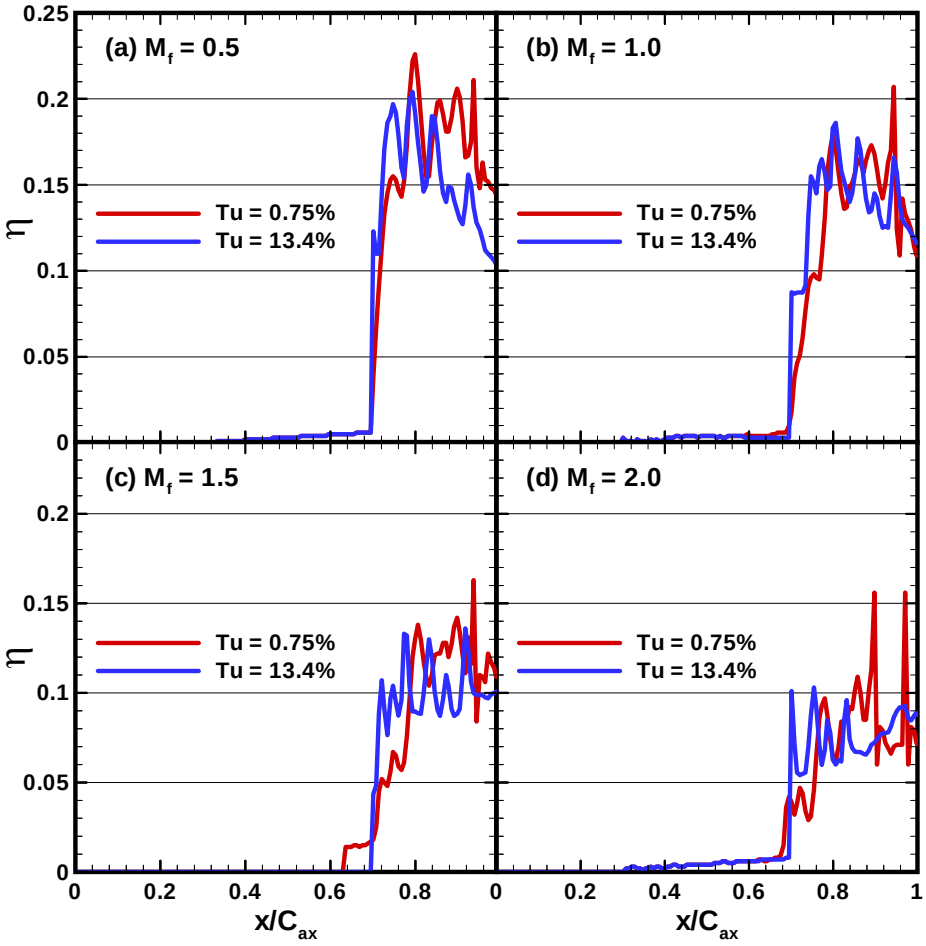


**Fig. 53 Laterally averaged film cooling effectiveness on the passage endwall with downstream discrete film cooling**

so the freestream turbulence intensity is 0.75%. Figure 54 shows the measured effectiveness with a seal injection rate of 1.0% and various blowing ratios from the discrete film holes. Figure 48(b) clearly shows a large area of the passage is left unprotected with only upstream injection, so the addition of the discrete holes should help alleviate this problem. All the trends observed for the upstream injection and the downstream film holes can be seen in these figures. The seal and holes flows are essentially independent of one another.

Although the holes adequately protect the downstream half of the passage, an area near the pressure side of the passage remains unprotected. One way to ensure this area is adequately protected is to increase the coolant flow rate from the seal. Figure 55 shows an increased seal flow of 2.0% combined with the discrete film holes. Now the entire passage is protected, but much of the downstream half of the passage is over protected. With this high flow rate of 2.0%, the downstream film cooling is not required, and therefore, this is wasted coolant. Figure 55(a) clearly shows the film accumulation due to the seal and hole coolant flows. Although this illustrates the power of the PSP measurement technique, it also clearly shows how the coolant is inefficiently used. Figure 55(a) also confirms the power of the PSP technique. The path of the coolant from the middle row of film holes nearly follows the streamlines through the passage. As stated earlier, increasing the flow rate of coolant through the seal can weaken the effect of the passage induced secondary flow. This is seen by the path of the coolant from the holes; the coolant is no longer directed from the pressure side to the suction side of the passage (as dominant passage vortex would dictate).

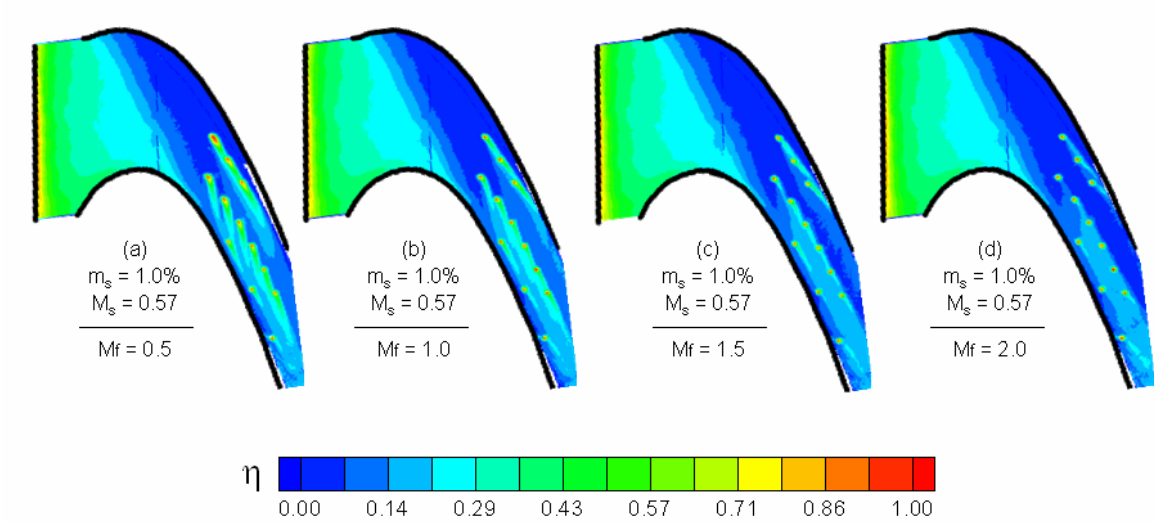


**Fig. 54 Film cooling effectiveness with combined seal cooling (1%) and downstream film cooling (Tu = 0.75%)**

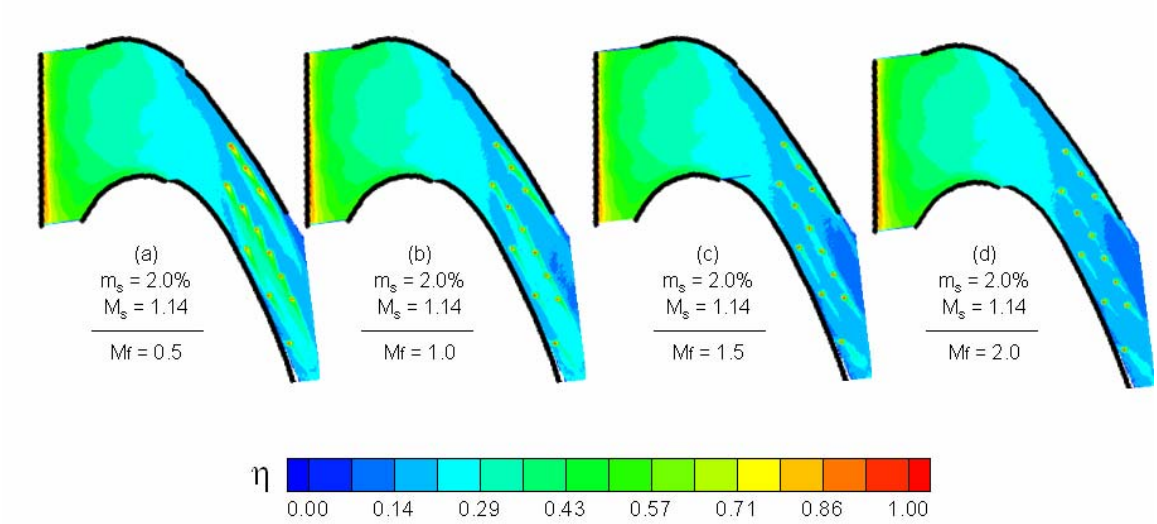


**Fig. 55 Film cooling effectiveness with combined seal cooling (2%) and downstream film cooling (Tu = 0.75%)**

The combined effect of the upstream injection combined with the discrete holes is shown by the laterally averaged effectiveness in Fig. 56. Beginning with the seal injection rate of 1.0%, from the reference case (only seal flow with $m_s$ = 1.0%), the effectiveness quickly drops into the passage. However, with the addition of the downstream discrete film cooling holes, the effectiveness increases dramatically with the additional cooling. With the seal injection of 2.0%, the effectiveness is obviously greater than with the injection of 1.0%. The film cooling effectiveness is elevated with the film cooling holes; however, the increase is not as significant as with the injection rate of 1.0%.

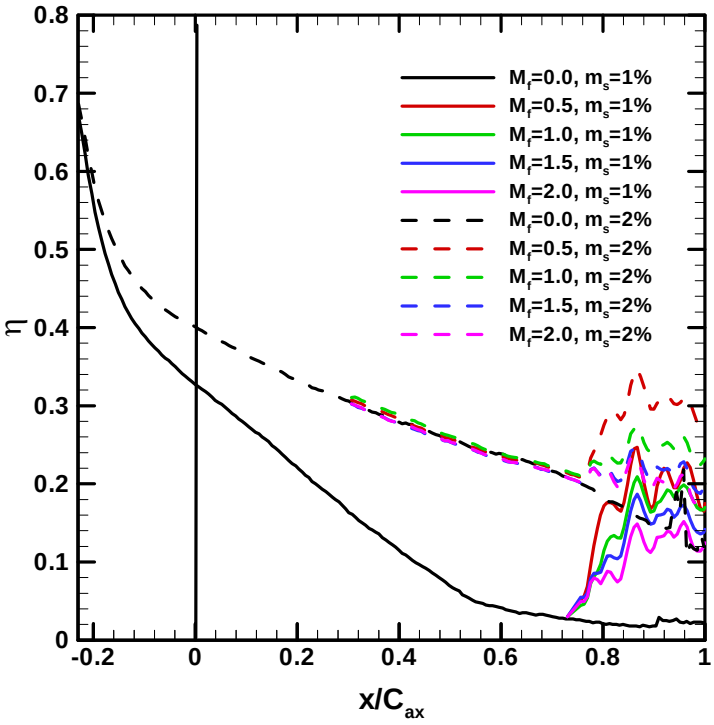


**Fig. 56 Laterally averaged film cooling effectiveness on the passage endwall with combined upstream seal injection and downstream discrete film cooling (Tu=0.75%)**

# MEASUREMENT OF THE EFFECT OF ROTATION IN TRAILING EDGE, INTERNAL COOLING PASSAGES

## *Effect of Rotation*

Heat transfer in rotating coolant passages is very different from that in stationary coolant passages. Both Coriolis and rotating buoyancy forces alter the flow and temperature profiles in the rotor coolant passages and affect their surface heat transfer coefficient distributions (Dutta and Han [49] and Wagner et al. [73]). It is very important to determine the local heat transfer distributions in the rotor coolant passages under typical engine cooling flow, coolant-to-blade temperature difference (buoyancy effect), and rotating conditions. Effects of coolant passage cross-section and orientation on rotating heat transfer are also important. As sketched in Fig. 57, the secondary flows in a two-pass channel are different for radial outflow and radial inflow passes. Since the direction of the Coriolis force is dependent on the direction of rotation and flow, the Coriolis force acts in different directions in the two-passes. For radial outward flow, the Coriolis force shifts the core flow towards the trailing wall. If both the trailing and leading walls are symmetrically heated, then the faster moving coolant near the trailing wall would be cooler (therefore heat transfer would be enhanced) than the slower moving coolant near the leading wall (i.e., heat transfer would be decreased). Rotational buoyancy is caused by a strong centrifugal force that pushes cooler heavier fluid away from the center of rotation. In the first channel rotational buoyancy affects the flow in a similar fashion as the Coriolis force and causes a further increase in flow and heat

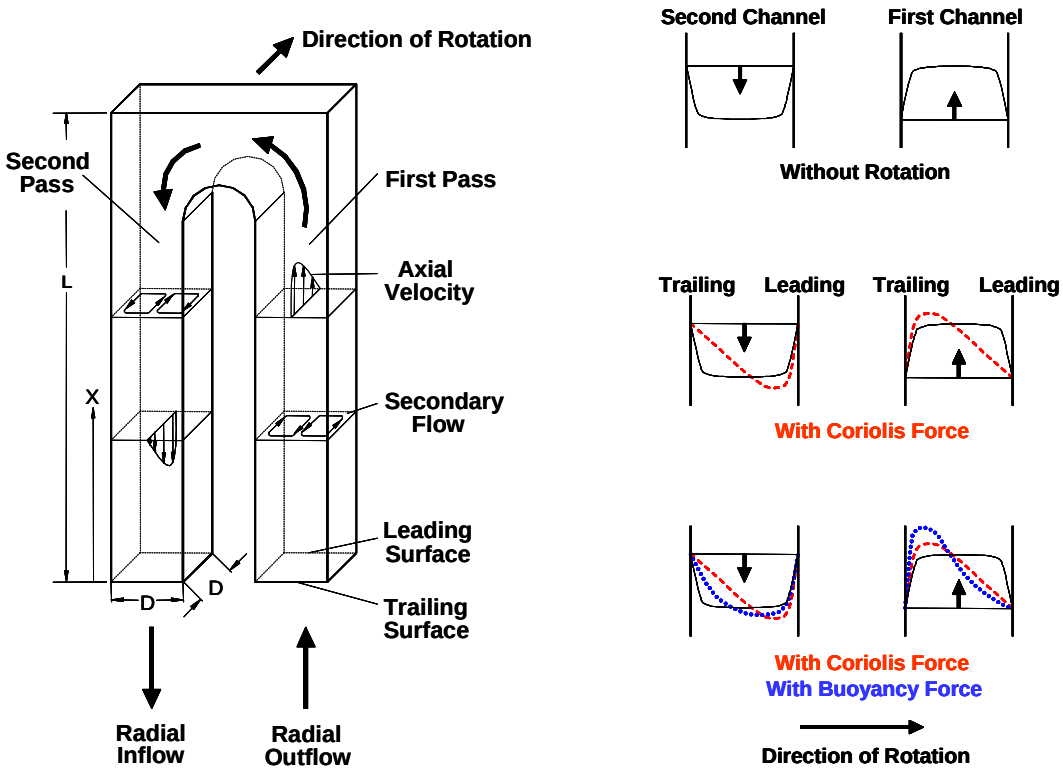


**Fig. 57 Effect of rotation on coolant flow through a two-pass cooling channel**

transfer near the trailing wall of the first channel; whereas, the Coriolis force favors the leading side of the second channel. The rotational buoyancy in the second channel tries to make the flow distribution more uniform in the duct.

### *Experimental Facility for Rotating Heat Transfer*

The experimental rotating test rig used for this study is shown in Fig. 58. A gear attached to the shaft of a variable frequency motor is connected to a gear located at the base of a hollow shaft via a timing belt, so the variable frequency motor is used to rotate the hollow shaft. The hollow shaft extends from the base of the test rig to the work platform. A hollow rotating arm is attached orthogonal to the rotating shaft; the test section is inserted into this rotating arm. Thermocouple and heater wires are connected to a 100-channel slip ring assembly that is mounted to the rotating shaft. Power is supplied through the slip ring to the heaters using variable transformers. Cooling air is pumped to the test rig using a steady flow air compressor. The air flows through an ASME square-edge orifice meter, upward through the hollow rotating shaft, around a 90° bend, through two mesh screens, and into the rotating arm and test section. After flowing through the test section, the air is expelled to the atmosphere.

A 48-channel Scani-valve pressure transducer was fixed at the top of the slip ring to the rotating shaft. Flexible tubing from the Scani-valve runs through the hollow shaft to the base of the slip ring, where it exits the slip ring in the same locations as the slip ring lead wires. The tubing is then attached to the pressure taps of the test section. The

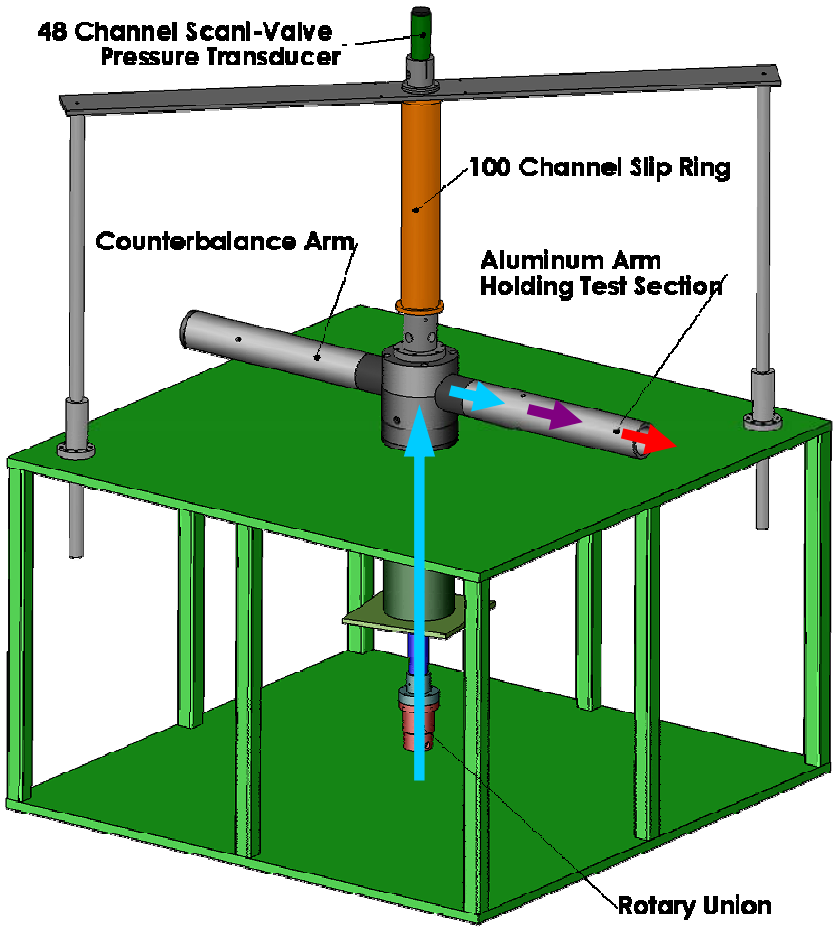


**Fig. 58 3D model of the rotating test facility**

signal of the pressure transducer is transmitted through the slip ring to the data acquisition system.

The test section is a one-pass rectangular channel. The ratio of mean rotating arm radius-to-channel hydraulic diameter ($R/D_h$) is 33.0 for the 4:1 channel. Likewise, the heated channel length-to-hydraulic diameter ratio ($L/D_h$) is 7.5. The air flows radially outward from the axis of rotation through the test section.

Figure 59 shows a schematic of the test section used in the present study. The test section consists of the leading, trailing, inner, and outer surfaces. The inner and outer surfaces each consist of six plates in the streamwise direction. The leading and trailing surfaces each consist of twelve plates. The cross-section of the test section contains two plates for the leading surface to capture the spanwise variation on the leading surface, two plates for the trailing surface (spanwise variation), one plate for the inner surface, and one plate for the outer surface. A total of thirty-six copper plates make-up the entire test section. Each plate is 0.9375 inch x 0.9375 inch (2.38 cm x 2.38 cm) and is surrounded by a 0.0625 inch (0.159 cm) strip of nylon to prevent conduction between the plates. This method provides a grid for analysis of the spanwise as well as the streamwise variation in the regionally averaged heat transfer coefficients. In order to maintain approximately the same circumferential wall temperature the power supplied to the heaters is varied. While maintaining the same temperature at two adjacent copper plates, the net heat flux can vary by 45%. Therefore, the nylon strip is effectively limiting the conduction between adjacent copper plates.

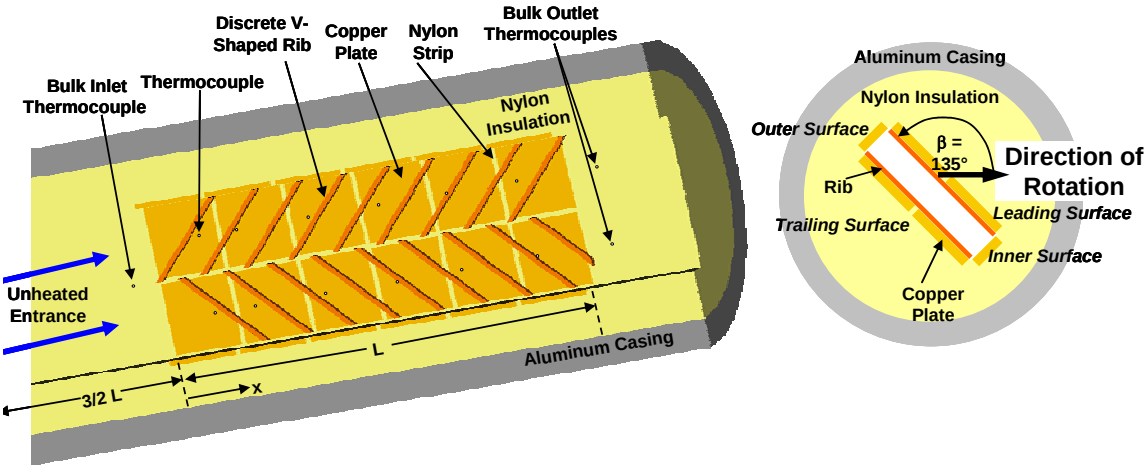


**Fig. 59 Model of a typical 4:1 test section**

Each 0.125 inch (0.318 cm) thick copper plate has a 0.0625 inch (0.159 cm) deep blind hole drilled in its backside. The temperature of each copper plate is measured using a 36 gauge, type T thermocouple. The thermocouple is secured in the blind hole using thermally conductive epoxy. With this setup, the thermocouple junction is located 0.0625 inch (0.159 cm) from the surface of the copper plate. The thermocouple output is monitored using commercially available software. The temperature data is displayed using the virtual instrument format, and the data is written to a data file specified by the user.

A nylon substrate serves as the support for the test section; each of the copper plates is mounted into this substrate. The nylon substrate forms a 3.5 inch (8.89 cm) diameter cylinder, and this test section is placed inside the aluminum, rotating arm of the test rig. Flexible heaters are installed beneath the leading and trailing surfaces, two for each surface. Thermal conducting paste is applied between the heater and copper plates to minimize contact resistance and promote heat transfer from the heater to the plates.

The outer and inner walls (or sidewalls) are smooth, and they are unheated. Static pressure taps are used to measure the pressure at the inlet and outlet of the heated portion of the test section. At the inlet, one pressure tap is located on the inner surface and one tap is located on the outer surface (the smooth walls), and two corresponding taps are located at the exit of the heated test section. Four channels of a 48-channel Scani-valve pressure transducer are used to measure the static pressure at each of the taps. The voltage output of the transducer is read using a multimeter. The Scani-valve

transducer was calibrated prior to the tests using an inclined manometer. The pressure measurements are taken under adiabatic conditions (test section is not heated).

The test section is oriented at 135° from the direction of rotation. The experiments are conducted at Reynolds numbers (based on the hydraulic diameter) of 10000, 20000, and 40000. In the heat transfer experiments, constant heat flux is supplied to the test section by each of the heaters. The maximum wall temperature is maintained approximately 38°C above the inlet coolant temperature to yield an inlet coolant-to-wall density ratio ($\Delta\rho/\rho$) of approximately 0.12 for all cases. The rotation speed remained constant at 550 rpm, resulting in a range of rotation number ($Ro$) from 0.038-0.150.

***Data Reduction***

This study investigates the regionally averaged heat transfer coefficient at various locations within the narrow rotating ducts with ribs. The heat transfer coefficient is determined by the net heat transferred from the heated plate, the surface area of the plate, the regionally averaged temperature of the plate, and the local bulk mean temperature in the channel. Therefore, the heat transfer coefficient is given as:

$$h = \frac{Q_{net} / A}{\left(T_w - T_{b,x}\right)} \tag{9}$$

The net heat transfer is calculated using the measured voltage and current supplied to each heater from the variac transformers multiplied by the area fraction of the heater exposed to the respective plate minus the external heat losses escaping from the test

section. The heat losses are predetermined by performing a heat loss calibration for both the rotational and stationary experiments. The heat loss calibration is performed by inserting insulation into the channel to eliminate natural convection. During the calibration, the heat transfer (in the form of power from the variac transformers) and wall temperature of each plate is measured; therefore, from the conservation of energy principle it is possible to know how much heat is being lost to the environment. At a Reynolds number of 10000, heat losses account for 17% of the heat put into the test section. However at the highest Reynolds number of 40000, just less than 8% of the heat input is lost by conduction through the test section.

The surface area used in this study is the projected surface area of the channel; in other words the surface area of a smooth channel (the area increase due to the ribs is neglected). The regionally averaged wall temperature ($T_w$) is directly measured using the thermocouple installed in the blind hole on the backside of each copper plate. Because the plates are made of copper, which has a high thermal conductivity, the temperature of each plate is assumed uniform. One thermocouple at the inlet and two thermocouples at the outlet of the test section measure the inlet and outlet bulk temperatures, respectively. Therefore, the bulk temperature at any location in the test section can be calculated using linear interpolation. The results presented from this study are based on the linear interpolation method. However, the local bulk temperature can also be calculated using the conservation of energy principle. For the present study, both methods compare very well. The energy balance equation is:

$$T_{bx} = T_{bi} + \sum_{i} \left( Q - Q_{loss} \right) / \dot{m} c_p \qquad x = 1, 2, ..., 6 \tag{10}$$

The Dittus-Boelter/McAdams [74] correlation for heating ($T_w > T_{bx}$) is used in this study to provide a basis of comparison. The Dittus-Boelter/McAdams correlation is used to calculate the Nusselt number for fully developed turbulent flow through a smooth stationary circular tube. Therefore, the Nusselt number ratio is given as:

$$\frac{\mathrm{Nu}}{\mathrm{Nu}_o} = \frac{hD_h}{k} \frac{1}{0.023\,\mathrm{Re}^{0.8}\,\mathrm{Pr}^{0.4}} \tag{11}$$

All air properties are taken based on the bulk air temperature with a Prandtl number (Pr) for air of 0.71.

The experimental uncertainty for the presented results was calculated using the method developed and published by Kline and McClintock [70]. The estimated uncertainty in the temperature measurements is 0.5°C for all cases. At the Reynolds number of 10000, the overall uncertainty in the Nusselt number ratio is approximately 15% of the presented values. At this lowest Reynolds number, a greater percentage of the heat input is lost. Due to the estimation of these heat losses, the experimental uncertainty increases. However, at the higher Reynolds numbers, the percent uncertainty of the individual measurements decreases and the percentage of heat losses decreases. Therefore, the overall uncertainty in the Nusselt number ratio decreases to approximately 7% of the calculated value at the highest Reynolds number of 40000.

The frictional losses in the cooling channel are determined by measuring the pressure drop from the inlet to the outlet of the heated test section. The friction factor is calculated using the measured inlet and outlet pressures as shown in Eq. 12.

$$f = \frac{P_i - P_e}{4\left(\frac{L}{D_h}\right)\left(\frac{1}{2}\rho V^2\right)} \tag{12}$$

The inlet pressure, $P_i$, is taken as the average of the two pressure measurements at the channel entrance, and the outlet pressure, $P_e$, is average of the two outlet pressure measurements.

The frictional losses can then be calculated by dividing the fiction factor by the turbulent friction factor in a smooth tube as given by the Blasius equation [75]. This ratio is shown in Eq. 13.

$$\frac{f}{f_o} = \frac{f}{0.079\,Re^{-1/4}} \tag{13}$$

The experimental uncertainty for the frictional losses was also calculated using the method developed by Kline and McClintock [70]. At the Reynolds number of 10000, where the most uncertainty exists in the measured quantities, the overall uncertainty in the friction factor ratio is approximately 16% of the presented values. However, at the higher Reynolds numbers, the percent uncertainty of the individual measurements decreases. Therefore, the overall uncertainty in the friction factor ratio decreases to approximately 6.5% of the calculated value at the highest Reynolds number of 40000.

Based on the heat transfer enhancement ($Nu/Nu_o$) and the frictional loss penalty ($f/f_o$), the thermal performance, $\eta$, of each rib configuration can be calculated. Equation 14 shows the thermal performance based on the constant pumping power condition as used by Han et al. [76].

$$\eta = \frac{\left( Nu / Nu_o \right)}{\left( f / f_o \right)^{1/3}} \tag{14}$$

# COMBINED EFFECT OF ROTATION AND ENTRANCE GEOMETRY ON INTERNAL, HEAT TRANSFER ENHANCEMENT

## *Channel Entrance Configurations*

Figure 60 shows the three entrance geometries investigated in this study. Figure 60(a) shows the case of fully developed flow. For the fully developed case the cross-section of the entrance section is identical to that of the heated test section, and the entrance duct is 11.25 hydraulic diameters in length. Figure 60(b) shows a channel in which the fluid is forced through a sudden contraction. As shown in this figure, the height of the entrance duct is three times greater than that of the heated test section. Therefore, the coolant is forced through the sudden contraction into the heated test section. Figure 60(c) shows the cross-section of a channel that contains a partial sudden contraction. In this case, the cross-section of the entrance duct is identical to the heated test section. However, the entrance duct does not allow the coolant to flow directly into the heated test section; the coolant is redirected just before entering the heated test section. As with the fully developed case, the entrance duct of the latter two cases is 11.25 hydraulic diameters long. The entry of the channel is altered using pieces of nylon, which can be moved to create various entry scenarios (only the entrances of the leading and trailing surfaces are altered to create the various entrances).

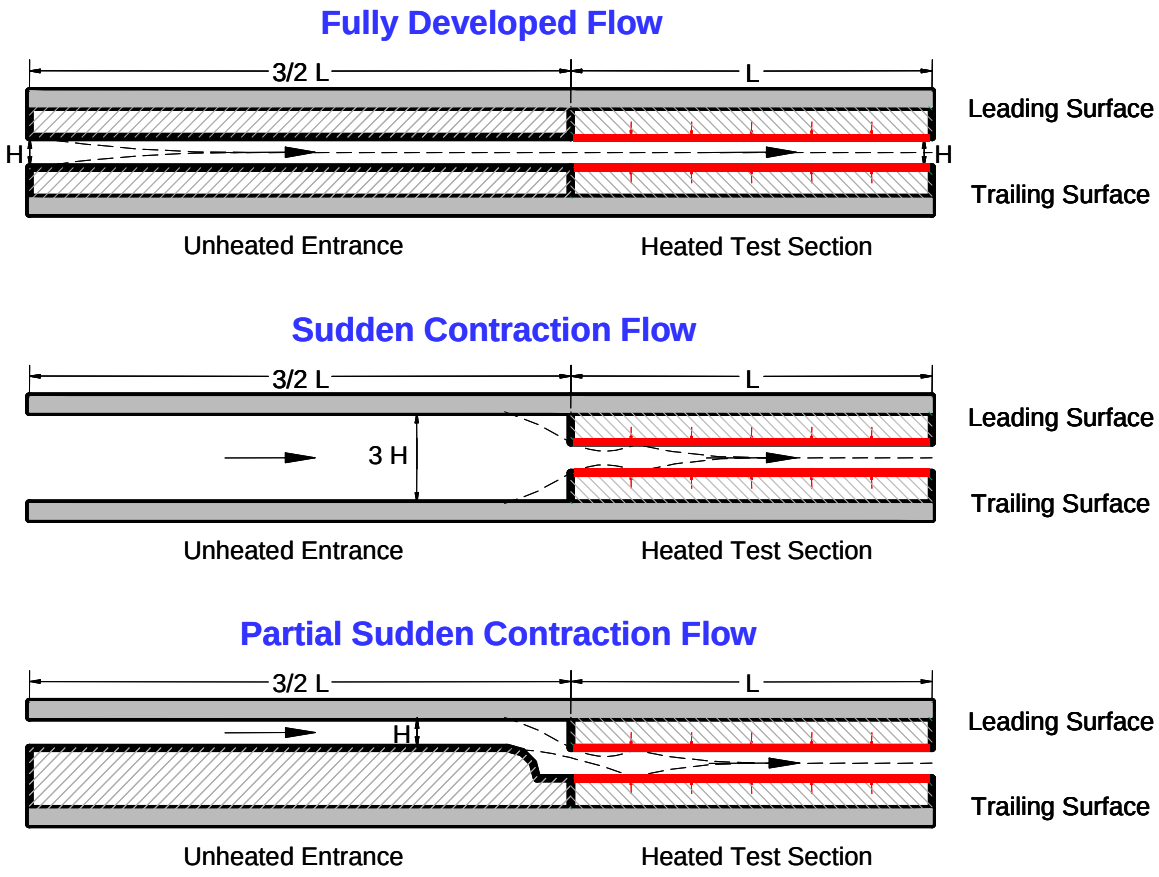


**Fig. 60 Cross-sectional view of the various entrance configurations**

***Secondary Flow Behavior***

Figure 61 shows conceptual views of the secondary flow behavior within the cooling channel. As shown in Fig. 61(a), the secondary flow induced by the 45° angled ribs, in the fully developed channel, moves parallel to the ribs from the outer surface to the inner surface and returns back to the outer surface. Thus, the angled ribs create two counter rotating vortices rotating parallel to the angled ribs in the cross-section of the channel. As the coolant travels along the rib, it gradually becomes warmer. Therefore, the heat transfer enhancement for the leading and trailing-outer surfaces is expected to be greater than the leading and trailing-inner surfaces.

The Coriolis and buoyancy forces, induced by the rotation, affect the flow through a rotating channel. Two counter-rotating vortices are created in a rotating channel, as shown in Fig. 61(b). The vortices are created as a result of the coolant being forced from the leading-inner corner to the trailing-outer corner. The trailing surfaces experience enhanced heat transfer as the coolant is forced to the trailing side of the channel, and the trailing-outer surface typically experiences the greatest enhancement. However, due to the rectangular channel and orientation angle, the leading surface should also experience heat transfer enhancement.

For the channel shown in Fig. 60(a), the flow is hydrodynamically developed when it enters the heated portion of the test section, and the dashed line shown in this figure represents the hydrodynamic boundary layer. Therefore, only the thermal boundary layer develops within the heated test section. However, for flow through a

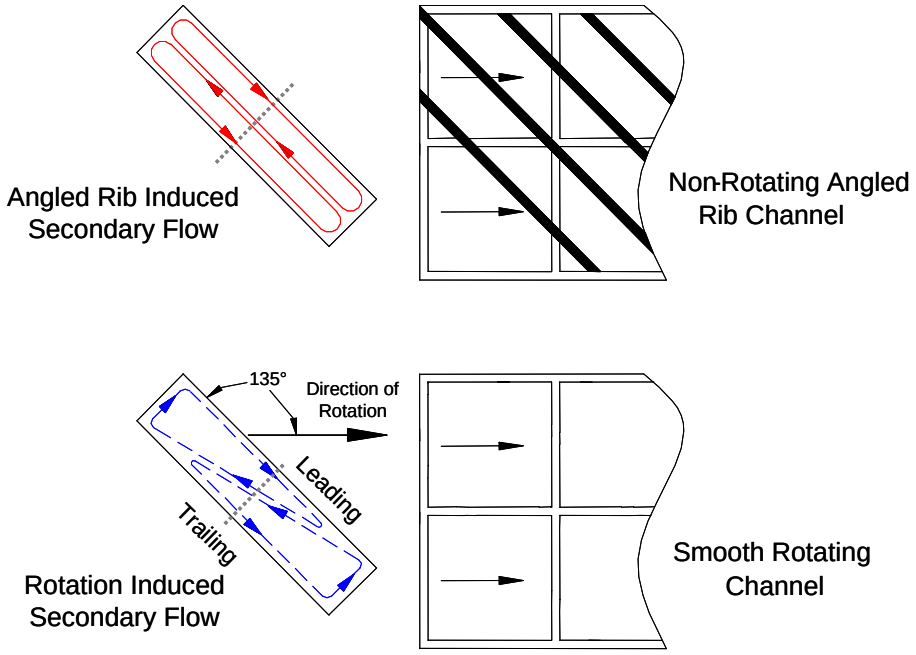


**Fig. 61 Flow conceptualization. (a) Secondary flow induced by 45° angled ribs and (b) Vortices induced by rotation in a narrow rectangular channel**

sudden contraction and flow through a partial sudden contraction, both the thermal and hydrodynamic boundary layers are developing in the heated test section.

As the coolant is forced through the sudden contraction, flow separation occurs at the entrance of the heated test section; this separation is associated with the vena contracta which occurs just downstream of the sharp entrance. Therefore, at the entrance of the heated test section, the turbulence intensity of the flow increases due to the area of separation and flow recirculation. With the increased turbulence, the heat transfer will also increase. Also associated with the flow separation and reattachment is development of the boundary layer. After the flow separates and reattaches past the vena contracta, the boundary layer develops and begins to grow. Therefore, the boundary layer at the beginning of this heated test section is much thinner than the boundary layer of the fully developed channel (boundary layer extends to the middle of the channel). The development of the hydrodynamic boundary layer is represented in Fig. 60(b) by the dashed line. The thinner boundary layer results in greater heat transfer from the channel walls. Downstream when the flow becomes developed, the heat transfer trends are expected to be similar to those of the fully developed flow.

As the coolant travels through the partial sudden contraction, areas of separation and recirculation form. The phenomenon occurring along the upper (leading) surface is similar to that of the sudden contraction. The flow separates as it passes the sharp entrance into the heated test section. Again, there is the area of recirculation associated with the vena contracta downstream of the entrance. On the trailing surface, the flow advances down a rounded step before entering the heated test section. The flow also

separates as it passes over the step. Therefore, on the trailing surface an area of flow separation and recirculation exists. As with the sudden contraction entrance geometry, the turbulence at the beginning of the heated test section is increased, and associated with the increased turbulence is an increase in the heat transferred from the channel walls. As with the flow through the sudden contraction, the boundary layer begins to develop and grow just inside the heated test section. In this developing region, the boundary layer is relatively thin (as represented by the dashed line in Fig. 60(c)), and there is more heat transferred from the walls.

Within the stationary channels, the turbulent mixing is increased by both the rib turbulators, as well as the various entrance geometries. Therefore, it is expected the varied entrance geometries will increase the heat transfer at the entrance of the channel. In the rotating channels with angled ribs, there is an increased turbulence due to the ribs, the entrance geometry, and rotation. Therefore, it is conjectured the effect of the various entrance geometries will be less significant in the rotating channel than in the stationary channel.

***Heat Transfer Enhancement***

Figure 62 contains the stationary Nusselt number ratio results for the smooth channel with varying entrance geometry. The solid lines represent the data for the fully developed flow, and the dashed lines represent the data for flow through the sudden contraction or partial sudden contraction. Both non-rotating and rotating experiments

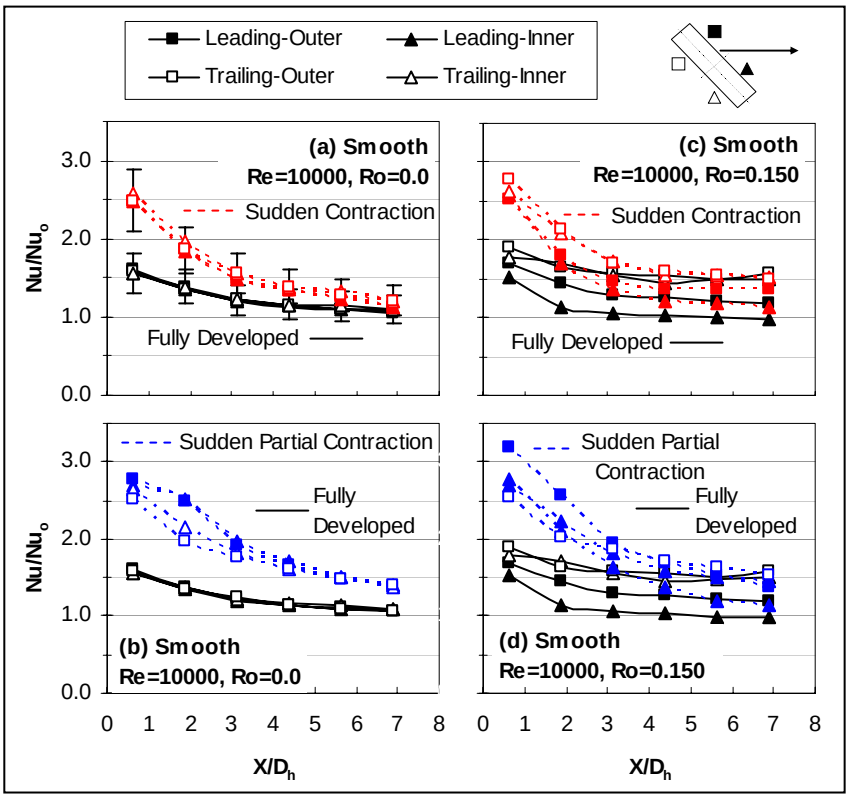


**Fig. 62 Nusselt number ratios in smooth channels with Re = 10000**

are shown for Re=10000, with Ro=0.150 for the rotating channels. Figures 62(a) and 62(b) show the Nusselt number ratio for stationary channels, and Figs. 62(c) and 62(d) show the results for the rotation channels.

Figure 62(a) shows the heat transfer enhancement for the fully developed entrance geometry and the sudden contraction entrance geometry applied to the smooth channel. As shown by the solid lines in the figure, the Nusselt number ratio for the smooth channel with the fully developed entrance approaches a thermally developed value of unity. The values at the entrance of the channel are elevated above the value of one due to the development of the thermal boundary layer. The dashed lines in Fig. 6(a) show the Nusselt number ratios for flow through the sudden contraction. As clearly seen in this figure, the ratios at the entrance of the heated test section are elevated above those within the fully developed channel. Due to the contraction, both the hydrodynamic and thermal boundary layers are developing at the beginning of this channel. With this relatively thin boundary layer, the heat transfer is enhanced above that in the fully developed channel. At the Reynolds numbers greater than 10000, the entrance condition has less of an impact on the downstream heat transfer enhancement.

Figure 62(b) compares the heat transfer enhancement of the fully developed flow to that of flow through a partial sudden contraction. Similar to the sudden contraction, at the entrance of the channel, the Nusselt number ratios are elevated above those of fully developed flow. The heat transfer coefficients are also elevated above those of the sudden contraction geometry (Fig. 62(a)). However, for this geometry all surfaces do not exhibit the same level enhancement; at the entrance of the channel, the leading

surfaces are enhanced more than the trailing surfaces. This is due to the nonsymmetrical entrance condition (as shown in Fig. 60). With the high Nusselt number ratios at the entrance, the Nusselt number ratios for flow through this partial sudden contraction do not reach the fully developed value of unity. As the Reynolds number increases, the trends begin to approach one, but they remain greater than one. Therefore, this nonsymmetrical partial sudden contraction has a more significant impact on the heat transfer throughout the entire channel than the sudden contraction entrance.

As shown in Fig. 62(c), the general trends of the data for the smooth, rotating channel are the same as for the stationary cases. However, there exists spanwise variation, and as one may anticipate, the surface that undergoes the least enhancement is the leading-inner surface. As explained previously, this is due to the rotation-induced vortices which shift the coolant away from the leading-inner corner to the trailing-outer corner of the channel. As the rotation number decreases (Reynolds number increases), rotation has less of an effect on the coolant flow through the channel. At the highest Reynolds number of 40000 ($Ro$ = 0.038), the spanwise variation is very small, and the flow in the smooth rotating channel exhibits the same trend as the flow in the smooth stationary channel: a gradual decrease until the fully developed value of unity is achieved.

Also shown in Fig. 62(c) are the Nusselt number ratios for the flow through the sudden contraction. As with the stationary channel, the Nusselt number ratio of the first point for all surfaces is elevated above the fully developed values. Spanwise variation is

also present in this channel; however, it is clear the amount of variation is less than that in the fully developed channel.

Figure 62(d) shows a similar trend as Fig. 62(c). The heat transfer from the channel walls is elevated above the enhancement created with the fully developed geometry. From the stationary results it was shown that the leading surfaces underwent more enhancement than the trailing surfaces. This is trend is also apparent at the entrance of these rotating channels. As one moves downstream, the effect of rotation is more pronounced as there is more enhancement from the trailing surfaces than the leading surfaces.

Figure 63 compares data from the current study to that of Boelter et al. [64] as presented by Kays and Crawford [63]. This data from Kays and Crawford [63] corresponds to a Reynolds number of 50000, and from this present study, a Reynolds number of 40000 is shown. The results from the present study for the fully developed, sudden contraction, and partial sudden contraction are compared to flow through a long entrance, sharp entrance, and rounded bend, respectively. The Nusselt number ratios for fully developed flow follow the results from the previous study along the entire length of the channel. For flow through a sudden contraction the Nusselt number ratio is slightly less than ratios for flow through the sharp entrance. Because the present study focuses on the regionally averaged heat transfer, the detailed distribution of the increase then decrease within in the channel is not captured. Overall, throughout the channel, the present study follows the same trend as the well-known literature. Similar to the sudden

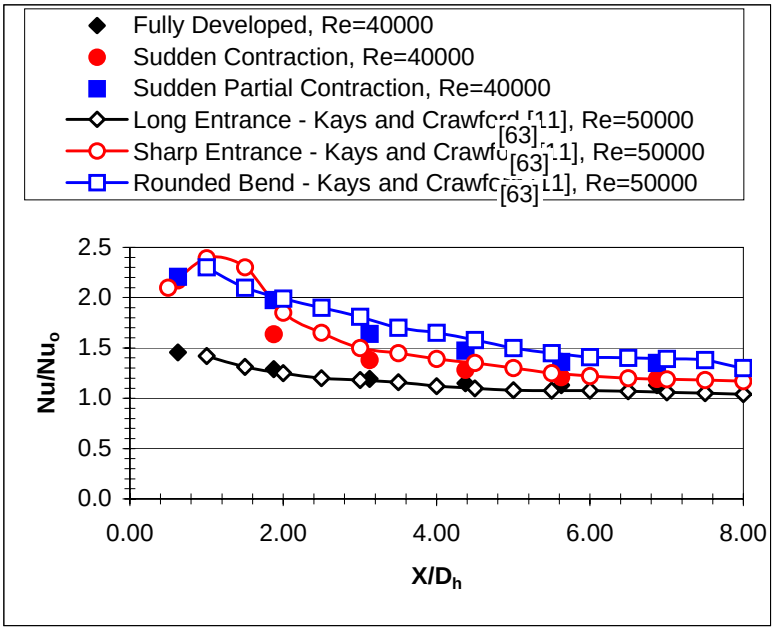


**Fig. 63 Nusselt number ratio comparison of smooth channels with varied entrances**

contraction, the values for the sudden partial contraction are less than those of the rounded bend. However, the values are comparable to those of the accepted literature.

Figure 64 contains the stationary Nusselt number ratio results for the channels with angled ribs and varying entrance geometry. Figure 64(a) shows the heat transfer enhancement for the fully developed entrance geometry and the sudden contraction entrance geometry. For the present angled rib configuration, the leading-outer and trailing-outer surfaces undergo significantly higher heat transfer enhancement than the leading and trailing-inner surfaces. With this 45° angled rib geometry, the first interaction between the rib and the coolant occurs on the leading and trailing-outer surfaces, near the corner of the channel. When the coolant contacts the rib, the hydrodynamic boundary layer of the fluid is tripped, and the coolant near the surface is forced to traverse along the length of the rib from the outer surface toward the inner surface. As the coolant follows the rib, the secondary fluid velocity is decreasing. More heat is convected away from the channel along the leading and trailing-outer walls due to the increased secondary flow velocity of the coolant and relatively thin boundary layer. As the velocity decreases (and the boundary layer grows thicker), less heat is convected from the surface, and thus the leading and trailing-inner surfaces undergo less heat transfer enhancement than the leading and trailing-outer surfaces. Also, as the coolant travels along the length of the rib turbulators, there is a rise in the coolant temperature. Therefore, the heat transfer enhancement is greatest along the leading and trailing-outer surfaces where the coolant temperature is the lowest. As the coolant temperature rises

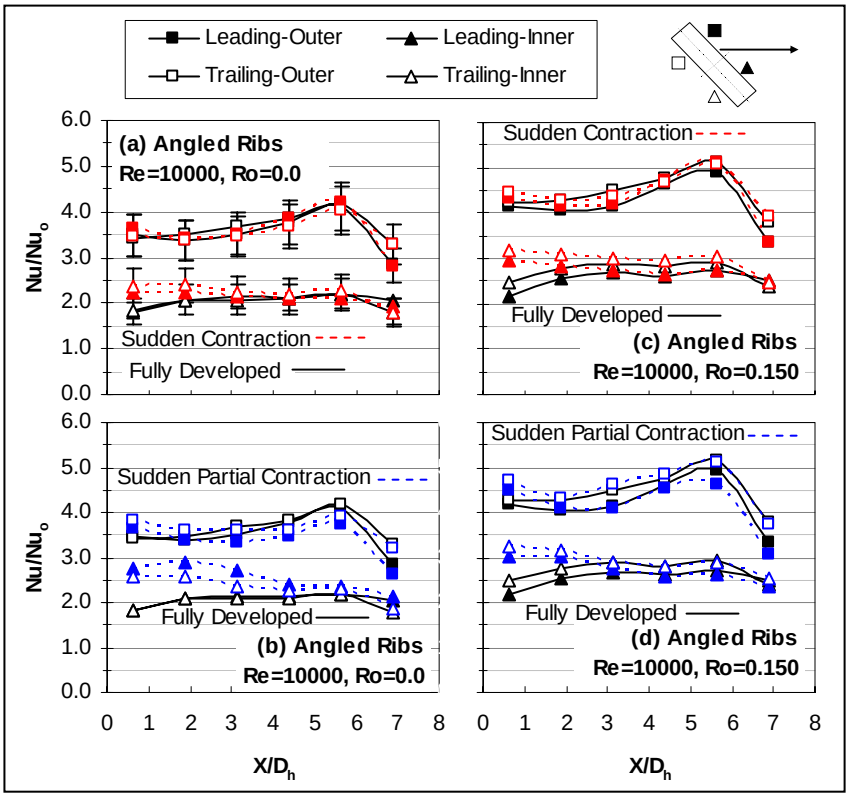


**Fig. 64 Nusselt number ratios in angled rib channels with Re = 10000**

along the length of the rib, less heat is transferred from the hot leading and trailing-inner surfaces to the relatively warm coolant.

The Nusselt number ratios continue to increase until approximately 4.5 hydraulic diameters downstream of the entrance, as the rib induced secondary flow gains strength. As the Reynolds number increases, the effectiveness of the ribs decreases. From the Dittus-Boelter correlation, the Nusselt number ($Nu_o$) increases as the Reynolds number increases, and this results in a decrease in the Nusselt number ratio. Also as the Reynolds number increases, the Nusselt number ratio difference between the outer surfaces (leading and trailing) and inner surfaces (leading and trailing) decreases.

As also shown in Fig. 64(a), fully developed flow and flow through a sudden contraction undergo relatively the same amount of heat transfer enhancement for the majority of the channel. The difference in the two channels occurs at the beginning of the channel. As with the smooth stationary channel, the Nusselt number ratios of the sudden contraction begin to converge to the ratios of the fully developed channel. For this angled rib case, the values of the sudden contraction converge to the fully developed values at approximately 2 hydraulic diameters; in the smooth channel, at least 5 hydraulic diameters are required for sudden contraction values to meet the fully developed values.

Figure 64(b) shows a similar trend as Fig. 64(a). However, the entry length for flow through a sudden partial contraction is much longer than flow through a sudden contraction. As shown in Fig. 64(b) the flow through the partial sudden contraction requires almost two-thirds of the channel to reach the Nusselt number ratio of the fully

developed flow (leading-inner and trailing-inner surfaces); this is unlike the smooth channel, where the ratios of the partial sudden contraction never decrease to the fully developed values. In addition, the heat transfer enhancement in the entrance of the channel is increased by as much as 52% (on the leading and trailing-inner surfaces) when compared to the fully developed channel. As the Reynolds number increases the effect of the entrance geometry decreases. With the increasing Reynolds number, the flow becomes more turbulent, therefore the additional effect created by the entrance geometry has less of an impact on the flow.

Figures 64(c) and 64(d) show the rotational Nusselt number ratio results for the channels with angled ribs and varying entrance geometry. As shown in Fig. 64(c), the heat transfer distributions in the rotating channel with fully developed flow are similar to those of the stationary channel (Fig. 64(a)). When the Nusselt number ratios are compared to those of the stationary channel (Fig. 64(a)), it can be seen that all surfaces in the rotating channel undergo heat transfer enhancement. As shown in Fig. 61, the vortices induced by rotation circulate in the same direction as those induced by the angled ribs. Therefore, rotation strengthens the secondary flow, and thus all surfaces experience heat transfer enhancement when compared to the stationary channel. As the Reynolds number increases, rotation number decreases, the heat transfer enhancement decreases, and there is less variation between the surfaces.

Also shown in Fig. 64(c) are the Nusselt number ratios for the flow through the sudden contraction. The values for flow through the contraction are slightly elevated above the ratios for the fully developed flow. The ribs induce counter rotating vortices

which increase the mixing of the coolant. Rotation also induces counter rotating vortices, which strengthen the rib-induced vortices, and more mixing occurs. Therefore, the effect of any additional mixing introduced by the varied entrance geometry has a decreased effect on the heat transfer enhancement in the rotating channel.

Figure 64(d) shows a similar trend as Fig. 64(b). The heat transfer from the channel walls is elevated above the enhancement created with the fully developed geometry. However, the difference between the fully developed flow and the flow through a partial sudden contraction is less in the rotating channel than in the stationary channel. In the rotating channel, the maximum variation is 40% along the leading and trailing-inner surfaces, compared to a difference of 52% from the stationary channel. Again, rotation induces more turbulent mixing in the channel, so the additional turbulence created by the entrance geometry has less of an effect in the rotating channel.

Figure 65 shows the channel-averaged Nusselt number ratios for the smooth and angled rib stationary channels with the given entrance geometries. This figure clearly shows for the smooth channels, the greatest channel enhancement occurs in the channel with the partial sudden contraction entrance, and this is followed by the sudden contraction entrance. The fully developed values are elevated above the ratio of one due to the entrance region of the channel where the thermal boundary is developing. Although the channels with the sudden contraction and partial sudden contraction approach values of one (Figs. 62(a) and 62(b)), the ratios at the entrance of these channels are much greater than those for the fully developed channel. Therefore, the averages are significantly greater than the fully developed channel.

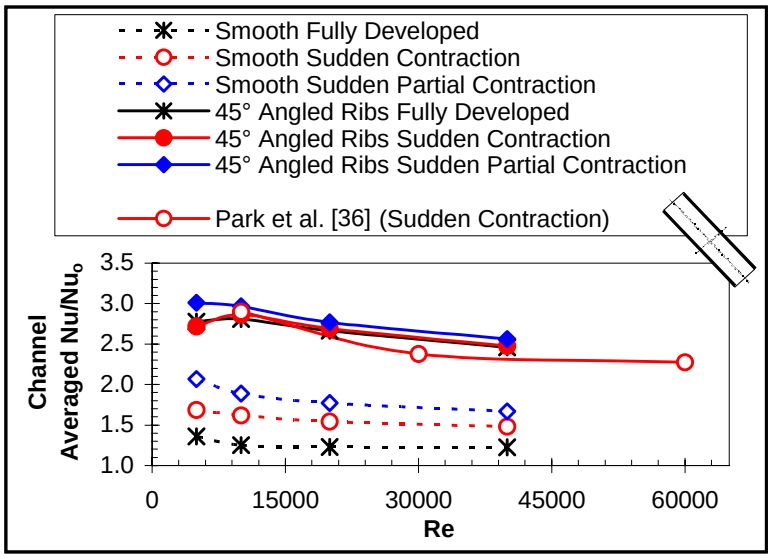


**Fig. 65 Channel averaged Nusselt number ratio in stationary cases**

As also shown in this figure, over the specified range of Reynolds numbers, the angled rib channel with the partial sudden contraction experiences greater heat transfer enhancement than the other ribbed channels. As the Reynolds number increases, the difference between the three geometries decreases. At a Reynolds number of 5000, the difference between the partial sudden contraction and the fully developed case is approximately 9%, and at the Reynolds number of 40000, the difference is only 4%.

Figure 65 also compares the stationary results of the present study to those of the previous study by Park et al. [36]. This previous study involved flow through an abrupt contraction with various rib configurations. The curve shown in this figure is for 45° angled ribs with a height-to-hydraulic diameter ratio ($e/D_h$) of 0.078 and a pitch-to-rib ratio ($P/e$) of 10, and the channel aspect ratio is 4:1. At the lower Reynolds numbers, almost no difference exists between the present and previous studies (less than 1% difference). However, as a Reynolds number increases, the trends of the two studies show variation. Although the present study does not directly involve a Reynolds number of 30000, the data trends show a variation of approximately 8% between the present and previous studies (which is within the experimental uncertainties of the two investigations). Again, from the data trends, as the Reynolds numbers continue to increase past 30000, the variation between the two studies decreases. Therefore, the stationary results of the present study are comparable to previous studies involving similar channel geometry.

Figure 66 shows the streamwise-averaged Nusselt number ratios in the smooth channel for fully developed flow, flow through a sudden contraction, and flow through a

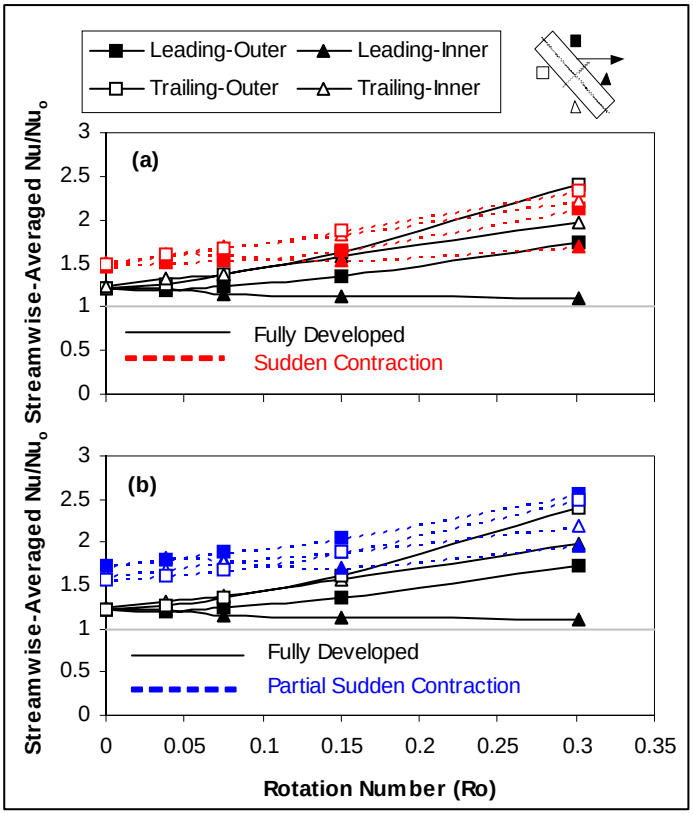


**Fig. 66 Streamwise averaged Nusselt number ratios in smooth channels**

sudden partial contraction. The solid lines represent fully developed flow, and the dashed lines represent flow through a sudden contraction and flow through a sudden partial contraction in Figs. 66(a) and 66(b), respectively. The results shown in Fig. 66(a) clearly indicate the coolant is being forced away from the leading-inner surface toward the trailing-outer surface. Due to the channel orientation and aspect ratio, the trailing-outer, trailing-inner, and leading-outer surfaces experience heat transfer enhancement and the leading-inner surface experiences a declination in the heat transfer with the increasing effect of rotation. The spanwise variation is also clearly seen in this figure. As the rotation number continues to increase the separation between the surfaces increases. The greatest enhancement due to rotation occurs on the trailing-outer surface, followed by the trailing-inner, and leading-outer, respectively.

Figure 66(a) also shows the difference between the fully developed flow and the flow through a sudden contraction. At the lower rotation numbers, the entrance condition is the dominant factor in determining the level of heat transfer enhancement; all surfaces in the channel with the contraction are greater than those of the fully developed channel. However, as the rotation number increases, the surfaces in the fully developed channel are affected more than the surfaces in the channel with the contraction. As with the fully developed channel, all surfaces undergo enhancement with the addition of rotation, but the enhancement due to rotation is less in the channel in the sudden contraction than the fully developed channel.

Figure 66(b) shows interesting trends for enhancement in the channel with the partial sudden contraction. Again, at low rotation numbers, the entrance condition is the

primary factor influencing the level of enhancement. At the low rotation numbers, the greater enhancement of the leading surfaces is clearly seen. However, as the rotation number increases, the effect of rotation begins competing with the effect of the entrance geometry. The leading-inner surface experiences the least enhancement at the highest rotation number. The effect of the entrance does not totally diminish at the higher rotation numbers, and this is seen with the leading-outer surface experiencing the greatest enhancement.

Figure 67 shows the streamwise-averaged Nusselt number ratios in ribbed channels with fully developed flow, as well as flow through a sudden contraction and flow through a sudden partial contraction, in Figures 67(a) and 67(b), respectively. As shown in Fig. 67(a), all surfaces in the rib channel with a fully developed entrance experience heat transfer enhancement with rotation. As the rotation number increases (Reynolds number decreases), the variation between the leading outer and trailing outer surfaces increases, and the same is true for the leading and trailing inner surfaces. Due to the nature of the rotation-induced vortices, the trailing-outer surface undergoes greater heat transfer enhancement than the leading-outer surface because the vortices are forcing the coolant from the leading-inner surface toward the trailing-outer surface. Likewise the trailing-inner surface experiences greater enhancement than the leading-inner surface. Figure 67(a) also shows there is little difference between the fully developed flow and the flow through a sudden contraction. The trailing surfaces of the channel with the sudden contraction undergo more heat transfer enhancement than the trailing surfaces of

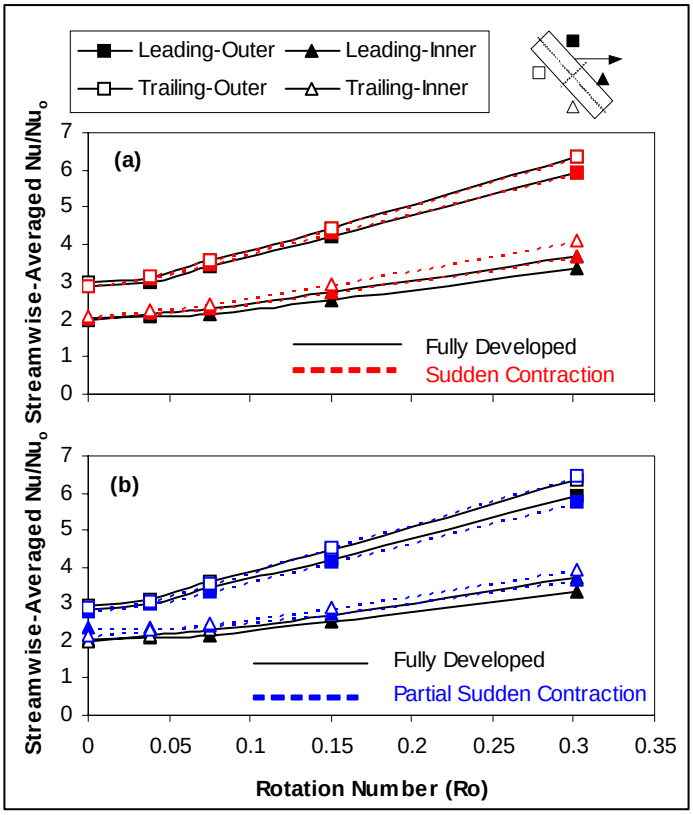


**Fig. 67 Streamwise averaged Nusselt number ratios in angled rib channels**

the fully developed channel. Figure 67(b) shows similar trends for flow through a partial sudden contraction.

Figure 68 shows the channel-averaged Nusselt number ratios for both the rotating and non-rotating channels with the various entrance geometries. This figure clearly shows the entrance geometry has a more profound effect on the heat transfer in the smooth channels than the ribbed channels. For both rotating and non-rotating channels, there is a clear distinction between the partial sudden contraction, sudden contraction, and fully developed values. For the rotating channels, the increasing Reynolds number corresponds to a decreasing rotation number. In this figure, the effect of rotation is clearly seen at the given Reynolds numbers. At the lowest Reynolds number of 5000, the greatest variation exists between the stationary and rotating results. In the ribbed channel, at this highest rotation number, the rotating channel results can be up to 1.75 times greater than the stationary results. However, at the highest Reynolds number (lowest rotation number) the enhancement within the rotating channel is only 1.10 times greater than the stationary channel. It can also be seen in this figure that the flows through the sudden contraction and partial sudden contraction experience greater heat transfer enhancement than the fully developed flow.

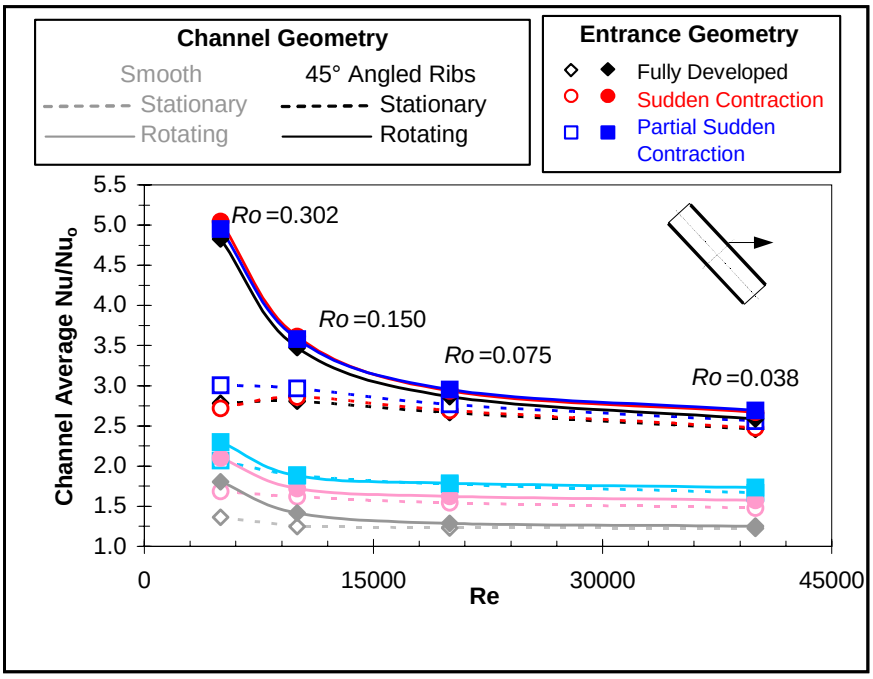


**Fig. 68 Channel averaged Nusselt number ratios in rotating and stationary channels with varying entrances**

# THERMAL PERFORMANCE OF HIGH PERFORMANCE RIB TURBULATORS IN TRAILING EDGE COOLING PASSAGES

## *Rib Configurations and Rib Induced Secondary Flows*

The six rib configurations investigated in this study are shown in Fig. 69. The geometry of the six rib configurations of the present study is similar. The ribs for each case are parallel; i.e. the ribs on the leading surface are aligned with the ribs on the trailing surface. In each case, the ribs are oriented at 45° to the mainstream flow. One-sixteenth inch square ribs are used in all cases with a pitch-to-rib height ($P/e$) of 10 and a rib height-to-hydraulic diameter ratio ($e/D_h$) of 0.078. The ribs are made of brass, and they are glued to the copper plates of the leading and trailing surfaces. The thickness of the glue is less than 0.01 cm and creates negligible thermal resistance between the ribs and the copper plates.

Figure 70 shows conceptual views of the rib induced secondary flow within the cooling channels with angled ribs (70(a)), V-shaped ribs (70 (b)), and W-shaped ribs (70 (c)). The secondary flow induced by angled ribs and V-shaped ribs has been verified by the numerical predictions of Al-Qahtani et al. [77] and Su et al. [78], respectively. As shown in Fig. 69(a), the secondary flow induced by the 45° angled ribs moves parallel to the ribs from the outer surface to the inner surface and returns back to the outer surface. Thus, the angled ribs create two counter rotating vortices rotating parallel to the angled ribs in the cross-section of the channel. As the coolant travels along the rib, it gradually becomes warmer and the boundary layer continues to grow thicker. Therefore,

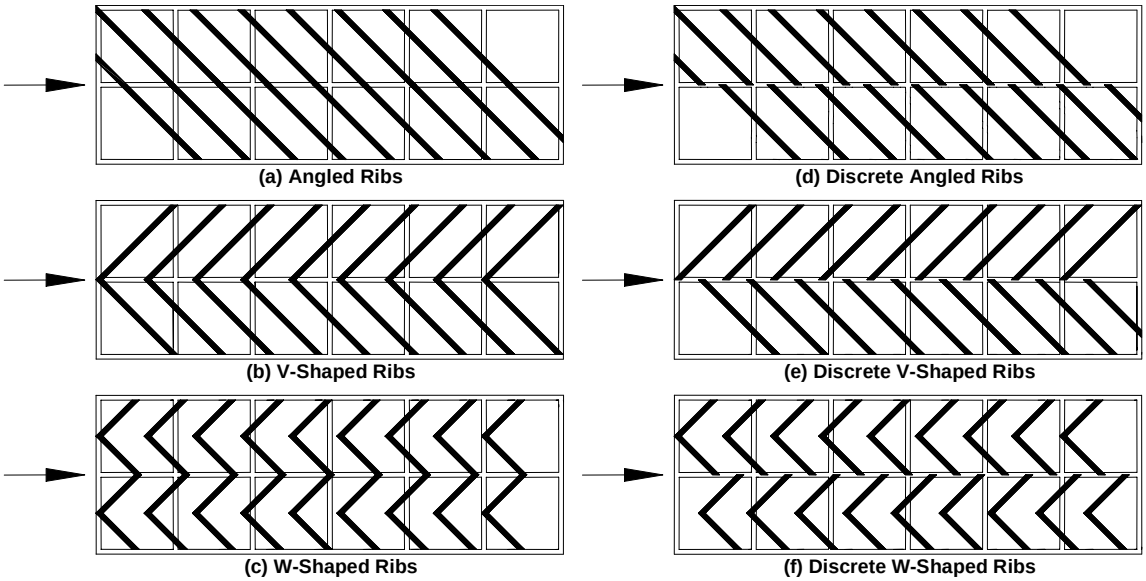


**Fig. 69 Top view of six high performance rib configurations**

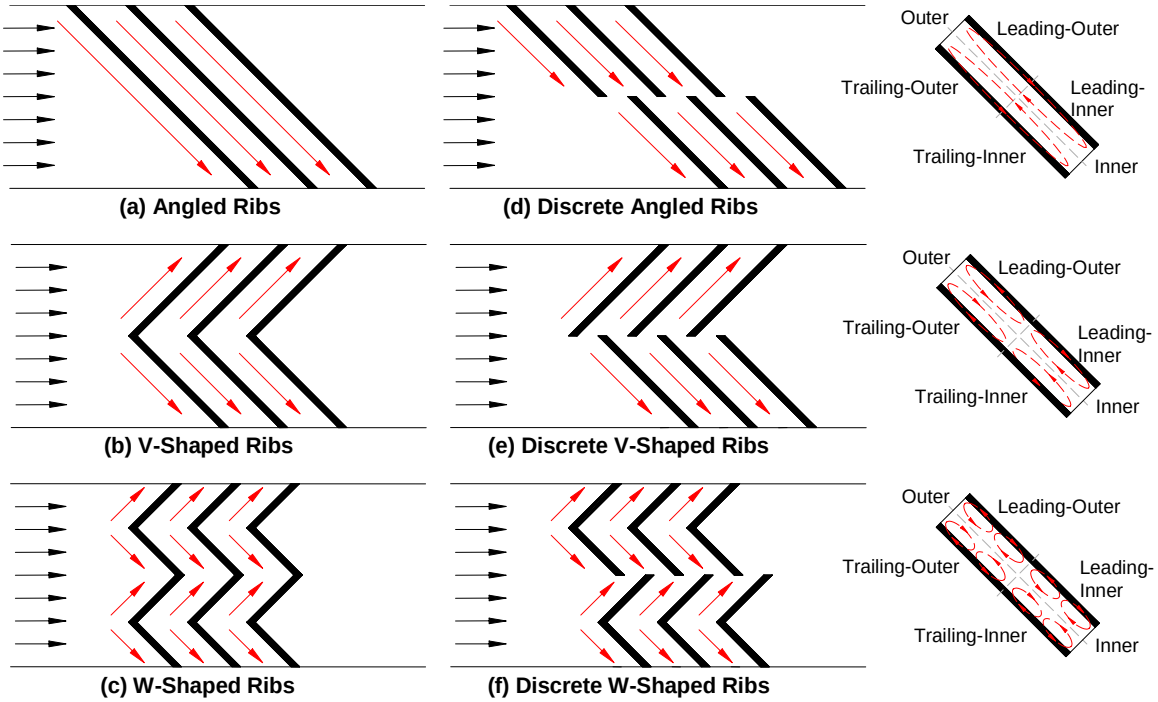


**Fig. 70 Rib induced secondary flow**

the heat transfer enhancement for the leading and trailing-outer surfaces is expected to be greater than the leading and trailing-inner surfaces (enhancement is much greater on the upstream portion of the rib than the downstream portion).

As shown in Fig. 70(b), the secondary flow induced by the V-shaped ribs creates four vortices. Near the wall, the coolant splits into two streams, each stream following the V away from the center of the channel to the sidewalls. The coolant is forced to circulate to the center of the channel after impinging on the sidewalls. Therefore, two vortices are created on the leading surface, and two vortices are created on the trailing surface. Because the V-shaped ribs are symmetrical about the center of the channel, it is expected the leading-inner, leading-outer, trailing-inner, and trailing-outer surfaces will all experience the same level of heat transfer enhancement (unlike the cooling channel with angled ribs). The rib induced flow of the W-shaped ribs is shown in Fig. 70(c). Conceptually it is shown that eight vortices are created in the cooling channel. These W-shaped ribs are essentially two V-shaped ribs joined at the center of the channel. As with the V-shaped ribs, the W-shaped ribs are expected to produce uniform spanwise heat transfer.

The rib induced flow of the discrete rib configurations is expected to be similar to that induced by the complete rib configurations (Figs. 70(d), 70(e), and 70(f)). The coolant near the wall will follow the rib resulting in the formation of counter rotating vortices as the coolant impinges on the sidewalls. The primary difference in the secondary flow behavior will occur near the centerline of the channel. As Ekkad and Han [41] showed with detailed liquid crystal measurements, the broken ribs create

serpentine secondary flows. This flow behavior results in the highest heat transfer occurring immediately downstream of the rib.

In the discrete angled rib channel, the discrete ribs will result in the creation of a second set of vortices (on the leading and trailing inner surfaces). This will also result in the redevelopment of the boundary layer on the inner surfaces. This thin boundary layer will result in much higher heat transfer enhancement when compared to the complete angled ribs.

***Thermal Performance of Rib Configurations***

Figures 71 and 72 contain a sample of the regionally averaged Nusselt number ratio results for the six rib configurations. Each figure contains results for the six rib configurations at Re=20000. For the rotating cases, this Reynolds number corresponds to Ro=0.075.

Figure 71(a) shows the regionally averaged heat transfer distributions in the non-rotating channel with angled ribs. It can be seen that the heat transfer enhancement along the leading-outer and trailing-outer surfaces is significantly higher than the enhancement along the leading-inner and trailing-inner surfaces. The ribs are angled, so the coolant is forced from the outer surface to the inner surface (see Fig. 70(a)). Therefore, the leading edge of the rib undergoes more enhancement, and as the coolant continues along the rib, the enhancement decreases as the boundary layer thickens. Moving in the streamwise direction, the Nusselt number ratio gradually increases as the rib induced vortices are gaining strength. As the Reynolds number increases, the

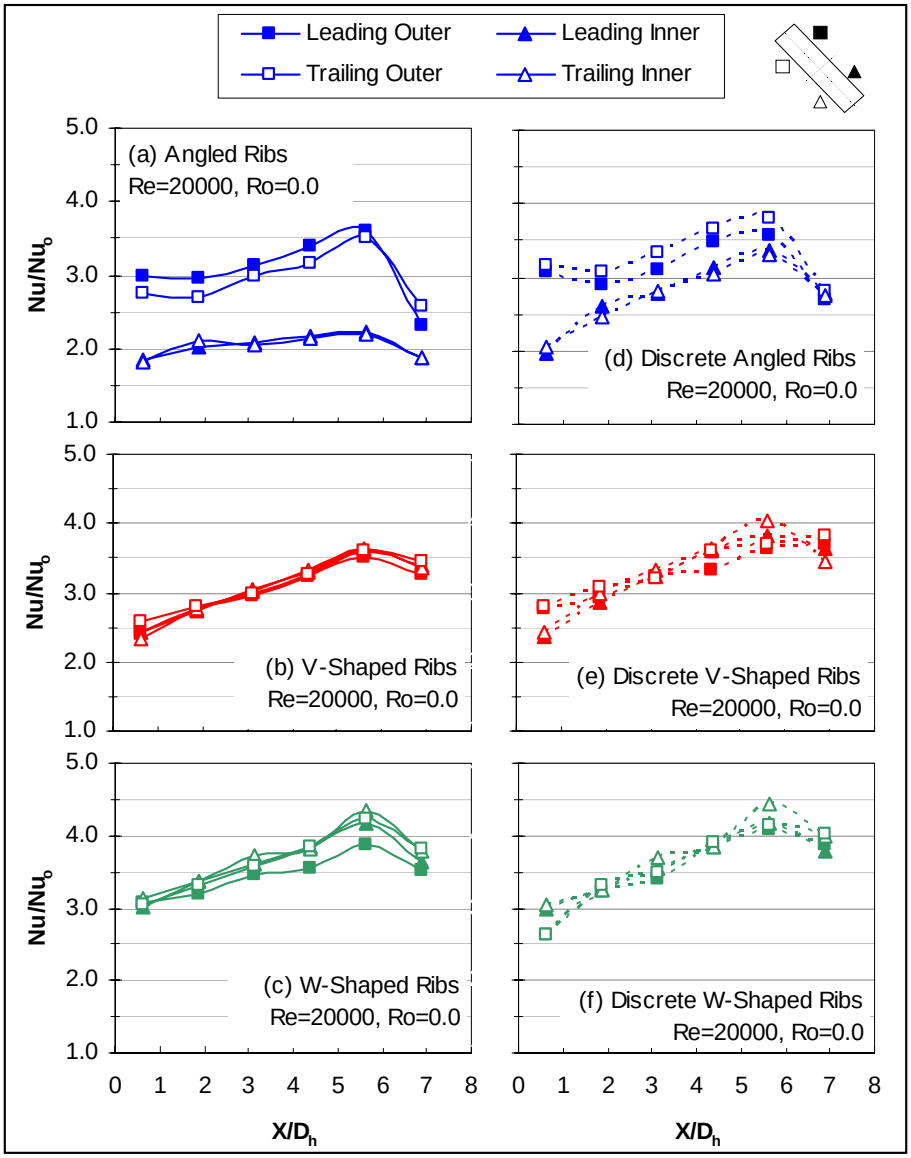


**Fig. 71 Nusselt number ratios in non-rotating channels with high performance ribs**

difference between the enhancement on the inner (leading and trailing) and outer (leading and trailing) surfaces decreases.

The heat transfer enhancement in the cooling channel with V-shaped ribs is shown in Fig. 71(b). Unlike in the angled rib channel, all surfaces within the V-shaped rib channel undergo the same level of heat transfer enhancement. The strength of the vortices continues to grow as the coolant travels streamwise through the channel. Therefore, the Nusselt number ratio continues to increase until the flow becomes fully developed; at this point the Nusselt number ratio remains constant.

The Nusselt number ratios in the cooling channel with W-shaped ribs are shown in Fig. 71(c). Like the V-shaped rib channel, the symmetry of the rib configuration results in all surfaces undergoing the same level of enhancement. The magnitude of the Nusselt numbers for these W-shaped ribs is greater than the magnitude of that in the V-shaped channel. This configuration is essentially two V-shaped ribs which meet at the center of the channel. Therefore, two areas of high heat transfer are created at the tip of each V. In addition, because the ribs in this configuration are shorter than the ribs of V-shaped configuration, the boundary layer along these shorter ribs is thinner than the boundary layer along the V-shaped ribs (see Fig. 70(b)). The result is more enhancement in the W-shaped rib channel than in the V-shaped rib channel.

The heat transfer distribution for the non-rotating channel with discrete angled ribs is shown in Fig. 71(d). Comparing the discrete angled ribs to the complete angled ribs (Fig. 71(a)), it is clearly seen the difference between the inner (leading and trailing) and outer (leading and trailing) surfaces decreases. The difference is the result of

significant enhancement on the leading-inner and trailing-inner surfaces. As shown in Fig. 70, the long angled rib has been broken; therefore, the continuous growth of the boundary layer from the outer surface to the inner surface does not exist. Instead, the boundary layer forms at the leading edge of the rib near the outer surface and has only half the channel to grow (as opposed to the entire channel). Similarly, on the leading and trailing inner surfaces, the boundary layer forms at the center of the channel and grows as the coolant is forced to the inner wall. Therefore, the boundary layer on the leading and trailing inner surfaces is much thinner than in the angled rib channel, and the result is significantly more enhancement along these surfaces.

Figure 71(e) shows the regionally averaged heat transfer distributions in the channel with discrete V-shaped ribs. The trends within this channel are similar to those in the complete V-shaped rib channel (Fig. 71(b)). The secondary flow induced by the ribs is not altered significantly when compared to the complete V-shaped ribs. The ribs create four rotating vortices; however, in this case, the vortices on the leading and trailing inner surfaces have been shifted downstream, as the V-shaped rib was broken. The advantage of this configuration over the complete V-shaped ribs is the enhancement that occurs just downstream of the V-shaped rib. As the coolant passes over the ribs, flow separation occurs, and immediately behind the ribs in the area of separation, there is relatively low heat transfer enhancement. When the V is broken, the area of low heat transfer immediately downstream of the point is reduced. Ekkad and Han [41] showed that the broken V-shaped ribs created a serpentine-like secondary flow in the center of

the channel. This secondary flow behavior results in more enhancement than the complete V-shaped ribs.

The Nusselt number ratios in the cooling channel with discrete W-shaped ribs are shown in Fig. 71(f). As the V-shaped and discrete V-shaped ribs, the trends of the W-shaped and discrete W-shaped ribs are similar. However, only a negligible difference exists between Nusselt number ratios of the W-shaped and discrete W-shaped rib channels. This discrete W configuration does not help the areas of relatively low heat transfer. In other words, the discrete V-shaped ribs reduced the area of low heat transfer behind the point of the complete V. With the discrete W-shaped ribs, the point associated with the V's is still present, the difference occurs at the center of the channel where the legs of the V's meet. As the coolant travels along these legs of the V's to the center of the channel, the heat transfer is decreasing. By shifting the V's on the inner surfaces to create this discrete W-shaped configuration, the heat transfer near the center of the channel is not increased. The rib induced flow of the discrete W-shaped ribs is similar to that of the W-shaped ribs. Therefore, as the coolant travels along the ribs, the heat transfer enhancement decreases in both configurations. Breaking the ribs at the centerline does nothing to increase the heat transfer in this area of relatively low heat transfer enhancement. Therefore, the level of heat transfer enhancement in the discrete W-shaped rib is the same as that in the complete W-shaped rib channel.

The regional heat transfer for the rotating channels is shown in Fig. 72. For the given Reynolds number of 20000, the corresponding rotation number is 0.075. Figure 72(a) shows the regionally averaged heat transfer distributions in the rotating channel

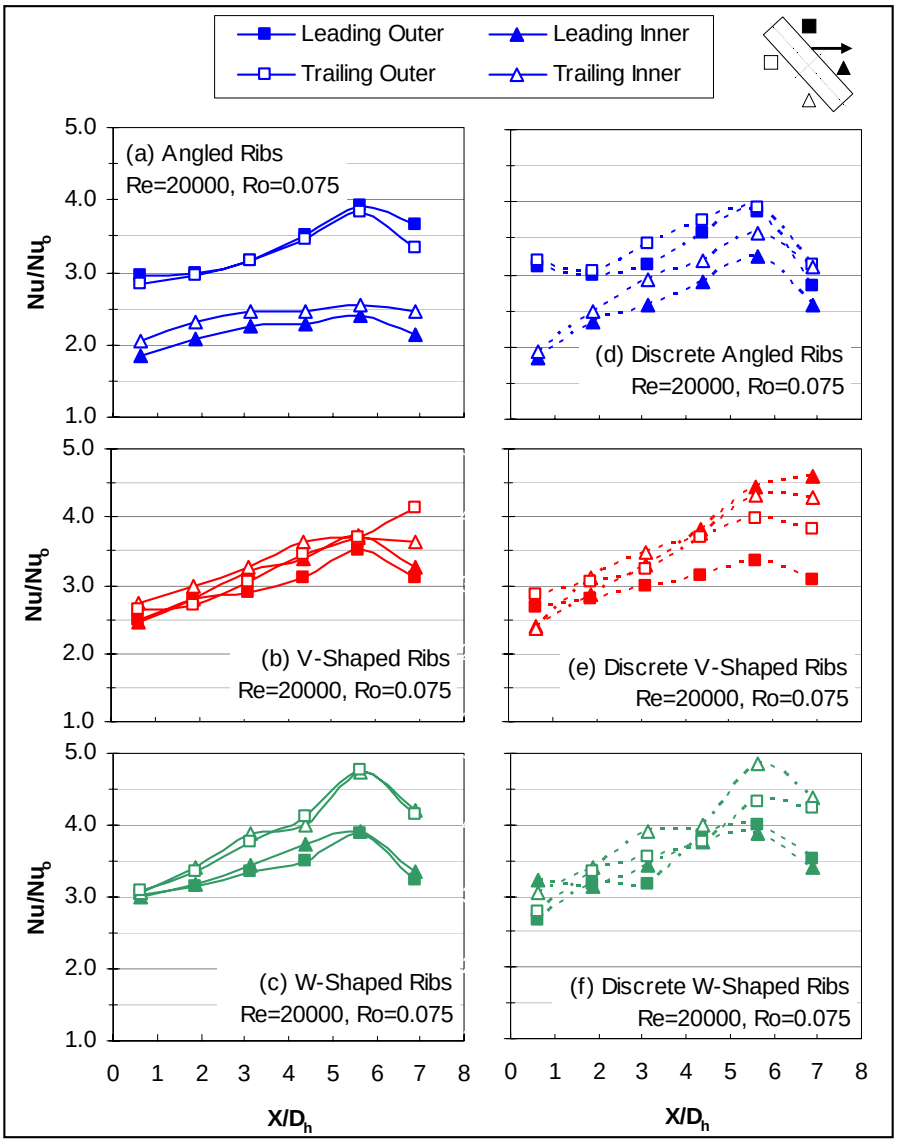


**Fig. 72 Nusselt number ratios in rotating channels with high performance ribs**

with angled ribs. All surfaces in the angled rib channel experience heat transfer enhancement with rotation. Although it is not shown, as the rotation number increases (Reynolds number decreases), the variation between the leading-outer and trailing-outer surfaces increases, and the same is true for the leading and trailing inner surfaces. Due to the nature of the rotation induced vortices, the trailing-outer surface undergoes greater heat transfer enhancement than the leading-outer surface because the rotation induced vortices are forcing the coolant from the leading-inner surface toward the trailing-outer surface. Likewise the trailing-inner surface experiences greater enhancement than the leading-inner surface.

The heat transfer enhancement in the rotating cooling channel with V-shaped ribs is shown in Fig. 72(b). It can be seen that the trailing-inner surface undergoes slightly higher heat transfer enhancement than the trailing-outer surface. This is due to the fact that the rib and rotation induced secondary flows move in opposite directions, and the combined effect of these secondary flows is weakened. However, along the leading and trailing-inner surfaces, both the rib and rotation induced secondary flows move into the same direction, and the combined effect of these secondary flows is strengthened (see Fig. 70(b)). As the rotation number decreases, the spanwise variation of the surfaces diminishes.

The Nusselt number ratios in the rotating cooling channel with W-shaped ribs are shown in Fig. 72(c). The effect of rotation is obviously seen at this intermediate rotation number of 0.075 (Re=20000). The trailing surfaces undergo significantly more enhancement than the leading surfaces, due to the rotation induced secondary flow. As

the coolant travels through the channel, the difference between the enhancement of the trailing and leading surfaces increases, as the vortices induced by rotation gain strength. The variation in this channel is much greater than was seen in the V-shaped rib channel. This is a result of the interaction of the vortices induced by the ribs and the vortices induced by rotation. Rhee et al. [44] showed the vortices induced by their discrete V-shaped ribs (similar to the W-shaped ribs of the present study) were much weaker than the vortices induced by the complete V-shaped ribs. Therefore, in the present study, rotation has a more dominant effect in the W-shaped rib channel than the V-shaped rib channel. As one would anticipate, as the Reynolds number increases (rotation number decreases), the variation between the trailing and leading surfaces decreases.

The heat transfer distribution for the rotating channel with discrete angled ribs is shown in Fig. 72(d). The difference between the rotating complete angled ribs (Fig. 72(a)) and these discrete angled ribs is similar to the differences of the non-rotating configurations (Figs. 71(a) and 71(d), respectively); the spanwise variation between the leading and trailing outer surfaces and the leading and trailing inner surfaces is dramatically reduced. The effect of rotation is also seen as the heat transfer on trailing-outer surface is enhanced more than the heat transfer on the leading-outer surface. The trailing-inner surface also undergoes more enhancement than the leading-inner surface. As the Reynolds number increases (rotation number decreases), the spanwise variation created by the ribs decreases, as well as the variation due to rotation.

The heat transfer trends of the rotating channel with discrete V-shaped ribs are shown in Fig. 72(e). The general trend is similar to the rotating channel with V-shaped

ribs (Fig. 71(b)); the additional enhancement of the trailing surfaces due to rotation can be seen. The Nusselt number ratios in the rotating cooling channel with discrete W-shaped ribs is shown in Fig. 72(f). The regional heat transfer trends of this configuration are similar to the complete W-shaped ribs (Fig. 72(c)).

The channel averaged heat transfer for the non-rotating and rotating channels is shown in Figs. 73 and 74, respectively. A comparison of the channel averaged values shown in Fig. 73 for the stationary channels, indicates the W-shaped and discrete W-shaped ribs have the best heat transfer performance. These are followed by the discrete V-shaped ribs, the V-shaped and discrete angled offering approximately the same level of enhancement, and the least enhancement is present in the non-rotating channel with angled ribs. For all cases, as the Reynolds number increases, the Nusselt number ratio decreases, and this should be anticipated as the Nusselt number for the smooth tube is increasing with Reynolds number. Figure 74 shows similar results for the rotating channel: the W-shaped and discrete W-shaped offer the greatest heat transfer enhancement.

In an effort to determine which rib configuration has the best thermal performance, it is critical to investigate the pressure drop penalty, as well as the heat transfer enhancement. The measured pressure drop is presented in the form of the friction factor ratio in Figs. 75 and 76 for the non-rotating and rotating channels, respectively. As shown in Fig. 75, the greatest frictional losses are incurred in the channel with the W-shaped ribs. The discrete W-shaped ribs and the V-shaped ribs follow this channel. The lowest frictional losses are in the channels with the angled ribs,

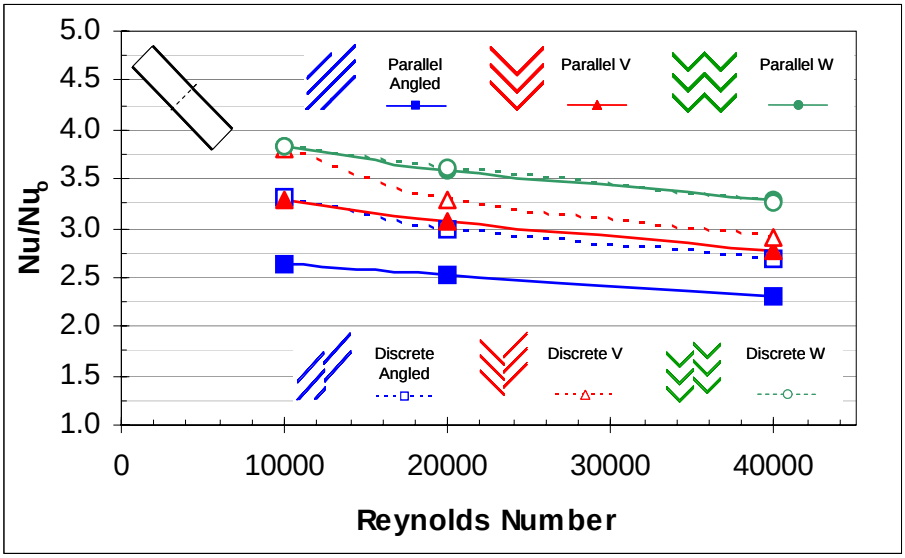


**Fig. 73 Channel averaged Nusselt number ratio in non-rotating channels**

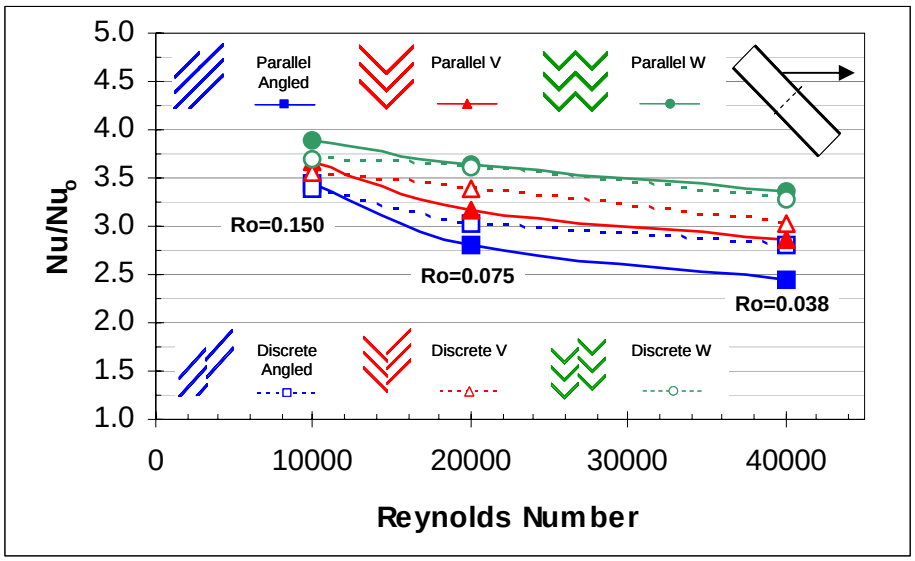


**Fig. 74 Channel averaged Nusselt number ratio in rotating channels**

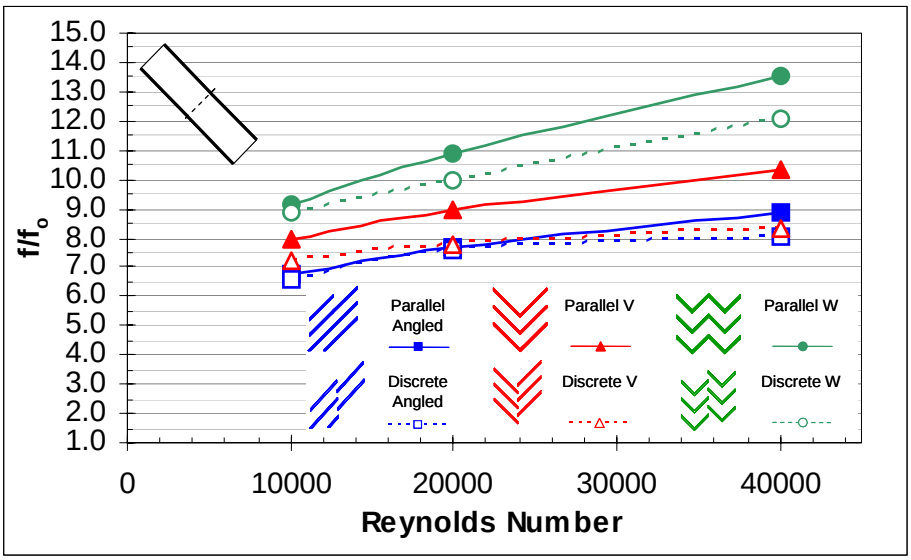


**Fig. 75 Friction factor ratio in non-rotating channels**

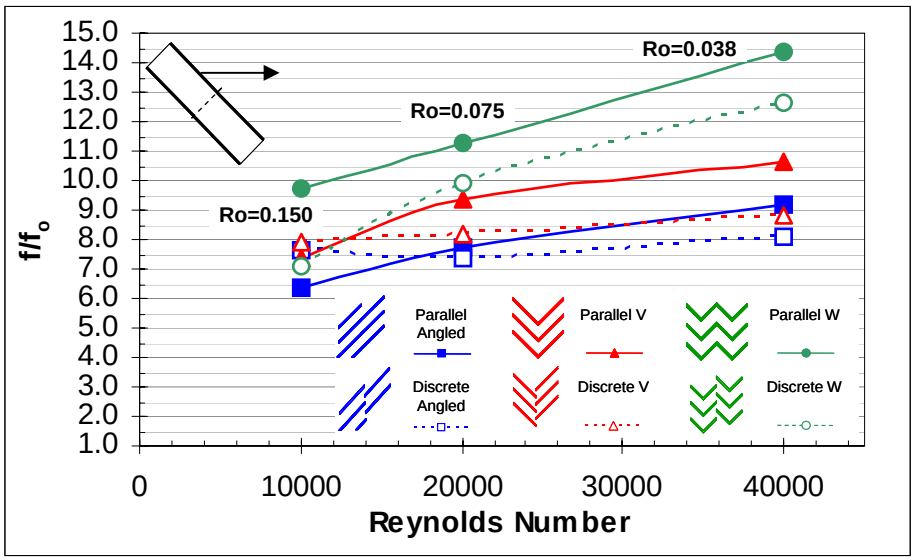


**Fig. 76 Friction factor ratio in rotating channels**

discrete V-shaped ribs, and the discrete angled ribs. Similar results are shown in Fig. 76, for the rotating channels. The W-shaped ribs and the discrete W-shaped ribs have the greatest pressure drop penalty.

It is important to address the accuracy of both the heat transfer enhancement measurements and the frictional loss measurements before continuing. The Nusselt number ratios and friction factor ratios of the stationary angled, discrete angled, V-shaped, and discrete V-shaped ribbed channels are compared to previous studies. Due to the infinite combinations of channel geometry and rib configurations, comparisons of the nature are generally difficult. However, previous studies involving rectangular channels with angled ribs [36, 42], discrete angled ribs [42], V-shaped ribs [44], and discrete V-shaped ribs [44] are considered in Figs. 77 and 78. The channel dimensions and rib parameters for each study are shown in Table 4. As shown in Fig. 77, the Nusselt number ratios in the 4:1 channel with angled ribs are comparable to previous studies. Decreasing the aspect ratio to 2:1 increases the enhancement. The heat transfer enhancement of the 4:1 channel with V-shaped ribs is slightly lower than the enhancement in both the 3:1 and 5:1 channel of Rhee et al. [44]. With this comparison, not only is the aspect ratio changing, the rib height-to-channel height ratio is changing. The discrete V-shaped rib results of Rhee et al. [44] are significantly lower than the present study due to very different rib configurations.

Figure 78 compares the friction factor ratio of the current studies to the previous studies. As shown in Fig. 78(a), the friction factor ratios of the current 4:1 angle ribbed channels are less those of the previous 4:1 study [36]. There is also significant

**Table 4 Cooling channel and rib parameter comparison**

| | | | | | **Units: cm** |
|---|---|---|---|---|---|
| | Configuration | AR | *e/H* | *P/e* | $\alpha$ |
| Present Study | Angled<br>Discrete Angled<br>V-Shaped<br>Discrete V-Shaped | 5.08 x 1.27 = 4:1 | 0.16 / 1.27 = 0.125 | 1.60 / 0.16 = 10 | 45° |
| Park et al. [36] | Angled | 10.16 x 5.08 = 2:1 | 0.32 / 5.08 = 0.063 | 3.2 / 0.32 = 10 | 45° |
| | | 10.16 x 2.54 = 4:1 | 0.32 / 2.54 = 0.125 | 3.2 / 0.32 = 10 | 45° |
| Cho et al. [42] | Angled<br>Discrete Angled | 10.16 x 5.08 = 2:1 | 0.50 / 5.08 = 0.098 | 5 / 0.5 = 10 | 45° |
| Rhee et al. [44] | V-Shaped | 15 x 5 = 3:1 | 0.30 / 5 = 0.06 | 3 / 0.3 = 10 | 60° |
| | | 15 x 3 = 5:1 | 0.30 / 3 = 0.10 | 3 / 0.3 = 10 | 60° |
| | Discrete V-Shaped | 15 x 5 = 3:1 | 0.30 / 5 = 0.06 | 3 / 0.3 = 10 | 45° |
| | | 15 x 3 = 5:1 | 0.30 / 3 = 0.10 | 3 / 0.3 = 10 | 45° |

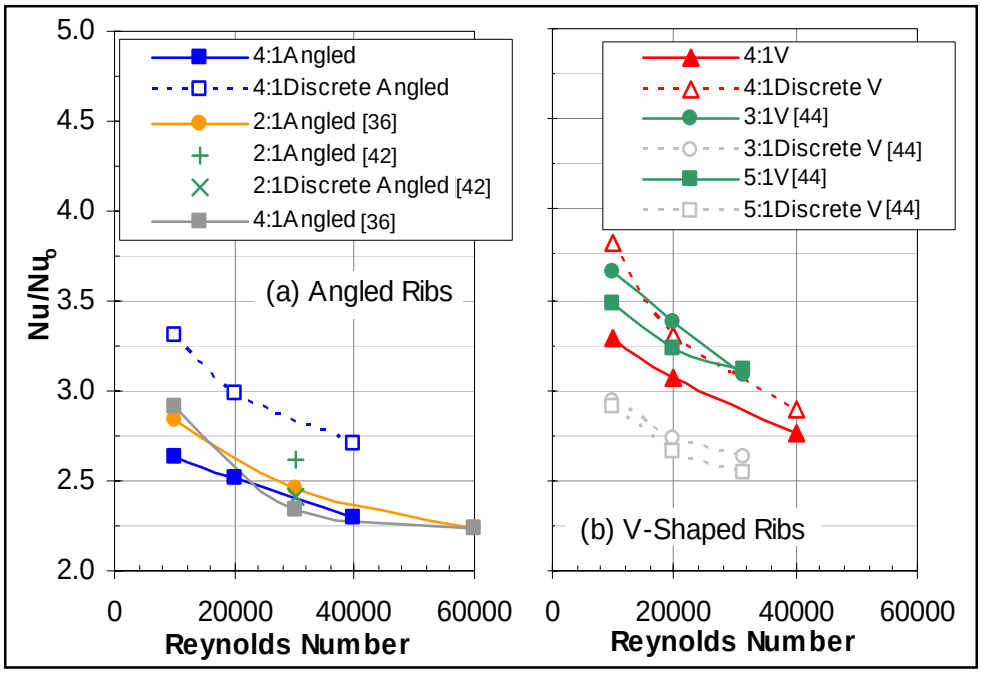


**Fig. 77 Nusselt number ratio comparison with previous studies**

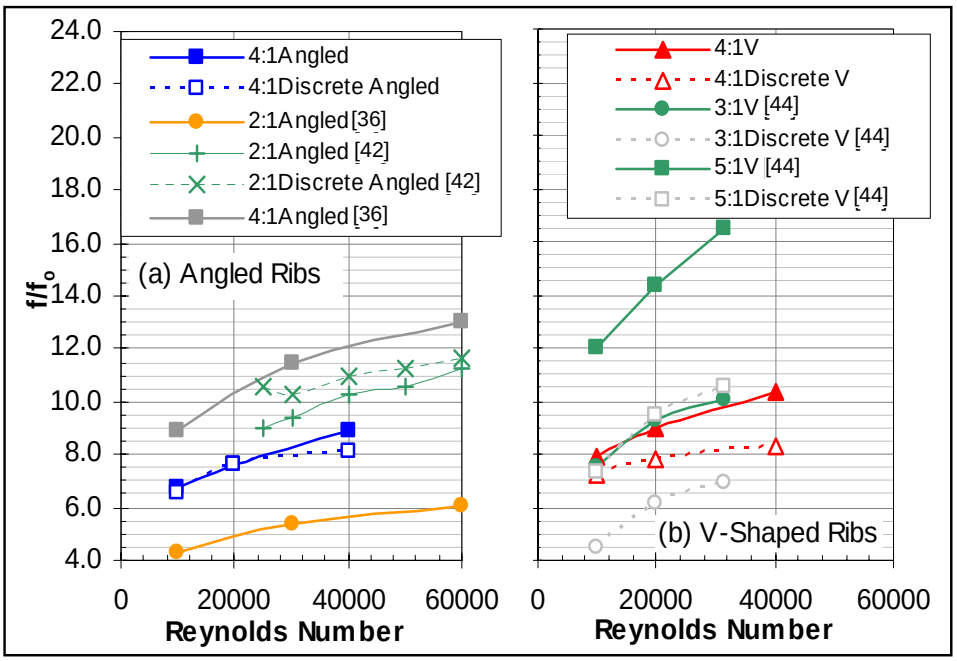


**Fig. 78 Friction factor ratio comparison with previous studies**

difference between the previous 2:1 studies of Cho et al. [42] and the previous 2:1 study of Park et al. [36]. However, because the non-dimensional rib and channel parameters are identical for the 4:1 channels, closer agreement between the two investigations is expected. When the actual dimensions of the channels are compared, one can see the 4:1 channel of Park et al. [36] is twice as large as the one of the current study. Also, the ribs of the previous study are twice as large as the ribs of the current study. Although the non-dimensional parameters are identical, the channels are actually very different. The situation is similar when comparing the V-shaped ribs of the present study with those of Rhee et al. [44]. With the large channel and ribs of the previous study, form drag becomes an issue. Form drag is primarily a function of the size and shape of an object. A large object creates an area of very low pressure immediately behind the object. Therefore, the smaller ribs of the present study, create less pressure drop than the much larger ribs of the previous studies ([36] and [44]), resulting in a lower friction factor ratio. When the frictional losses are coupled with the heat transfer enhancement, the thermal performance of each rib configuration can be evaluated.

Figure 79 shows the thermal performance of the rib configurations in the non-rotating channels. As shown previously, the W-shaped and discrete W-shaped ribs offered the greatest heat transfer enhancement; however, they also incurred the greatest frictional losses. From the overall performance point of view, the discrete V-shaped and discrete W-shaped ribs yield the greatest thermal performance. The discrete V-shaped ribs showed increased heat transfer enhancement and decreased frictional losses over the complete V-shaped ribs. Although the heat transfer enhancement for this configuration

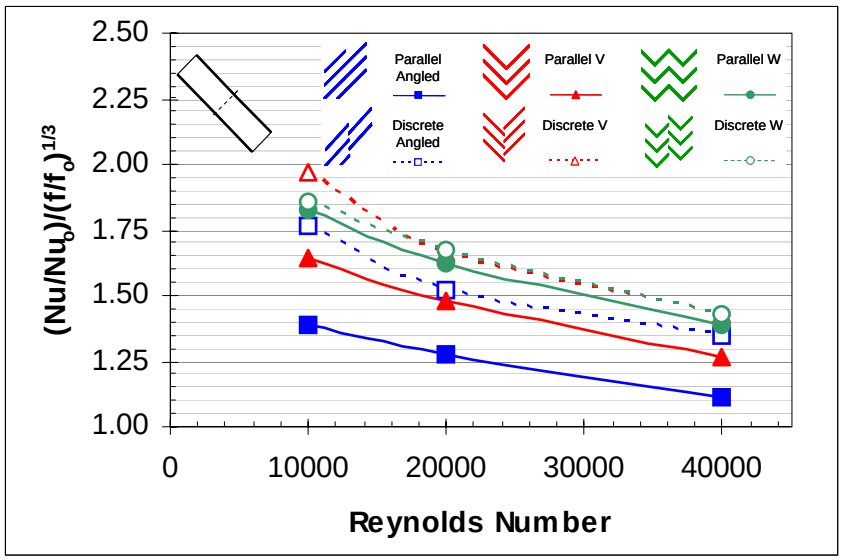


**Fig. 79 Thermal performance in non-rotating channels**

is lower than the W- shaped ribs, the frictional losses are significantly lower. The discrete V-shaped and discrete W-shaped configurations are followed closely by the complete W-shaped ribs. It is interesting to note the comparison between the angled and V-shaped ribs which are more commonly used in modern engines. The performance of the discrete angled rib is comparable to the performance of the complete V-shaped rib; a slight modification to the traditional angled rib design results in a significant increase in the overall thermal performance.

Figure 80 shows the thermal performance of the six rib configurations in the rotating channels. For the rotating channels, the discrete V-shaped ribs, the W-shaped ribs, and the discrete W-shaped ribs perform equally. The difference in the performance of each configuration is much less than was shown for the non-rotating channels. Again the performance of the discrete angled ribs is comparable to the V-shaped ribs, and the traditional angled ribs have the poorest performance of the six configurations under investigation.

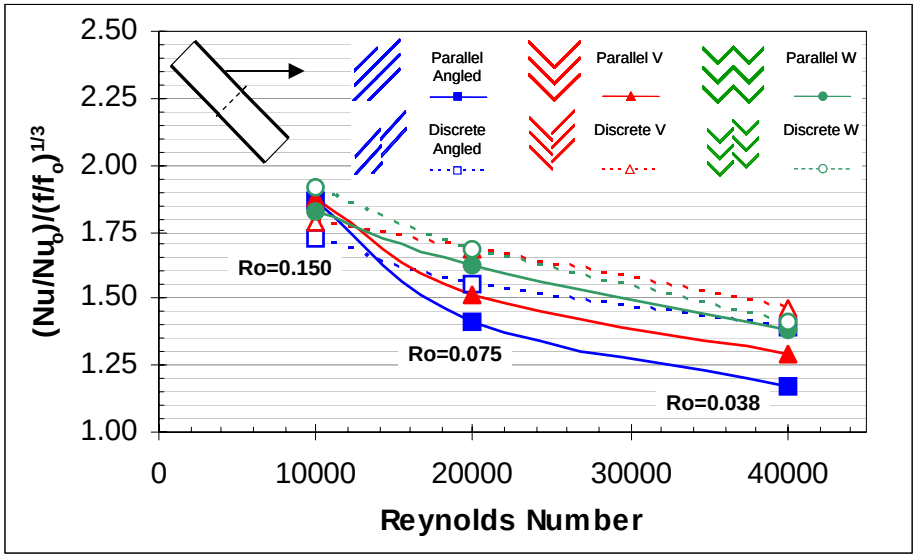


**Fig. 80 Thermal performance in rotating channels**

# CONCLUSIONS

This experimental study has considered both internal and external turbine blade cooling methods. Although the cooling techniques are used differently, they are employed with a common goal: cool the turbine components at a minimum cost. Based on all the experimental cases considered, the following conclusions can be drawn.

On the platform of a typical high pressure turbine blade, the film cooling effectiveness is significantly affected by the complex secondary flow along the passage endwall. The pressure sensitive paint technique clearly demonstrates the impact of passage secondary flow on the film cooling effectiveness. The effect of the secondary flows can be weakened, if the upstream injection rate is sufficiently large (at least 1 – 2% of the mainstream flow). Additionally, the passage vortex can be weakened with increased freestream turbulence, so the effectiveness due to the upstream slot injection increases.

The effect of the passage secondary flow is clearly seen when the film cooling effectiveness measured on the cascade endwall is compared to the effectiveness measured on a flat plate with tangential slot injection. Near the slot, the experimental data matches the correlation for the slot injection; however, downstream of the slot, the passage secondary flow strongly affects the film cooling effectiveness, and the effectiveness is significantly reduced when compared to the flat plate correlation. Therefore, the direct application of flat plate data to the blade platform should be done cautiously.

The behavior of the discrete film cooling holes is best described from traditional flat plate film cooling studies with cylindrical holes. The maximum effectiveness occurs when the blowing ratio ($M_f$) is 0.5. As the blowing ratio increases beyond 1.0, the coolant tends to lift off the surface, and protection is inadequate. Unlike with slot injection, increasing the freestream turbulence (from 0.75% to 13.4% at the cascade inlet and 5% at the cascade outlet) decreases the film cooling effectiveness near the discrete film cooling holes; this is also consistent with flat plate studies.

Finally, combining upstream slot injection with downstream discrete film hole cooling has the potential to further increase the endwall film cooling effectiveness. At an injection rate of 1.0%, the film cooling effectiveness increases more than 3 times over the effectiveness resulting from only upstream slot injection. However, when the injection rate is increased to 2.0%, the film effectives increases in this downstream region, but the amount of increase is less than when film cooling is combined with the 1.0% upstream slot injection rate.

The purge flow through an advanced seals is also significantly affected by the complex secondary flow along the passage endwall. The protection offered through the advanced seals is less than from the inclined slot and moreover from a tangential slot. However, with the advanced seal configurations, the coolant exits the seal more uniformly (across the entire length of the seal) than with the inclined slot. Although the effectiveness is reduced, the possibility of hot gas ingestion is also reduced; which is an obvious advantage of the advanced seal design.

The geometry of internal cooling passages in modern gas turbine blades is limited to by the blade profile. The cross-section of the cooling channels varies to meet the cross-section of the blade from the leading edge to the trailing edge. Channels with large aspect ratios and large orientation angles are typically located near the trailing edge of the blade. The coolant entering the blade does not travel through a straight constant cross-section channel; the entrance of the cooling channel is manufactured to meet the space limitations in the dovetail of the blade. This study experimentally investigated the effect of entrance geometry on heat transfer in rotating cooling channels with smooth walls and angled ribs. The study presents designers with new heat transfer data applicable to the design of cooling channels. It was shown the entrance geometry has a significant effect on the heat transfer in smooth rotating and non-rotating channels. In the smooth channel with a sudden contraction, the Nusselt number ratios are elevated above the fully developed values for the first 5 hydraulic diameters of the channel. The Nusselt number ratios in the channel with the partial sudden contraction are elevated above the fully developed values for the entire length of the channel. The effect of the entrance condition is also seen in the smooth rotating channel. However, as the rotation number increases, the effect of rotation is more dominant than the effect of entrance geometry. For all three entrance conditions, all surfaces within the channels experience heat transfer enhancement with the increasing effect of rotation. In addition, sudden and partial contraction entrances provide higher heat transfer enhancement than the fully developed entrance from the entrance of the channel through the first 3 to 4 hydraulic diameters of the channels with angled ribs.

Discrete V-shaped and discrete W-shaped ribs have the best thermal performance in both rotating and non-rotating channels. These configurations are followed closely by the W-shaped configuration. For the non-rotating and rotating rectangular channels, the W-shaped and discrete W-shaped ribs yield the best heat transfer enhancement. This comes at the cost of the greatest pressure drop. The performance of the V-shaped ribs is better than the performance of the angled ribs. Furthermore, the performance of the discrete angled ribs is comparable to that of the V-shaped ribs in both non-rotating and rotating channels.

This study used a wide variety of experimental techniques and cooling techniques in an attempt to provide engineers with reliable cooling data. The results can be used to aid in the development of more efficient cooling schemes which minimize the amount of cooling air required, so the turbine components can survive the extreme conditions of the high pressure turbine.

## REFERENCES

[1] Han, J.C., Dutta, S., and Ekkad, S.V., 2000, *Gas Turbine Heat Transfer and Cooling Technology*, Taylor and Francis, New York.

[2] Lakshminarayana, B., 1996, *Fluid Dynamics and Heat Transfer of Turbomachinery*, John Wiley, New York, pp. 597-721.

[3] Dunn, M.G., 2001, "Convection Heat Transfer and Aerodynamics in Axial Flow Turbines," ASME Journal of Turbomachinery, **123**, pp.637-686.

[4] Goldstein, R.J., 2001, "Heat Transfer in Gas Turbine Systems," Annals of The New York Academy of Sciences, pp. **934**.

[5] Chyu, M.K., 2001, "Heat Transfer near Turbine Nozzle Endwall," Annals of the New York Academy of Sciences, **934**, pp. 27-36.

[6] Langston, L.S., Nice, L.M., and Hooper, R.M., 1976, "Three-Dimensional Flow within a Turbine Cascade Passage," ASME Paper no. 76-GT-50.

[7] Langston, L.S., 1980, "Crossflows in a Turbine Cascade Passage," ASME J. Engineering for Power, **102**, pp. 866-874.

[8] Goldstein, R.J. and Spores, R.A., 1988, "Turbulent Transport on the Endwall in the Region between Adjacent Turbine Blades." ASME J. Heat Transfer, **110**, pp. 862-869.

[9] Blair, M.F., 1974, "An Experimental Study of Heat Transfer and Film Cooling on Large-Scale Turbine Endwall," ASME J. Heat Transfer, **96**, pp. 524-529.

[10] Graziani, R.A., Blair, M.F., Taylor, J.R., and Mayle, R.E., 1980, "An Experimental Study of Endwall and Airfoil Surface Heat Transfer in a Large Scale Turbine Blade Cascade," ASME J. Engineering for Power, **102**, pp. 257-267.

[11] York, R.E., Hylton, L.D., and Mihelc, M.S., 1984, "An Experimental Investigation of Endwall Heat Transfer and Aerodynamics in a Linear Vane Cascade," ASME J. Engineering for Gas Turbines and Power," **106**, pp. 159-167.

[12] Radomsky, R.W. and Thole, K.A., 2000, "High Free-Stream Turbulence Effects on Endwall Heat Transfer for a Gas Turbine Stator Vane," ASME J. Turbomachinery, **122**, pp. 299-708.

[13] Kwak, J.S., Lee, J.H., and Han, J.C., 2002, "Heat Transfer and Pressure Distributions on a Gas Turbine Vane End-Wall," Proc. 12th International Heat Transfer Conference, Grenoble, France, pp. 693-698.

[14] Takeishi, K., Matsuura, M., Aoki, S., and Sato, T., 1990, "An Experimental Study of Heat Transfer and Film Cooling on Low Aspect Ratio Turbine Nozzles," ASME J. Turbomachinery, **112**, pp. 488-496.

[15] Harasgama, S.P. and Burton, C.S., 1992, "Film Cooling Research on the Endwall of a Turbine Nozzle Guide Vane in a Short Duration Annular Cascade: Part 1 – Experimental Technique and Results," ASME J. Turbomachinery, **114**, pp. 734-740.

[16] Jabbari, M.Y., Marston, K.C., Eckert, E.R.G., and Goldstein, R.J., 1996, "Film Cooling of the Gas Turbine Endwall by Discrete-Hole Injection," ASME J. Turbomachinery, **118**, pp. 278-284.

[17] Friedrichs, S., Hodson, H.P., and Dawes, W.N., 1996, "Distribution of Film-Cooling Effectiveness on a Turbine Endwall Measured Using the Ammonia and Diazo Technique," ASME J. Turbomachinery, **118**, pp. 613-621.

[18] Friedrichs, S., Hodson, H.P., and Dawes, W.N., 1997, "Aerodynamic Aspects of Endwall Film Cooling," ASME J. Turbomachinery, **119**, pp. 786-793.

[19] Friedrichs, S., Hodson, H.P., and Dawes, W.N., 1998, "The Design of an Improved Endwall Film Cooling Configuration," ASME Paper no. 98-GT-483.

[20] Barigozzi, G., Benzoni, G., Franchini, G., and Derdichizzi, A., 2005, "Fan-Shaped Hole Effects on the Aero-Thermal Performance of a Film Cooled Endwall," ASME Paper no. GT2005-68544.

[21] Roy, R.P., Squires, K.D., Gerendas, M., Song, S., Howe, W.J., and Ansari, A., 2000, "Flow and Heat Transfer at the Hub Endwall of Inlet Vane Passages – Experiments and Simulations," ASME Paper no. 2000-GT-198.

[22] Burd, S.W., Satterness, C.J., and Simon, T.J., 2000, "Effects of Slot Bleed Injection Over a Contoured End Wall on Nozzle Guide Vane Cooling Performance: Part II – Thermal Measurements," ASME Paper no. 2000-GT-200.

[23] Oke, R., Simon, T., Shih, T., Zhu, B., Lin, Y.L., and Chyu, M., 2001, "Measurements over a Film-Cooled Contoured Endwall with Various Coolant Injection Rates," ASME Paper no. 2001-GT-0140.

[24] Oke, R.A. and Simon, T.W., 2002, "Film Cooling Experiments with Flow Introduced Upstream of a First Stage Nozzle Guide Vane through Slots of Various Geometries," ASME Paper no. GT-2002-30169.

[25] Nicklas, M., 2001, "Film-Cooled Turbine Endwall in a Transonic Flow Filed: Part II – Heat Transfer and Film Cooling Effectiveness," ASME J. Turbomachinery, **123**, pp. 720-729.

[26] Liu, G., Liu, S., Zhu, H., Lapworth, B.C., and Forest, A.E., 2004, "Endwall Heat Transfer and Film Cooling Measurements in a Turbine Cascade with Injection Upstream of Leading Edge," Heat Transfer – Asian Research, **33**, pp. 141-152.

[27] Zhang, L.J. and Jaiswal, R.S., 2001, "Turbine Nozzle Endwall Film Cooling Study Using Pressure-Sensitive Paint," ASME J. Turbomachinery, **123**, pp. 730-735.

[28] Zhang, L.J. and Moon, H.K., 2003, "Turbine Nozzle Endwall Inlet Film Cooling – The Effect of a Backward Facing Step," ASME Paper no. GT2003-38319.

[29] Knost, D.G. and Thole, K.A., 2004, "Adiabatic Effectiveness Measurements of Endwall Film Cooling for a First Stage Vane," ASME Paper no. GT2004-53326.

[30] Cardwell, N.D., Sundaram, N., and Thole, K.A., 2005, "Effects of Mid-Passage Gap, Endwall Misalignment and Roughness on Endwall Film-Cooling," ASME Paper no. GT2005-68900.

[31] Zess, G.A. and Thole, K.A., 2002, "Computational Design and Experimental Evaluation of Using a Leading Edge Fillet on a Gas Turbine Vane," ASME J. Turbomachinery, **124**, pp. 167-175.

[32] Shih, T.I.P. and Lin, Y.L., 2002, "Controlling Secondary-Flow Structure by Leading-Edge Airfoil Fillet and Inlet Swirl to Reduce Aerodynamic Loss and Surface Heat Transfer," ASME Paper no. GT-2002-30529.

[33] Han, S. and Goldstein, R.J., 2005, "Influence of Blade Leading Edge Geometry on Turbine Endwall Heat (Mass) Transfer," ASME Paper no. GT2005-68590.

[34] Han, J.C., 1988, "Heat Transfer and Friction Characteristics in Rectangular Channels with Rib Turbulators," ASME Journal of Heat Transfer, **110**, pp. 321-328.

[35] Han, J.C. and Park, J.S., 1988, "Developing Heat Transfer in Rectangular Channels with Rib Turbulators," International Journal of Heat and Mass Transfer, **31**, pp. 183-195.

[36] Park, J.S., Han, J.C., Huang, Y., Ou, S., and Boyle, R.J., 1992, "Heat Transfer Performance Comparisons of Five Different Rectangular Channels with Parallel Angled Ribs," International Journal of Heat and Mass Transfer, **35**, pp. 2891-2903.

[37] Han, J.C., Zhang, Y.M., and Lee, C.P., 1991, "Augmented Heat Transfer in Square Channels with Parallel, Crossed, and V-Shaped Angled Ribs," ASME Journal of Heat Transfer, **113**, pp. 590-596.

[38] Lau, S.C., Kukreja, R.T., and McMillin, R.D., 1991, "Effects of V-shaped Rib Arrays on Turbulent Heat Transfer and Friction of Fully Developed Flow in a Square Channel," International Journal of Heat and Mass Transfer, **34**, pp. 1605-1616.

[39] Han, J.C. and Zhang, Y.M, 1992, "High Performance Heat Transfer Ducts with Parallel Broken and V-shaped Broken Ribs," International Journal of Heat and Mass Transfer, **35**, pp. 513-523.

[40] Taslim, M.E., Li, T., and Kercher, D.M., 1996, "Experimental Heat Transfer and Friction in Channels Roughened with Angled, V-Shaped, and Discrete Ribs on Two Opposite Walls," ASME Journal of Turbomachinery, **118**, pp. 20-28.

[41] Ekkad, S.V. and Han, J.C., 1997, "Detailed Heat Transfer Distribution in Two-Pass Square Channels with Rib Turbulators," International Journal of Heat and Mass Transfer, **40**, pp. 2525-2537.

[42] Cho, H.H., Wu, S.J., and Kwon, H.J., 2000, “Local Heat/Mass Transfer Measurements in a Rectangular Duct with Discrete Ribs,” ASME Journal of Turbomachinery, **122**, pp. 579-586.

[43] Gao, X. and Suden, B., 2001, “Heat Transfer and Pressure Drop Measurements in Rib-roughened Rectangular Ducts,” Experimental Thermal and Fluid Science, **24**, pp. 25-34.

[44] Rhee, D.H., Lee, D.H, Cho, H.H., and Moon, H.K., 2003, “Effects of Duct Aspect Ratios on Heat /Mass Transfer with Discrete V-Shaped Ribs,” ASME Paper no. GT2003-38622.

[45] Johnson, B.V., Wagner, J.H., Steuber, G.D., and Yeh, F.C., 1994, “Heat Transfer in Rotating Serpentine Passages with Trips skewed to the Flow,” ASME Journal of Turbomachinery, **116**, pp. 113-123.

[46] Johnson, B.V., Wagner, J.H., Steuber, G.D., and Yeh, F.C., 1994, “Heat Transfer in Rotating Serpentine Passages with Selected Model Orientations for Smooth or Skewed Trip Walls,” ASME Journal of Turbomachinery, **116**, pp. 738-744.

[47] Parsons, J.A., Han, J.C., and Zhang, Y.M., 1994, "Wall Heating Effect on Local Heat Transfer in a Rotating Two-Pass Square Channel With 90° Rib Turbulators,” International Journal of Heat and Mass Transfer, **37**, pp. 1141-1420.

[48] Parsons, J.A., Han, J.C., and Zhang, Y.M., 1995, "Effects of Model Orientation and Wall Heating Condition on Local Heat Transfer in a Rotating Two-Pass Square Channel With Rib Turbulators,” International Journal of Heat and Mass Transfer, **38**, pp. 1151-1159.

[49] Dutta, S., and Han, J.C., 1996, "Local Heat Transfer in Rotating Smooth and Ribbed Two-Pass Square Channels with Three Channel Orientations," ASME Journal of Heat Transfer, **118**, pp. 578-584.

[50] Park C.W., Lau, S.C., Kukreja, R.T., 1998, "Heat/Mass Transfer in a Rotating Two-Pass Square Channel with Transverse Ribs." AIAA Journal of Thermophysics and Heat Transfer, **12**, pp. 80-86.

[51] Park, C.W, Yoon, C, Lau, S.C. 2000, "Heat (Mass) Transfer in a Diagonally Oriented Rotating Two-Pass Channels with Rib-Roughened Walls," ASME Journal of Heat Transfer, **122**, pp. 208-211.

[52] Taslim, M.E., Rahman, A., and Spring, S.D., 1991, "An Experimental Investigation of Heat Transfer Coefficients in a Span-wise Rotating Channel With Two Opposite Rib-Roughened Walls," ASME Journal of Turbomachinery, **113**, pp. 75-82.

[53] Taslim, M.E., Bondi, L.A., and Kercher, D.M., 1991, "An Experimental Investigation of Heat Transfer in an Orthogonally Rotating Channel Roughened With $45^{o}$ Criss-Cross Ribs on Two Opposite Walls," ASME Journal of Turbomachinery, **113**, pp. 346-353.

[54] Kiml, R., Mochizuki S, Murata, A., 2001, "Effects of Rib Arrangements on Heat Transfer and Flow Behavior in a Rectangular Rib-Roughened Passage: Application to Cooling of Gas Turbine Blade Trailing Edge," ASME Journal of Heat Transfer, **123**, pp. 675-681.

[55] Kiml, R., Mochizuki S, Murata, A., 2001, "Heat Transfer Enhancement Mechanism in a Rectangular Passage with $\tilde{V}$ and $\tilde{\Lambda}$ shaped Ribs," Journal of Flow Visualization and Image Processing, **8**, pp. 51-68.

[56] Azad, G.S., Uddin, M.J., Han, J.C., Moon, H.K., and Glezer, B., 2002, "Heat Transfer in a Two–Pass Rectangular Rotating Channel With 45-deg Angled Rib Turbulators," ASME Journal of Turbomachinery, **124**, pp.251-259.

[57] Al-Hadhrami, L., and Han, J.C., 2003, "Effect of Rotation in Two-Pass Square Channels with Five Different Orientations of 45° Angled Rib Turbulator," International Journal of Heat and Mass Transfer, **46**, pp. 653-669.

[58] Al-Hadhrami, L., Griffith, T.S., and Han, J.C., 2003, "Heat Transfer in Two-Pass Rotating Rectangular Channels (AR=2) with Five Different Orientations of 45° V-shaped Rib Turbulators," ASME Journal of Heat Transfer, **125**, pp. 232-242.

[59] Griffith, T.S., Al-Hadhrami, L., and Han, J.C., 2002, "Heat Transfer in Rotating Rectangular Channels (AR=4) with Angled Ribs," ASME Journal of Heat Transfer, **124**, pp. 617 -625.

[60] Lee, E., Wright, L.M., and Han, J.C., 2003, "Heat Transfer in Rotating Rectangular Channels (AR = 4:1) with V-Shaped and Angled Rib Turbulators with and without Gaps," ASME Paper no. GT2003-38900.

[61] Cho, H. H., Kim, Y. Y., Kim, K. M., and Rhee, D. H., 2003, "Effects of Rib Arrangements and Rotation Speed on Heat Transfer in a Two-Pass Duct," ASME Paper no. GT2003-38609.

[62] Agarwal, P., Acharya, S., and Nikitopoulos, D. E., 2003, "Heat/Mass Transfer in 1:4 Rectangular Passages with Rotation," ASME Paper no GT2003-38615.

[63] Kays, W.M. and Crawford, M.E., 1993, *Convective Heat and Mass Transfer*, 3rd ed., McGraw-Hill, New York, pp. 345-348.

[64] Boelter, L.M.K., Young, G., and Iverson, H.W., 1948, "An Investigation on Aircraft Heaters – Distribution of Heat Transfer Rate in the Entrance Section of a Circular Tube," NACA Technical Note no. 1451.

[65] Burggraf, F., 1970, "Experimental Heat Transfer and Pressure Drop with Two-dimensional Turbulence Promoter Applied to Two Opposite Walls of a Square Duct," In *Augmentation of Convective Heat and Mass Transfer* (Edited by A.E. Bergles and R.L. Webb), ASME, New York, pp. 70-79.

[66] Liou, T.M. and Hwang, J.J., 1992, "Developing Heat Transfer and Friction in a Ribbed Rectangular Duct With Flow Separation at Inlet," Journal of Heat Transfer, **114**, pp. 565-573.

[67] Liu, T., Campbell, B.T., Burns, S.P., and Sullivan, J.P., 1997, "Temperature- and Pressure- Sensitive Luminescent Paints in Aerodynamics," Applied Mechanics Review, **50**, pp. 227 – 246.

[68] Crafton, J., Lachendro, N., Guille, M, Sullivan, J.P., and Jordan, J.D., 1999, "Application of Temperature and Pressure Sensitive Paint to an Obliquely Impinging Jet," AIAA Paper no. AIAA-99-0387.

[69] Liu, Q., Kapat, J.S., Douglass, C.J., and Qiu, L., 2003, "Applicability of Temperature Sensitive Paints for Measurement of Surface Temperature Distribution," ASME Paper no. GT2003-38591.

[70] Kline, S.J., and McClintock, F.A., 1953, "Describing Uncertainties in Single-Sample Experiments," Mech. Eng. (Am. Soc. Mech. Eng.), **75**, pp. 3-8.

[71] Zhang, L. and Han, J.C., 1994, "Influence of Mainstream Turbulence on Heat Transfer Coefficients from a Gas Turbine Blade," ASME J. Heat Transfer, **116**, pp. 896-903.

[72] Goldstein, R.G., 1971, "Film Cooling," Advances in Heat Transfer, **7**, pp. 321 – 379.

[73] Wagner, J.H., Johnson, B.V., and Kopper, F.C., 1991, "Heat Transfer in Rotating Serpentine Passages With Smooth Walls," ASME Journal of Turbomachinery, **113**, pp. 321-330.

[74] Rohsenow, W.M. and Choi, H., 1961, *Heat, Mass, and Momentum Transfer*, Prentice-Hall, Inc., New Jersey, pp. 192-193.

[75] Kays, W.M. and Crawford, M.E., 1993, *Convective Heat and Mass Transfer*, 3rd ed., McGraw-Hill, New York, pp. 249.

[76] Han, J.C., Park, J.S., and Lei, C.K., 1985, "Heat Transfer Enhancement in Channels with Turbulence Promoters," ASME Journal of Engineering for Gas Turbines and Power, **107**, pp. 628-635.

[77] Al-Qahtani, M., Jang, Y.J., Chen, H.C., and Han, J.C., 2002, "Prediction of Flow and Heat Transfer in Rotating Two-Pass Rectangular Channels with 45-deg Rib Turbulators," ASME Journal of Turbomachinery, **124**, pp. 242-250.

[78] Su, G., Teng, S., Chen, H.C., and Han, J.C., 2003, "Computation of Flow and Heat Transfer in Rotating Rectangular Channels (AR=4) with V-Shaped Ribs by a Reynolds Stress Turbulence Model," ASME Paper no. GT2003-38348.

# VITA

Name: Lesley Mae Wright

Address: c/o Jimmy and Loretta Wright
2503 Cary Dr.
Benton, AR 72015

E-mail Address: WrightL8@asme.org

Education: B.S., Engineering, Arkansas State University, 2001
M.S., Mechanical Engineering, Texas A&M University, 2003
Ph.D., Mechanical Engineering, Texas A&M University, 2006